Università
Ca'Foscari
Venezia

Ca' Foscari
Dorsoduro 3246
30123 Venezia

Master's Degree programme – Second Cycle
(*D.M. 270/2004*)
in Science and Technology of bio and
nanomaterials

Final Thesis

Influence of different ceramic femoral heads on the oxidative degradation of Highly Crosslinked Polyethylene liners

Supervisor
Ch. Prof. Alvise Benedetti
Ch. Prof. Giuseppe Pezzotti

Graduand
Elisa Casagrande
Matriculation Number 818979

Academic Year
2015 / 2016

Acknowledgements

Grazie a tutte le persone che hanno contribuito in maniera diretta o indiretta al conseguimento di questo traguardo.

Il mio relatore Prof. Alvise Benedetti per i preziosi consigli e la costante disponibilità. Il mio co-relatore Prof. Giuseppe Pezzotti, per avermi dato l'opportunità di svolgere l'internato di tesi presso il suo gruppo di ricerca, al Kyoto Institute of Technology. Leonardo, per avermi fatto pazientemente da mentore e per avermi spronata a fare sempre del mio meglio.

I miei genitori e mio fratello, per essermi sempre vicini, a dispetto della distanza che ci separa ormai da così tanto tempo.
Tommaso per avermi spinta a camminare sulle mie gambe e per aver incessantemente creduto in me.

Gli amici di sempre, per l'interesse che mi dimostrano ogni giorno, e i compagni che hanno condiviso con me gioie e dolori degli ultimi due anni.

Grazie a chi ha percorso con me parte del mio cammino, lasciando anche solo un piccolo segno del suo passaggio.

Un sincero ringraziamento a tutti.

Elisa Casagrande

Contents

Abstract

Long-term oxidative degradation of ultra-high molecular weight polyethylene (UHMWPE) bearings in THA is a major factor in limiting the longevity of prosthetic joint implants. In ceramic-UHMWPE articulations, the ceramic counter-surface has historically been assumed to be biologically inert. However, it is difficult to believe that no interaction establishes between the two sliding counterpart surfaces in the biological environment, on a long-term period. To investigate how femoral heads and polyethylene liners work as a whole system, and how the surface chemistry of ceramic materials can affect the oxidative degradation and joint lifetime, polyethylene liners were tested in static contact with different ceramic heads (*e.g.*, monolithic alumina, zirconia, zirconia-toughened alumina and silicon nitride), and exposed to hydrothermal environment.

Microscopic information extracted from Raman spectroscopic mapping of UHMWPE liners before and after accelerated aging, showed how the oxidation process induces a noticeable increase in crystallinity and orthorhombic phase content.

A trend of higher oxidative propensity was found out against oxide femoral heads in comparison with non-oxide ones. This trend was a common denominator to the three different oxide materials tested.

Raman spectroscopic data were confirmed on the molecular scale with cathodoluminescence (CL) and X-ray photoemission spectroscopy. They revealed enhanced fractions of oxidized sites on the non-oxide (Si_3N_4)-ceramic head surfaces and higher oxygen concentration in couples including oxide counterparts as compared to a Si_3N_4 counterpart, respectively.

Definitely, the presented data showed that oxide ceramics (*e.g.*, monolithic alumina, zirconia, or zirconia-toughened alumina) affect differently the oxidative degradation of the UHMWPE counter-surface as compared to the surfaces of Si_3N_4 based ceramics. These findings challenge the general definition of bioinertness for ceramic materials, which showed instead to affect, in a positive or negative way, polyethylene oxidative degradation.

Introduction

The most popular and widespread cause of chronic diseases with a high potential for disability are dysfunctions of the musculoskeletal apparatus. These account for 50% of chronic disease in those aged over 65 years and have a high impact on the healthcare system [1]. Eventually they lead to the prosthetic replacement of the involved joint, which, thanks to advances in surgical techniques and in materials research, turns out to be an effective treatment. The prosthetic replacement allows in fact to the patient the restoration of the articular function, the elimination of pain and the improvement of the quality of life, in almost all cases [2]. For this reason, and several other causes (such as the increasing world population, the increasing average life expectancy and changes in lifestyle), the demand for artificial joint replacements and the number of operations carried out in industrialized countries is constantly increasing [3].

Each year around 1 million patients worldwide undergo THA surgery [4]. In Italy, in particular, about 120.000 or more replacements are performed every year. According to the data on hospitalizations (Figure 1), replacements of diseased joints, either hip or knee, in the period 2001-2005 show an average annual increase of +5% for hip replacement and +13% for knee replacement. In 2005, there were more than 87.000 hip and 47.000 knee operations [2].

This phenomenon is getting more and more significant, weighting dramatically on the public health care system.
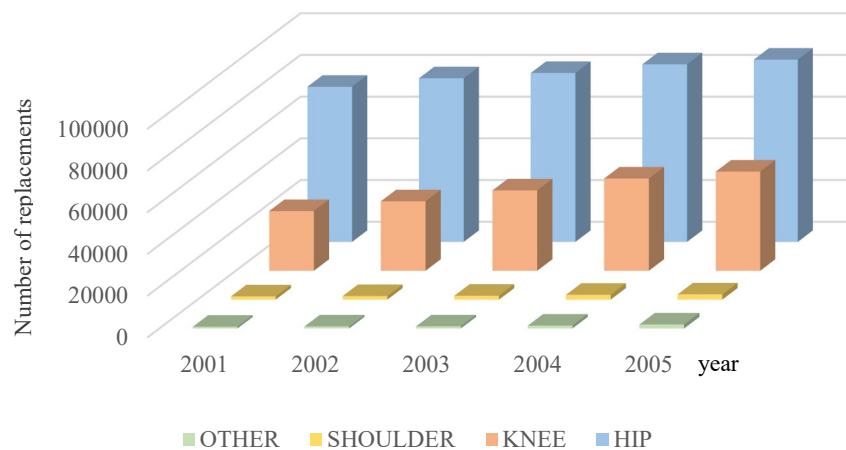
Figure 1: Number of different types of prosthetic surgery (total + partial) in Italy during the years from 2001 to 2005 (Source: ISTISAN Report 9/22)

The replacement of joints, especially hip and knee, represents one of the most successful surgical innovations of the last century. Artificial hip prosthesis are innovative and high quality engineering products. Unfortunately, even if they are designed to last more than 20 years, they have a limited life due to wear [3]. Despite the good results already obtained, biomedical companies continue to invest huge

capital in the search for new materials and improvement of designs already on the market.

The purpose of the ongoing research is to create implants with greater reliability and duration of human life. Revision surgeries (replacement of a part or the whole prosthesis) in fact have a lower success rate compared to the first replacement. The key to success in the arthroplasty field is the improvement of implant performances, regarding structural and environmental long-term reliability in vivo, reaching a lifespan of at least several decades.

The field of biomaterials for orthopedic applications is therefore extremely active and innovative [5]. In fact, it is very important to understand fully the in vivo and in vitro behavior of these biomaterials, checking the reliability by means of non-destructive analysis both before and after their implantation in the human body.

Chapter 1
Aim of the thesis

Oxidation and wear are the main factors limiting the durability of polyethylene acetabular cups. For this reason, when determining at which rate the microstructure of polyethylene liners becomes affected by oxidation in the joint environment, it must be considered also the interaction with the corresponding femoral head.

Hence, the aim of this thesis was twofold:
   a) investigating the oxidation rate of polyethylene, when exposed to accelerated aging in autoclave, and determining the increase in crystallinity and consequent embrittlement;
   b) deepening how femoral heads and polyethylene liners work as a whole system, and how the surface chemistry of ceramic materials can affect the oxidative degradation of polyethylene liners.

Therefore, polyethylene liners were tested in static contact with different ceramic heads (*e.g.*, monolithic alumina, zirconia, zirconia-toughened alumina and silicon nitride), and exposed to accelerated aging.

By employing various surface spectroscopy tools, this study enabled to verify a method for determining oxygen stoichiometry in UHMWPE/ceramic couples subjected to static contact in a hydrothermally activated environment.

Chapter 2
Theoretical background

2.1 Hip anatomy

In anatomy, the term articulation refers to the junction of two skeletal segments, allowing the movement [1]. Each joint is specialized in shape and structural components, to control the type and range of motion of the bones.

The hip joint, in particular, connects the head of the femur with the acetabular cup of the iliac bone. It is a synovial, multi-axial ball and socket joint (Figure 2), which allows a large number of movements (compatible with the locomotives activities), in particular in three directions: flexion/extension, abduction/adduction and intra/extra-rotation.
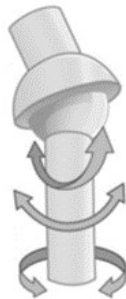
Figure 2: Ball and socket joint – hip joint

The coxal bone, known also as hip-bone, is a flat bone that along the sacrum and the coccyx ends up in the pelvis. During the skeletal growth, three bones (the pubis, the ischium, and the ilium) merge to form the coxal bone once they reach skeletal maturity (Figure 3). The articulation between the coxal bone and the femur form then the hip joint. At the center of the outer surface of the coxal bone there is a hemispherical cavity called the acetabulum. The entire inner surface, with the exception of the central region from which depart the ligaments, is covered with a layer of cartilage. If absent, sliding would cause the deterioration of the bones [4]. The edge of the acetabulum is covered by a soft fibrocartilaginous tissue of a horseshoe shape, said labrum, which increases the depth of the acetabulum. The labrum has many functions, including the absorption of the trauma, the lubrication of the joint, the pressure distribution and the increase of the stability of the joint [6].

The femur is the thigh bone (Figure 4). It allows a large number of movements and is composed of two projecting ends said epiphysis and a body said diaphysis. The femoral head has a hemispherical shape, complementary to the concavity of the acetabulum. It is covered by cartilage, with the exception of the central part (called the fovea) where the ligaments fit.

The cartilage is thicker in correspondence of the upper surface of the femoral

head, where is concentrated a greater weight. Even if the surfaces are mutually curves, the hip joint is formed by two non-congruent shapes and this implies limited contact, which slightly increases with increasing load. This allows distributing the load and protecting the cartilage from excessive stress.
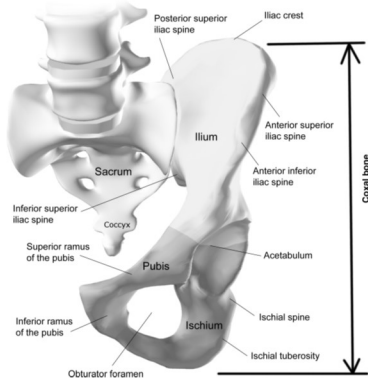
Figure 3: Pelvis schematization
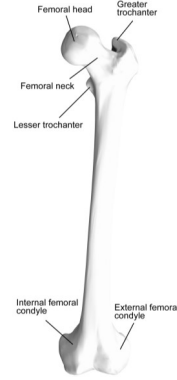
Figure 4: Femur schematization

The cartilage that covers the acetabulum and the femoral head reduces friction and compressive forces acting on the coupling during normal activities and allows smooth, pain free movements. The hip joint is also lubricated by the synovial fluid, which reduces the friction of the joint surfaces [7].

The joint is sealed by the articular capsule, constituted by dense connective and fibrous tissue. The capsule contains the synovial fluid and forms a sleeve around the bones forming the joint. These bundles of collagen fibers adhere firmly to the bone. Their thickness and orientation depends on the stress magnitude in the various joint areas. Three ligaments, (iliofemoral, ischiofemoral and pubofemoral) further reinforce the articular capsule by restricting joint movement (Figure 5). The capsule, the intra- and extra-capsular ligaments and muscles stabilize the joint and keep the bones in place, avoiding the dislocation [8].

The hip joint must be able to support the full weight of the body on one leg [9]. Since it connects the lower limbs to the trunk, and is therefore involved in the transmission of the weight (having also to withstand loads 3 times the weight of the body), it has considerable mechanical requirements [10].
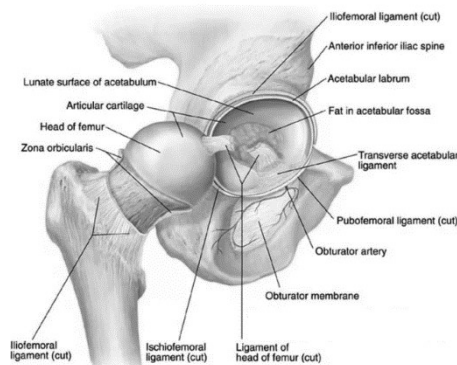
Figure 5: Hip joint and articular capsule

2.2 Main hip diseases

Hip diseases are common problems that can affect a wide variety of people. The main diseases that cause pain and disability and are a frequent cause of total hip arthroplasty (THA) in older patients are osteoarthritis and rheumatoid arthritis. In younger patients instead, are post-traumatic arthritis, congenital dislocation of the hip and Legg-Calvé-Perthes disease [11].

The most common diagnosis is osteoarthritis (≈90% of cases), followed by the fracture of the femoral neck (≈4%), osteonecrosis (≈4%), developmental dysplasia (≈1%) and arthritis rheumatoid (≈1%) [12].

Osteoarthritis is a disease that consumes the cartilage between the femoral head and the acetabulum, causing the rubbing of two bones. It is the result of the interaction between mechanical and biological factors that destabilize the balance of synthesis and degradation of chondrocytes and extracellular matrix. The joint becomes pitted, eroded and uneven, causing pain, instability, stiffness and in some cases movement limitation and limp. Therefore, it can greatly affect the quality of life of patients [13]. It 'a degenerative joint disease, though it is more common in patients over 50 years of age and female, and it afflicts the hips more than other joints [14]. Osteoarthritis has a multifactorial etiology; the onset may in fact be due to the interaction between genetic risk factors that seem to be related to the development and progress of the disease, and systemic factors, such as age, sex, obesity, ethnicity, genetics, abnormalities in the development, nutrition, etc. [15]. Current procedures for the treatment of osteoarthritis are classified as surgical or non-surgical, that can be pharmacological and non-pharmacological (both intended to reduce pain and improve mobility). Both surgical and non-surgical procedures deal with the consequences, such as pain and loss of function, but do not cure the causes [16].

Rheumatoid arthritis is a chronic inflammatory disease due to an autoimmune disorder. Although similar to osteoarthritis in symptoms, it is not due to a "wear and tear" phenomenon. The exact causes are not yet known, but they are probably a combination of genetic and environmental factors. The underlying mechanism of the disease consists in the attack by the immune system, leading to joint inflammation, pain, swelling, loss of motion and deformity. Rheumatoid arthritis is characterized by synovial proliferation and by influx of a variety of inflammatory cells [17]. In the past, the treatment of rheumatoid arthritis was aimed at reducing the activity of the disease, until a low activity state, as there were no alternative effective treatments [18]. However, its treatment is substantially improved over the past 20 years. The treatment can be brought to a state of remission or low activity before patients develop permanent deformation, functional disability or systemic morbidity and mortality [19].

Congenital dysplasia (CDH) or *Developmental dysplasia of the hip* (DDH) is a condition that lasts a lifetime: patients are born with an anatomic shape from slightly to severely altered, deformed or non-aligned, that does not allow the development of the normal wear pattern [20]. In hips affected by dysplasia, the tight coupling between

4

the femoral head and the acetabulum is lost, and the head may not be in the acetabulum [21]. The etiology of DDH is still largely unknown. The risk factors associated with developmental dysplasia include female gender, intrauterine breech position, eldest son and family history. The dislocation may be bilateral or unilateral. If the diagnosis of DDH occurs within the first few weeks of life, there is a 95% success rate of treatment of the disorder. If DDH is not diagnosed early, the normal hip development may be compromised [22].

Legg-Calvé-Perthes disease is a childhood disease that starts from the interruption of blood flow to the femoral head. Because of this, the bone dies by osteonecrosis, or avascular necrosis, stops growing and collapses. Healing then occurs by infiltration of new blood vessels in the dead bone and by removal of necrotic bone. This leads to a loss of bone mass and weakening or deformation of the femoral head [23]. The etiology of LCPD is idiopathic, but it is likely to be multifactorial and may be genetically influenced. The causes of the interruption of the blood supply of the femoral head have not yet been established, but they could be the obstruction of the vessels by lipid particles or the dislocation of the hip after a trauma. A number of factors have been implicated, including heredity, trauma, endocrine, inflammatory or nutritional factors and altered circulation [24].

2.3   Hip replacement

Hip replacement is usually performed when other treatments, pharmacological or otherwise, do not lead to the desired effects. The aim is to eliminate pain and to improve the mobility, the functionality of the damaged joints and in general the quality of life [4].

Hip replacement surgeries can be divided into three broad categories: partial or total replacement (defined primary procedures) and revision of the replacement.
If only one part of the joint is damaged, it may be advisable to perform a partial replacement. In many cases the acetabulum is left intact while the femoral head is replaced, using components similar to those used for total hip replacement. The articular surface can be also partially replaced by resurfacing.

The revision operations are instead re-operations of hip replacements in which one or more components of the prosthesis need to be replaced, removed or added. Major revisions imply the replacement of the femoral stem or the acetabular cup (at the interface with the bone); minor revisions consist in the replacement of the femoral head and the acetabular liner. Much of the revision surgeries are major (85% of the total), and most commonly they concern the acetabular cups [12].

The total hip arthroplasty consists in the surgical replacement of the hip with an artificial prosthesis: the femoral head and neck are removed and replaced by a prosthetic implant [25]. This reconstructive procedure allowed the improvement of the treatment of joint diseases that respond weakly to conventional medical therapy. It is currently one of the most realized procedures in the orthopedic practice.

The total hip arthroplasty (THA) has become one of the most effective surgical interventions in terms of costs and success. After over 40 years of improvements, it guarantees both high clinical success rates in the short term and long term lasting results. With current technology, patient satisfaction, pain relief and long-term implant survival are excellent. The success depends on many factors, including the type of the prosthesis, the pre-operative conditions, the correct surgical execution, adequate post-operative rehabilitation and patient motivation [4].

2.4 THA prosthesis design

Nowadays available prosthetic implants are made from different materials and with different designs. In fact, it does not exist a unique implant that is the most appropriate for all the patients. The implant must be selected on the patient's needs, life expectancy and level of physical activity, but also on the quality and size of the bone [4].

To replicate the hip movement, the prosthetic implant for THA is generally composed of four components (Figure 6): the stem, the femoral head and the two layers of the acetabular cup (outer shell and inner liner).
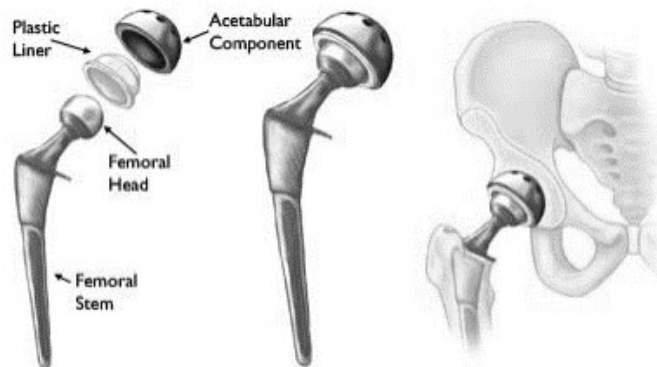
Figure 6: individual components of a total hip replacement (left), all components merged into an implant (center), the implant fitted into the hip (right)

The *femoral stem* replaces a large portion of the femoral bone; it is in fact positioned in the medullary canal, following the resection of the femoral head. Its main function is to maintain fixed the femoral part of the prosthesis and provide a uniform load distribution on the surrounding bone [3]. It is the load-bearing part of the system. To take the full weight of the body it must have a Young's Modulus (typical property of a material that expresses the ratio between traction and relative elongation) comparable to that of cortical bone. If the material does not have the same hardness of the bone, the surrounding bone is subjected to constant stress; if it is harder the bone will undergo the stress shielding phenomenon (osteopenia), which is the loss of bone density. In fact, according to the law of Wolff the bone remodels depending on the load to which it is subjected. If the load decreases, the bone becomes less dense and therefore inevitably weaker [26]. The selected material must then have additional requirements such as resistance to static and dynamic loads, resistance to mechanical and chemical wear, fatigue strength and biocompatibility. The most suitable materials

for this use are titanium alloys and stainless steel.

In addition, the length of the stem affects the stability of the prosthesis. Longer stems guarantee a better stability but also have negative aspects: a greater amount of bone is removed and the contact surface between bone and implant increases, with consequent more likely complications in the case where it is necessary a revision surgery. It was then reached a compromise on the length of the stem, which generally varies between 130 and 140 mm (Figure 7) [27].

Most of the stems are manufactured using the titanium alloy Ti-6Al-4V (6% aluminum, 4% vanadium) due to various properties such as mechanical strength, corrosion resistance and excellent biocompatibility, which make it one of the materials most suitable for orthopedic applications [28]. Some disadvantages are, however, the stress shielding, since the modulus of elasticity of about 100 GPa is much higher than that of the surrounding bone, and migration, a result of large micromotions at the bone-implant interface. Both of these disadvantages can lead to implant loosening and bone resorption, limiting the longevity of the prosthesis.

So far, some materials/design have been proposed to overcome the problems related to the stress shielding and improve the lifetime of the implants. One approach involves the use of a titanium-based alloy, with an elastic modulus between 60 and 80 GPa. Alternatively, zirconia alloys are equipped with sufficient strength, corrosion resistance and high biocompatibility. These alloys with low modulus of elasticity, although still 4 or 5 times higher than that of the bone, are able to reduce the stress shielding and increase bone remodeling [29, 30].
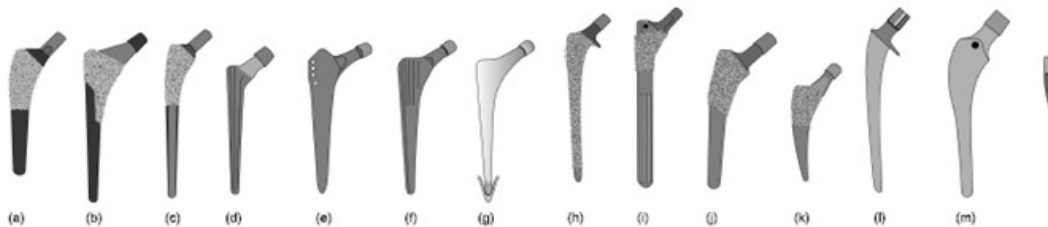
Figure 7: Different modern stems for hip arthroplasty

Femoral heads are generally made from ceramic (in particular alumina and zirconia) or metallic (Co-Cr-Mo alloys or stainless steel) materials. Ceramic femoral heads have a smoother surface than metal heads, with a consequent lower friction rate. However their main disadvantage is the higher brittleness and fracture risk respect to metal heads [3].

Size and properties of the materials at the joint interface can be selected according to the needs of the patient, to optimize the function and lifetime of the implant, mitigating the associated risks. The size of the femoral ball is measured as the outer diameter of the head. The most common sizes are 28 mm, 32 mm and 36 mm. Femoral heads with 22.25 mm diameter were common in the early modern prostheses, while now they are available also larger (38-54+ mm) (Figure 8). The diameter of the femoral head plays a significant role in determining the range of motion and the stability against dislocation. In fact, these parameters increase linearly with the

diameter. The aim is to obtain the maximum diameter and at the same time the lowest roughness, to reduce friction and wear [31].
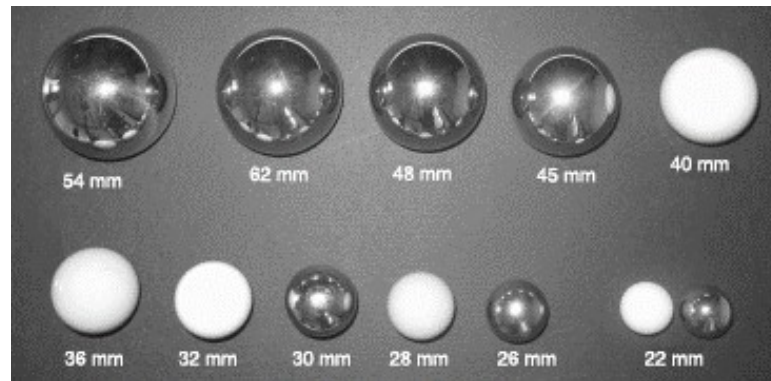
Figure 8: Different available sizes of femoral heads

However, the choice of the size must take into account the multi-component nature of the THA implants. Polyethylene liner do not adapt well to large femoral heads, as the increased swing distance causes increased wear. For this reason, non-smooth materials are not suitable for large femoral heads [3]. Larger femoral heads imitate more faithfully the anatomy of the femur (heads vary in size between 40-54 mm, smaller in women). The advantage of lager femoral heads is hence a greater range of movement, resulting in an improved quality and number of physical activities that can be carried by the patient [4].

The *acetabular cup* (Figure 9) replaces the worn socket of the joint. Its dimensions vary according to the physique of the patient and must be compatible with those of the femoral head.
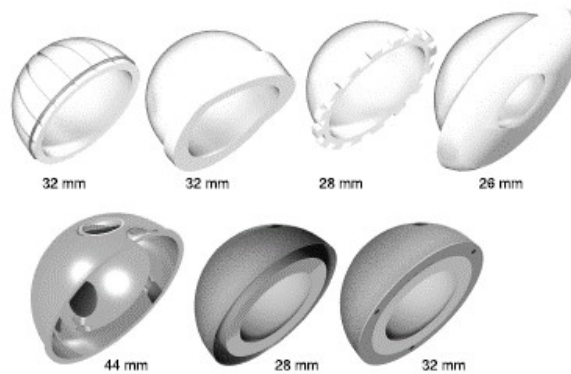
Figure 9: Evolution, in terms of size, of the acetabular cups

The orientation of the acetabular cup and the lip augmentation can increase post-operative stability, decreasing the chance of dislocation caused by the impingement of the prosthesis during rotation [32]. The predisposition to dislocation is in fact caused by the incorrect orientation. For this reason it is very important to get the correct anteversion (tilting forward) and vertical tilt of the acetabular component. The "safe zone" [33] defines the position in which instability is statistically lower. This corresponds to an angle between 30 and 50 ° of vertical tilt and between 5 and 25 ° of anteversion. A cup with few degrees of anteversion and almost vertical decreases the

chance of dislocation [34].

In hard-on-soft prosthesis, the liner is made from polymeric materials, usually high molecular weight polyethylene (UHMWPE) or a highly cross-linked (HXLPE). Hard-on-hard implants instead are made from metal alloys (such as Co-Cr-Mo) or ceramic materials (such as alumina and zirconia). The liner is then inserted in a metallic outer shell (made from titanium or stainless steel) which ensures the mechanical stability [3].

Implants can be monolithic or modular. Chanley's original prosthesis was one piece called "monoblock". Conversely, today implants tend to be composed of several pieces, customizable and adaptable to the needs and to the patient's anatomy.
Both the femoral stem and the acetabular cup can be modular or monoblock. The stem can be a single piece with the femoral head or it can be modular, consisting of several parts (stem, neck and femoral head), with different possible angles. A conical locking mechanism (similar to a Morse taper) holds together the various pieces. In a similar way the acetabular cup can be monoblock or modular, i.e. constituted of a single piece (metal or polymeric), or formed by two components: an outer metal shell, fixed to the pelvic bone, and a liner, fixed inside the shell [4].

A prosthetic implant can then be fixed to the bone with different strategies: cemented, cementless and hybrid fixation. The various methods require different choices in material, design and surface finish of the prosthesis components [3].

Cemented implants (Figure 10, left) are still common. Bone cement works as a space-filler and its fixation to the bone is purely mechanical, for interdigitation in the surrounding cancellous bone. The basic component is the methyl-methacrylate monomer (MMA), which polymerizes to form poly-methyl-methacrylate (PMMA). The characteristics of the different commercially available cements then depend on the exact chemical composition and on the cementing technique. Slight differences have sometimes shown dramatic changes in the mechanical and clinical performances [35]. The cementation techniques have evolved over the past 40 years, and the so-called third-generation cementing has substantially improved the long-term outcome [36]. The cemented acetabular cup is usually completely of polyethylene. The stem has usually a smooth surface, more or less opaque. The cement allows transmitting the mechanical stresses, which press on the prosthesis, to the surrounding bone [37].

Uncemented implants (Figure 10, right) have regained popularity in the 1980s, when the bone cement was believed to be responsible for periprosthetic osteolysis [38]. This type of fixation includes a primary stability by press-fitting or screwing the components in the bone, and a secondary fixation for bone ongrowth and ingrowth on the surface of the implants. To achieve this, the surface is roughened by sandblasting, application of porous coatings or coating with hydroxyapatite (HA), to stimulate bone growth around the implant. Since the stability depends on the bone regrowth, these implants require a longer healing time. The uncemented cup generally consists of two hemispherical pieces: an outer metal shell and an inner polyethylene liner mechanically fastened in the shell. Additional features include in sometimes spikes, screws, pegs or fins, to provide additional fixation. The femoral stem is typically

modular, made from titanium and with variables shape and surface finishing. This type of fixation is usually recommended for young, active patients with a good bone quality. Generally, its durability is good or excellent [39], even if reduced on the long-term because of wear and osteolysis [40].

In *hybrid implants* one of the two components, usually the acetabular cup, is inserted without cement while the other, usually the femoral stem, is cemented. This technique was introduced in the 1980s, to exploit the advantages of both fixation methods.
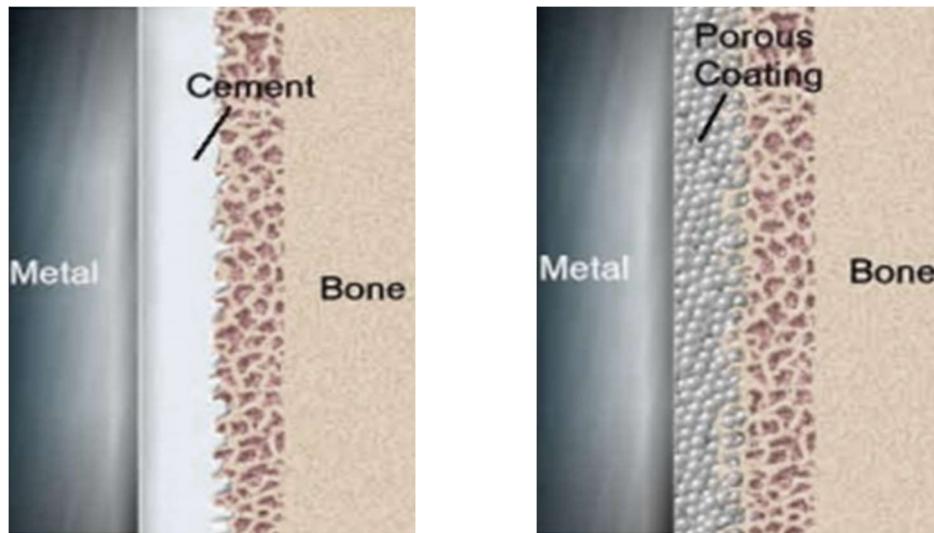
Figure 10: Schematic illustration of cemented (left) and uncemented (right) fixation methods

Trials on cemented versus cementless arthroplasty indicate less pain and better function with cemented arthroplasty [41]. The results from the Australian National Joint Replacement Registry also indicate a higher risk of revision for uncemented systems [12]. Moreover, cementless implants are generally more expensive than cemented ones, but the choice resides ultimately in the preference of the surgeon.
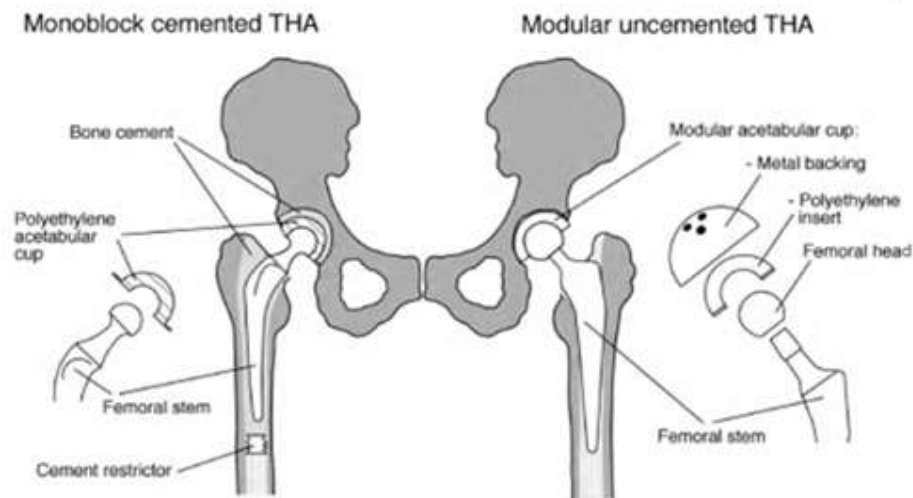
Figure 11: Schematics of monoblock, modular, cemented and uncemented implants

2.5   Implant materials

In the last half century, there have been many advancements in design, materials and implanting techniques of artificial hip joints, leading to a high rate of success.

The major difference between the different implants resides in the material forming the prosthesis. However, they all need to possess some fundamental properties, such as:

- biocompatibility: they must work in the body without triggering a local or systemic immune response
- no cytotoxicity and carcinogenicity
- resistance to corrosion, degradation and wear, while maintaining their strength and form for prolonged periods
- mechanical properties similar to those of the replaced structures. They must be strong enough to withstand loads, flexible in order to endure stress without fracturing and able to slide smoothly against each other
- compliance with the highest standards, but at the same time with reasonable costs
- possibly with osteoinduction, osteoconduction and osseointegration properties, to improve the function of the implant in the body [42].

Currently different combinations of materials, with different physical properties, are possible. Typical pairings (Figure 12) are metal on plastic (MOP), ceramic on plastic (COP), metal on metal (MOM) and ceramic on ceramic (COC).

Figure 12: Metal on plastic (MOP), ceramic on plastic (COP), metal on metal (MOM) and ceramic on ceramic (COC) pairings, respectively

Each of these pairs have different advantages and disadvantages, as well as different wear rates. As shown in the histogram (Figure 13), the coupling with a higher volumetric rate of consumption is metal on polyethylene [43]. Wear in ceramics on polyethylene implants is instead more than halved compared to MoP. Hard on hard couplings, like metal on metal (CoCrMo) and ceramic on ceramic (Al_2O_3), have the lowest wear rate, since they generate less particulate than hard on soft implants [44, 45]. They are therefore usually recommended for younger and very active patients.

Nowadays, however, there is still no unanimous consent between the orthopedic community about the best "bearing material". Each company has different models and every surgeon has his preferences, also based on his experience.
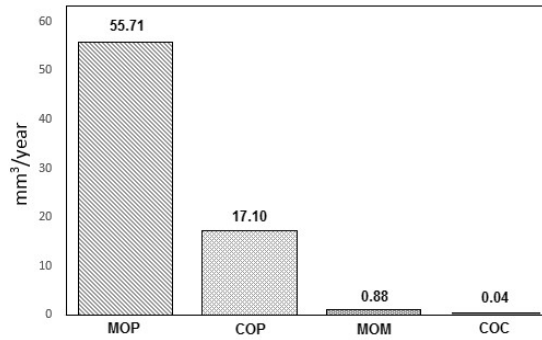
Figure 13: Different polyethylene wear rates, depending on the counterpart material

2.5.1   Metal on metal

The first generations were developed in the 1960s, but abandoned in the 1970s following the introduction of the low friction arthroplasty by Chanley. In the 1980s, it was then developed a second generation of metal on metal implants, with a better interface and composed of metal alloys with higher hardness.

The medium and long-term results of this type of implants showed excellent durability, but over the decades there has been growing concern about the release of metal ions. Inside of tissue cells, nanoparticles due to wear are exposed to a series of oxidative mechanisms that have the purpose of eliminating the foreign body. This leads to the generation of metal ions [46]. Despite the very low volumetric wear rate, the number of small metal particles and their surface area are very high [47]. The metal particles and ions can also spread throughout the body through the blood or lymphatic circulation, with harmful effects on the immune and nervous systems, and on the kidneys [48]. Cobalt ions are the most commonly encountered and their level is found even 5-6 times higher [49].

In general, this type of implants consists of cobalt-based alloys or stainless steel. They offer the advantage of less wear, with less inflammation and bone loss. They also allow the use of larger femoral heads (44-54mm), in imitation of the real hip size, ensuring greater stability with reduced risk of dislocation and without increasing the wear rate despite increased sliding distance.

2.5.2   Metal on polyethylene

The standard metal head-polyethylene cup coupling is in use since the 1960s. The MoP implants are the most tried and tested. With its performance and durability, MoP has been the leading artificial hip component material chosen since hip replacement surgeries have first been performed. It is also the least expensive. However, with time the polyethylene particles, formed because of wear, can be a source of infection, necessarily leading to a revision. To reduce friction, femoral heads of small size (28-36 mm) are used. The advancement in the materials and the use of Ultra Highly Cross-Linked (UHXLPE) or Ultra High Molecular Weight (UHMWPE) polyethylene, stable

and reliable plastic materials, has allowed reducing further the risk of wear. [50]

2.5.3 Ceramic on ceramic

Fully ceramic implants have been used since the 1980s. The ceramic materials are known to be fragile, with high hardness and very durable. Having extremely smooth surface they show extremely low wear rates, reducing the risk of inflammation, bone loss or systemic distribution of the wear products. Compared to other materials there is no cellular reaction to the debris, since the wear product has no toxic effects in the human body. They also have excellent lubrication and friction properties. Thanks to its properties, this type of implant is generally recommended for younger and very active patients.

The major disadvantage the low resistance to fracture of ceramic materials: a single critical defect can lead to catastrophic failure since they are not flexible and are therefore unable to deform [51]. Another disadvantage is the squeaking. The incidence varies widely, from 1 to 21%, and the exact mechanism is not yet clear [52].
Aluminum oxide (Al_2O_3) and zirconium oxide (ZrO_2) are the most widely bearing surfaces among the ceramic materials.

2.5.4 Ceramic-on-Polyethylene

These type of implants were introduced in the 1970s to reduce the volume of polymeric debris in the MoP couplings. This type of installations represent a good combination of two reliable materials. The ultra-smooth surface of the ceramic femoral heads significantly reduces the wear rate on the surface of the polyethylene respect to other femoral heads [53]. CoP represent a solution to the disadvantages of CoC cupling, such as the squeaking and the possibility of fracture of the ceramic material [54]. Currently hard-on-soft joint is the most conventional, with an excellent positive statistic. The most common coupling is alumina-based femoral head vs. polyethylene acetabular cup.
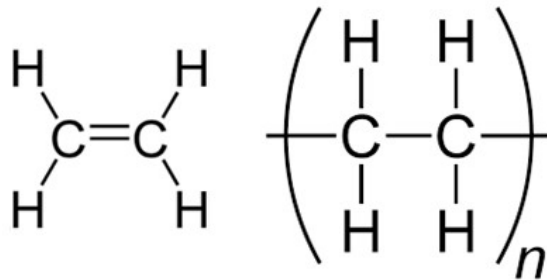
Chapter 3
Materials

3.1 Polyethylene

Polyethylene is a polymer formed from ethylene (C_2H_4), a gas with a molecular weight of 28g/mol. The chemical formula for polyethylene is $(C_2H_4)_n$, where n is the degree of polymerization (Figure 14).

Figure 14: Schematic structures of ethylene (left) and polyethylene (right)

There are different types of polyethylene, which differ in molecular weights and chain architectures: low density (LDPE), linear low density (LLDPE), high density (HDPE), ultra-high molecular weight polyethylene (UHMWPE). LDPE and LLDPE have branched and linear chain architecture respectively, and a typical molecular weight of less than 50,000 g/mol. HDPE is a linear polymer, provided with a molecular weight up to 200,000 g/mol. UHMWPE has molecular chains that consist of as many as 200 thousand ethylene repeated units, meaning a content of approximately 400 thousand carbon atoms. Its molecular weight, that cannot be measured directly by conventional means and must be inferred by its intrinsic viscosity, is 6 million g/mol. Speaking of physical and mechanical properties (Table 1), UHMWPE has the highest ultimate strength and impact strength.

PROPERTY	HDPE	UHMWPE
Molecular weight (10^6 g/mol)	0.05-0.25	3.5-7.5
Melting temperature (°C)	130-137	132-138
Poisson's ratio	0.40	0.46
Tensile modulus of elasticity (Gpa)	0.4-4.0	0.5-0.8
Tensile yield strength (Mpa)	26-33	21-28
Tensile ultimate strength (Mpa)	22-31	39-48
Tensile ultimate elongation (%)	10-1200	350-525
Impact strength	21-214	>1070 (no break)
Degree of crystallinity (%)	60-80	39-75

Table 1: Typical average physical properties of HDPE and UHMWPE

More relevant from the clinical point of view, UHMWPE is more abrasion and wear resistant respect to HDPE, as shown by the data collected using a contemporary multidirectional hip simulator [55]. The volumetric wear rate (Figure 15) is in fact 4.3 times greater for HDPE than that for UHMWPE.
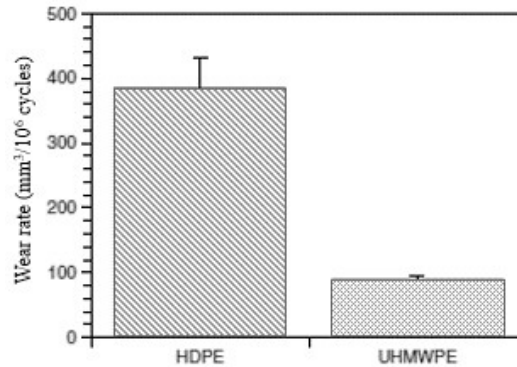
Figure 15: Comparison of wear rates of HDPE and UHMWPE in a multidirectional hip simulator

UHMWPE architecture is characterized by tangled, not static chains that become mobile at elevated temperatures. When the temperature is below the melting point, the molecular chains tend to rotate about the C-C bond, creating chain folds. This allows the molecules to arrange themselves in ordered, sheet-like regions called crystalline lamellae, embedded within a disordered amorphous phase (Figure 16). Crystalline phases might have different degrees of orientation, depending upon various factors, including molecular weight, processing conditions and environmental conditions.
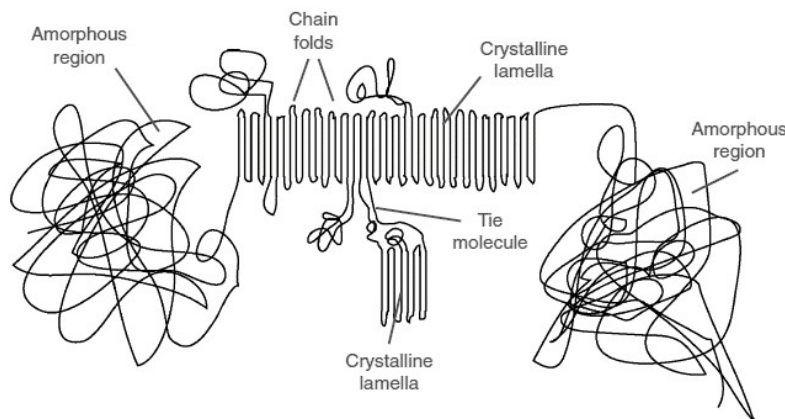
Figure 16: Morphological features of UHMWPE

Crystalline lamellae are micrometic in size, ranging from 10 to 50 μm in length and from 10 to 50 nm in thickness [56], while the average space between them is approximately 50 nm [57]. They diffract the visible light, giving UHMWPE a white and opaque appearance. Above the melting temperature of the lamellae (around 137°C) UHMWPE appears instead translucent. By means of transmission electron microscopy, UHMWPE can be magnified up to 16 thousand times, allowing observing its crystalline morphology. The staining with uranyl acetate makes the amorphous

region turn grey, while the crystalline lamellae appear as white lines with a dark outline. The composite nature of UHMWPE, characterized by an interconnected network of amorphous and crystalline regions (Figure 17), appears clear.
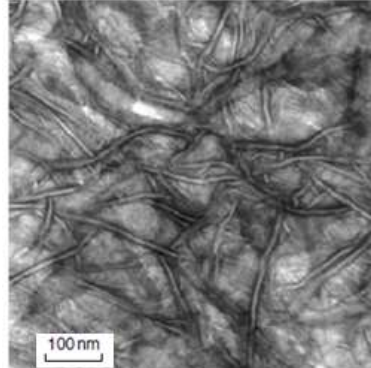
Figure 17: TEM micrograph, showing amorphous and crystalline phase of UHMWPE

UHMWPE can be regarded as a three-phase material, in fact in addition to a fully crystalline and a fully amorphous phases it contains in the intervening spaces an intermediate amorphous-crystalline inter-phase, partially ordered, called third phase [58]. Some investigations demonstrated that chains involved in the third phase lack of lateral order [59]. Other studies showed that this intermediate phase is anisotropic and exhibits properties that are intermediate between that of a crystalline solid and of an amorphous melt [60].

The properties of polymeric materials are generally temperature depending. Most polymers undergo three major thermal transitions, at glass transition temperature (T_g), melt temperature (T_m), and flow temperature (T_f). In particular, below the glass transition temperature (T_g) the polymer chains behave like a brittle glass and have insufficient thermal energy to slide past one another. In this case the material responds to mechanical stress by stretching (or rupture) of the bonds constituting the molecular chains. UHMWPE glass transition temperature occurs around -120°C.

Raising the temperature, the amorphous regions within the polymer gain mobility. Around 60-90°C the smaller crystallites begin to melt. Differential scanning calorimetry (DSC) allows measuring the melting behavior of UHMWPE. It measures the amount of heat necessary to increase the polymer temperature. The DSC trace for UHMWPE (Figure 18) shows the melting temperature (Tm) peak at around 137°C, when the majority of the crystallite have melted. Thicker and more perfect crystals melt at a higher temperature than smaller imperfect crystals. Moreover, the area underneath the melting peak is proportional to the crystallinity of the UHMWPE. DSC provides also a measure of the total heat energy per unit mass (change in enthalpy ΔH), required to melt the crystalline regions within the sample. By comparing the change in enthalpy of a UHMWPE sample to that of a perfect 100% crystal, it is possible to calculate the degree of crystallinity of the UHMWPE. Most bulk UHMWPEs are about 50% crystalline.

When raising the temperature above the melting temperature a polymer may

undergo a flow transition and become liquid. Polyethylene with a molecular weight below 500,000 g/mol can undergo such flow transition (Tf), while UHMWPE, due to its ultra-high molecular weight, does not exhibit a flow transition: the entanglement of the immense polymer chains prevents it from flowing.
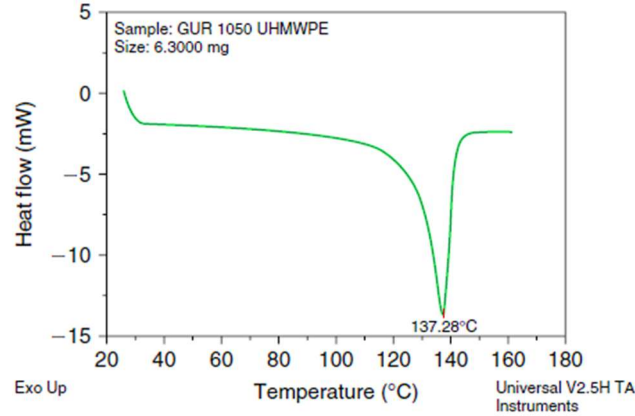
Figure 18: Differential scanning calorimetry trace for UHMWPE

UHMWPE is used for biomedical applications because of its high impact resistance, ductility and stability in contact with physiological fluids. Its first use dates back to the 1970's, with Charnley's low friction hip prosthesis [61]. Nowadays this is the most used polymeric material for human orthopedic implants, such as total hip or knee replacements.

3.1.1 UHMWPE processing

To produce UHMWPE, ethylene gas must be first polymerized. Second, the polymerized UHMWPE, in the form of resin powder, has to be consolidated into sheets, rods, or near-net shaped implants. Finally, it needs to be machined into its final shape (Figure 19).
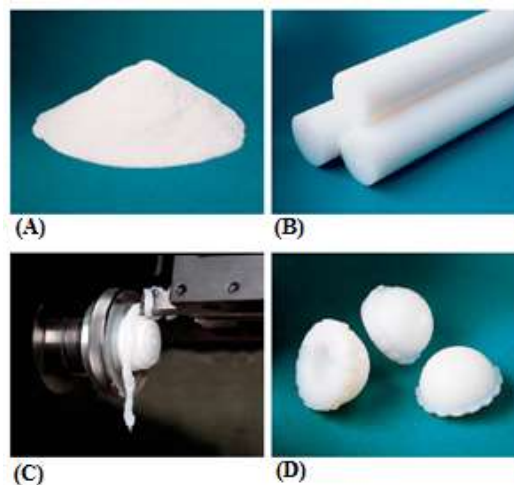
Figure 19: Processing steps in the manufacture of UHMWPE implants: resin powder (A), resin powder consolidated in semi-finished rods (B), machining of the rods on a lathe (C), finished UHMWPE acetabular components (D)

Each of these steps could produce subtle alterations of UHMWPE properties. Machining can only affect topography and appearance of the surface, while changes in the polymerization and conversion can affect also the physical and mechanical properties of UHMWPE. Details of polymerization, conversion and machining procedures are mainly proprietary, so little is reported in public domain literature. The requirement for UHMWPE for medical use are specified in two standards: ASTM F648 and ISO 5834-1. UHMWPE resins for this purpose are classified in three types, depending upon molecular weight and producer (Table 2).

PROPERTY	REQUIREMENTS	
Resin name	Types 1-2	Type 3 (discontinued)
Trade name	GUR 1025 and 1050	1900H
Producer	Ticona, Inc	Basell Pokyolefins
Ash, mg/kg (maximum)	125	300
Titanium, ppm (maximum)	40	150
Aluminium, ppm (maximum)	20	100
Calcium, ppm (maximum)	5	50
Chlorine, ppm (maximum)	30	90

Table 2: Requirements for Medical Grade UHMWPE Powders (per ASTM 648 and ISO 5834-1)

Impurities of titanium, aluminum, and chlorine are residuals from the catalysis, while trace levels of calcium and ash content depend upon the storage and handling of the powder after polymerization.

Ticona (Germany) produces Type 1 and Type 2 resins, known with the trade names of GUR 1020 and 1050, respectively. The acronym GUR stands for "Granular," "UHMWPE," and "Ruhrchemie". The first digit of the trade name was originally the loose bulk density of the resin (i.e. weight measurement of a fixed volume of loose, unconsolidated powder. The second digit indicates the presence ("1") or absence ("0") of calcium stearate that acts as a scavenger for residual catalyst components [62]. The third digit is correlated to the average molecular weight of the resin. UHMWPE average molecular weight is routinely inferred from intrinsic viscosity measurements [63]. Average molecular weights, calculated following ASTM D4020-05, are 3.5 million g/mol for GUR1020 and 5.5-6 million g/mol for GUR1050, respectively. The fourth digit is an internal code designation.

Basell Polyolefins (USA) produced instead Type 3 resin until 2002, when it was discontinued. Its average molecular weight is >4.9 million g/mol.

Differences in material properties of converted GUR and 1900 resins are due to variations in the averaged resin particle size, size distribution, and morphology of the resin particles. GUR resins have a mean particle size of about 140 μm, whereas the resin 1900 has a mean particle size around 300 μm [64]. The distribution of particle sizes also varies between the three types of resins. The scanning electron micrographs show that both GUR and 1900 resin powders consist of numerous spheroidal particles, with subtle differences in morphology likely related to catalyst and polymerization

conditions [65].

Since UHMWPE is produced as powder, it must be consolidated under elevated temperatures and pressures because of its high melt viscosity (it does not flow like lower molecular weight polyethylene above the melting temperature). UHMWPE is typically produced by compression molding and ram extrusion. The process of consolidation requires proper temperature, pressure, and time. The precise combinations of these variables remain proprietary [66].

During the process of consolidation, the UHMWPE chains in adjacent resin particles intermingle at a molecular level. The kinetics are promoted by close proximity of the interfaces (at elevated pressures) and thermally activated mobility of the polymer chains (at elevated temperatures). It is a diffusion-limited process, so it requires sufficient time at elevated temperature and pressure for the molecular chains to migrate across grain boundaries.

Compression molding (Figure 20) originated in Germany in the 1950s. It is divided into two main stages. Initially, the molds containing the powder are heated (at about 200-250 ° C) for the time necessary to obtain its homogeneous plasticization, applying a pressure of 10 - 20 bar. Then UHMWPE sheet is pressed between two platens, oil heated and hydraulically actuated from below. The entire press is contained in a clean room to reduce the introduction of extraneous matter into the sheet. Subsequently the mold is progressively cooled to room temperature and pressure is gradually increased, to about 40 bar, to allow a homogeneous solidification of the material. The cooling rate is a function of the desired degree of crystallization. The processing time can last up to 24 h: long molding times are necessary to maintain slow, uniform heating and cooling rates throughout the entire molding process [67].
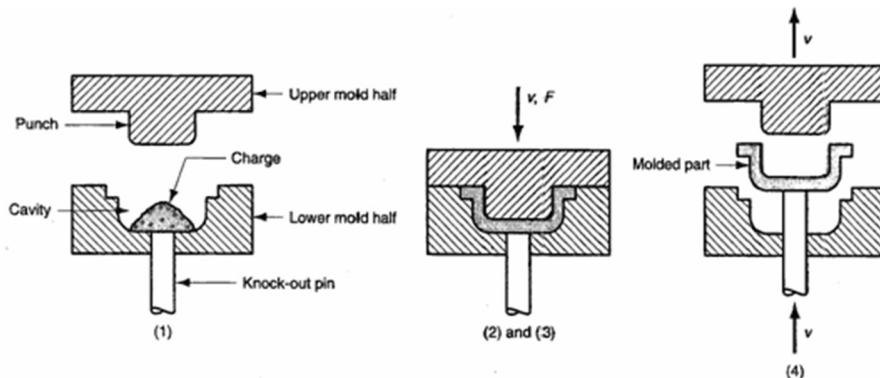
Figure 20: Schematic representation of compression molding process

Ram extrusion of UHMWPE (Figure 21) was developed by converters in the United States during the 1970s. In ram extrusion the polymer is loaded inside the extruder and pushed by a piston with cylindrical section; along this pathway the extruder is heated to temperatures between 180 and 200 °C, to melt the material. The cooling must be carried on with extreme care to avoid the occurrence of internal stresses and the formation of holes or cavities. With this technique UHMWPE rods of cylindrical section, with diameters between 20 and 80 nm, are continuously obtained. Typical production rates are on the order of mm/minute.
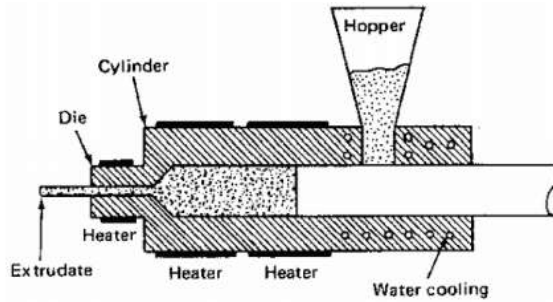
Figure 21: Schematic representation of ram extrusion process

Extruded and compression molded UHMWPEs may have subtle differences in the morphology and fatigue crack propagation behavior. Studies have demonstrated that compression molded UHMWPE has an isotropic crystalline orientation, while in ram extruded UHMWPE the morphology varies slightly depending on the distance from the centerline [68]. Similarly, compression molded sheets have a more isotropic crack propagation behavior compared to ram extruded rods of UHMWPE [69].

Lastly, orthopedic manufacturers machine UHMWPE components into their final form. Manufacturing conditions and the type of UHMWPE (conventional or crosslinked) determine the actual morphology of machining marks [70]. Machining of components consist in milling and turning operations. In some cases, UHMWPE is machined in a shape that approximates the cross-section of the finished implant. Depths of cut, cutting speeds and tool feed rates used to machine UHMWPE components are proprietary, so little information is available about the effect of this parameters on the tribological properties of UHMWPE [71].

Subsequently fabrication, UHMWPE components for total joint replacement need to be packaged and sterilized prior to distribution. Starting from the 1990s, different packaging and sterilization techniques have evolved. Around 1995 UHMWPE was typically sterilized with a nominal dose of 25-40 kGy of gamma radiation in the presence of air. As recently as 1998, all of the major orthopedic manufacturers were either sterilizing using gamma radiation in a reduced oxygen environment or without ionizing radiation, using ethylene oxide or gas plasma. Nowadays a wide range of choices is available for the sterilization of UHMWPE implants (Table 3). This reflects the lack of scientific consensus on which sterilization method provides the most advantageous long-term durability of UHMWPE.

STERILIZATION PROCESS	PACKAGING TYPE	GAMMA RADIATION DOSE
Gamma air	Gas permeable	25-40 kGy
Gamma inert	Barrier packaging	25-40 kGy
Gas plasma	Gas permeable	-
Ethylene oxide	Gas permeable	-

Table 3: Summary of sterilization processes for UHMWPE implants

UHMWPE implants can be sterilized with or without ionizing radiation. Whether packaged in air-permeable or barrier packaging, gamma sterilized UHMWPE

contains macroradicals, *i.e.* very reactive chemical species that react easily with oxygen available in air or dissolved in body fluids. The barrier packages (polymer laminates or metallic foils to block gas diffusion) aim to reduce the oxygen availability, minimizing the oxidation of macroradicals in the UHMWPE, which persist for years after irradiation [72].

During shelf storage, gamma sterilized UHMWPE components undergo oxidative degradation, resulting in an increase in density and crystallinity [73], and in a consequent loss of mechanical properties due to progressive embrittlement [74]. The development of an embrittled subsurface is associated with fatigue damage [75]. Some clinical studies demonstrated that wear particles, produced by in vivo damage to embrittled implant components, are one of multiple potential mechanisms responsible for the onset of osteolysis [76]. Hence, gamma sterilization plays a dual role, preserving implant properties (with beneficial crosslinking) but also initiating a complex cascade of chemical reactions in the polymer, which ultimately result in its oxidation and in the degradation of its properties.

In the 1990s, when gamma sterilization began to be less popular, sterilization of conventional UHMWPE began to use gas plasma or ethylene oxide: industrially viable, alternative methods. These methods do not generate free radicals, preventing the cascade reactions that can subsequently lead to the oxidation of the material during shelf storage. However, sterilization without ionizing radiation has an important drawback: UHMWPE does not receive a tribological benefit associated with radiation-induced crosslinking.

Implants sterilized with gas plasma and ethylene oxide are packaged in gas-permeable packaging, to allow access of the sterilizing medium to the UHMWPE surface.

Ethylene oxide gas (EtO) is highly toxic, it neutralizes bacteria, spores, and viruses. UHMWPE is compatible with EtO sterilization because it contains no constituents that will react with or bind to the toxic gas. The sterilizing efficacy depends upon stringent control of process conditions, as humidity, duration, and temperature [77]. Studies suggest that this sterilization technique does not influence mechanical, physical and chemical properties of UHMWPE [78]. The sterilization is accomplished by diffusion of EtO near the UHMWE surface, for several hours. EtO is then allowed to diffuse out [77].

Gas plasma sterilization, performed at low temperatures, is a relatively new commercially available sterilization method. Gas plasma relies upon ionized gas for deactivation of biological organisms [79]. Gas plasma sterilization is accomplished at low temperatures, below 50°C [80]. Recent studies suggest that it does not affect the mechanical, physical and chemical properties of UHMWPE [81]. In addition, it does not leave toxic residues or involve environmentally hazardous by-products [82]. Because of its recent introduction, retrieval data from *in vivo* UHMWPE components, sterilized using gas plasma, are not yet available.

Some study on wear rates of UHMWPE showed interesting results. McKellop et al. studied UHMWPE wear performance in a contemporary hip simulator following
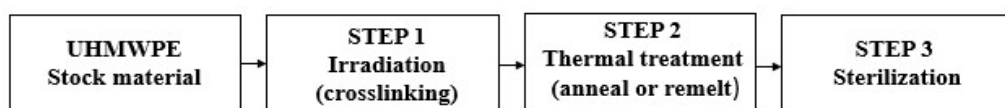
21

gamma irradiation in air, gamma irradiation in an inert gas, ethylene oxide, or gas plasma. Between 2 and 5 million cycles (each million of cycles corresponding on average to about a year of use *in vivo*), the wear rate of the UHMWPE sterilized by either gas plasma or ethylene oxide (40 ± 0.6 mm^3/million cycles) was significantly higher than gamma sterilized UHMWPE (18.5 ± 0.9 mm^3/million cycles) [83]. Wang et al. found a similar trend: after a single 25 kGy dose of gamma irradiation the hip simulator wear rate was more than halved [84].

Clinical studies on the same subject demonstrated that the wear rate of gamma air and gamma inert sterilized components is comparable, while gas plasma sterilized implants have a wear rate approximately two times greater than gamma air sterilized liners [85]. This is mainly because wear processes in hip replacements are dominated by crosslinking. Its beneficial effect dominates over the harmful effects of oxidative degradation. Moreover, since gamma sterilization produces a comparable extent of radiation crosslinking both in air and in barrier packaging, there are no substantial differences between the wear rates of UHMWPE gamma irradiated in air and in an inert gas.

Due to the importance to reduce the wear rates, major research efforts were focused on the development of improved polymeric materials. This led in 1998 to the introduction of highly crosslinked UHMWPE, the so-called "first generation" of UHMWPE [86]. These materials are irradiated with a total dose ranging from 50 to 105 kGy, depending on the manufacturer. Highly crosslinked UHMWPE materials undergo reduced wear, both experimentally and clinically, compared to conventional UHMWPE [87]. Examples of first generation UHMWPE materials are Crossfire™, Durasul®, Longevity™, Marathon™, Prolong™ and XLPE™.

The last step in the production of first generation of highly crosslinked UHMWPE consist in a thermal processing (Figure 22, Step 2). This step was initially proposed to avoid the oxidation observed in gamma sterilized UHMWPEs [88, 89].

| UHMWPE Stock material | → | STEP 1 Irradiation (crosslinking) | → | STEP 2 Thermal treatment (anneal or remelt) | → | STEP 3 Sterilization |

Figure 22: Production steps of "first generation" highly crosslinked and thermally treated UHMWPE

Two main thermal treatments are available: annealing, performed below the melting temperature of the polymer (130-136°C) and remelting, performed above the melt transition.

Remelting consists in heating the polymer to above its melting temperature. It effectively quenches the residual free radicals, improving the oxidative stability of irradiated UHMWPE. This thermal processing eliminates the crystalline domains (i.e. lamellae), releasing the trapped radicals that are provided with enough mobility to find and recombine with each other. The main drawback resides in the fact that it changes the UHMWPE microstructure.
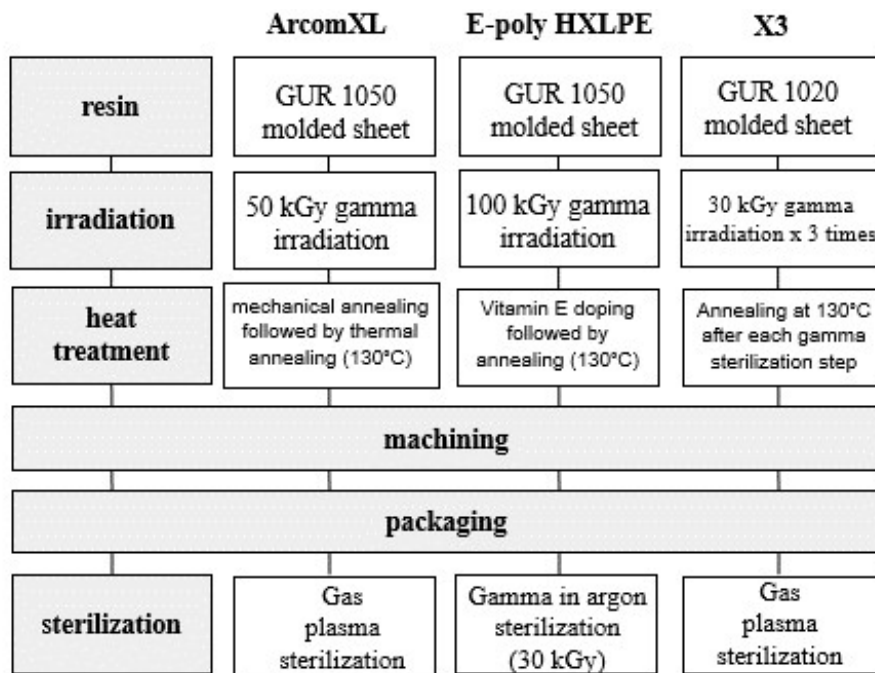
Annealing consists in heating UHMWPE below the melting temperature. It does

not change its microstructure but is not as effective in quenching free radicals.

The choice of the thermal processing can influence mechanical properties, degree of crystallinity and resistance to in vivo oxidation. Post-irradiation thermal processing, regardless of temperature, occurs at ambient pressure [90].

Mechanical properties, such as elastic modulus, yield stress and ultimate stress of a remelted material appear to be significantly lower than the respective properties for an annealed material. Moreover, the annealed material has an average degree of crystallinity higher than the remelted material that results in a greater resistance to plastic deformation. Anyhow, both types of material showed successful overall clinical performance [91].

Starting 2005, due to the increasing attention to in vivo oxidation [76], a new type of UHMWPE, the so-called "second generation" UHMWPE, has been developed and is now commercially available. The intent of this kind of material is to reduce the potential oxidation in vivo, while preserving the bulk properties. Examples of these materials include X3 (Stryker Orthopaedics, USA), ArCom XL and E-Poly (Biomet Orthopaedics, USA) (Figure 23).

	ArcomXL	E-poly HXLPE	X3
resin	GUR 1050 molded sheet	GUR 1050 molded sheet	GUR 1020 molded sheet
irradiation	50 kGy gamma irradiation	100 kGy gamma irradiation	30 kGy gamma irradiation x 3 times
heat treatment	mechanical annealing followed by thermal annealing (130°C)	Vitamin E doping followed by annealing (130°C)	Annealing at 130°C after each gamma sterilization step
	machining		
	packaging		
sterilization	Gas plasma sterilization	Gamma in argon sterilization (30 kGy)	Gas plasma sterilization

Figure 23: details of manufacturing procedure of different types of "second generation" UHMWPE materials

In 2002, J.H. Dumbleton and A. Wang filed a patent disclosure for the new UHMWPE material X3. This material has little to no free radicals thanks to a sequential process integrating irradiation and annealing: a low dose of radiation was followed by annealing, the process was then repeated. In 2005, X3 was cleared for clinical use. To produce X3 UHMWPE compression-molded GUR 1020 is chosen over GUR 1050 due to its higher ductility and impact strength. The material undergoes then a sequential process divided in three identical cycles, each including 30 kGy irradiation followed by annealing for 8 hours at 130°C. The cumulative radiation dose is 90 kGy.

Components are then machined, packaged and sterilized using gas plasma.

As shown in Table 4, the sequential irradiation and annealing process is much more efficient for crosslink formation and free radicals elimination [92].

| STEP	PROCESS	Free radical concentration (10^{14}spins/g)	Crosslink density (mol/dm³)
1	30 kGy irradiation (I cycle)	1561 ± 41	0.07 ± 0.01
2	Annealing (I cycle)	None detected	0.09 ± 0.01
3	30 kGy irradiation (II cycle)	1663 ± 36	0.13 ± 0.02
4	Annealing (II cycle)	7 ± 3	0.17 ± 0.02
5	30 kGy irradiation (III cycle)	1719 ± 45	0.23 ± 0.02
6	Annealing (III cycle)	9 ± 2	0.28 ± 0.03
Single	90 kGy + annealing	68 ± 7	0.11 ± 0.02

Table 4: Free radical concentration and crosslink density for each step of the sequential process (irradiation and annealing), compared to single process

The oxidation resistance of X3 has been evaluated in a variety of environments. The results of aging for 14 days at 70°C in 5 atmospheres of oxygen (ASTM F2003) are shown in Figure 24. Different types of polyethylene were tested: X3, N2/Vac (conventional UHMWPE), virgin UHMWPE and UHMWPE irradiated to 90 kGy and then annealed (90TS). X3 and virgin UHMWPE exhibited minimal oxidation, while N2/Vac showed subsurface oxidation. The 90TS showed oxidation intermediate between the other tested materials [92].

Accelerated aging of thin films of material, 180 μm thick, at 90°C in air confirmed that the oxidation resistance of X3 is similar to that of virgin UHMWPE (Figure 25).
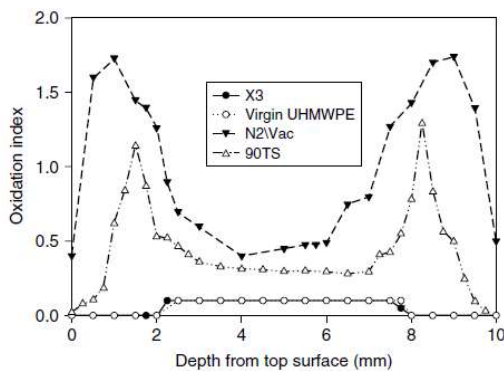
Figure 24: Oxidation index as a function of depth after accelerated aging
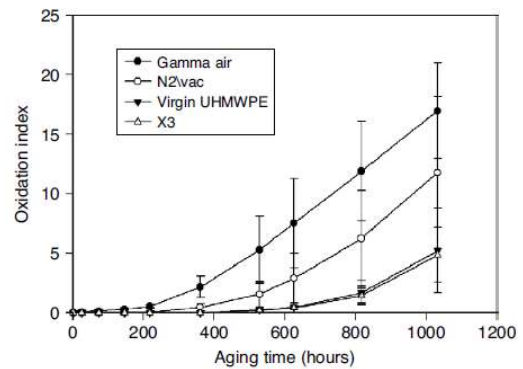
Figure 25: Oxidation index as a function of time with thin films in air at 90°C

Tensile testing after accelerated aging (following ASTM F2003) do not change the tensile properties of X3 (Table 5) [93].

MATERIAL	AGING	Yield strength (Mpa)	Tensile strength (Mpa)	Elongation (percent)
Virgin UHMWPE	Yes	22.1 ± 0.5	57.0 ± 3.7	418 ± 19
	No	22.7 ± 0.6	57.5 ± 5.5	422 ± 17
X3	Yes	23.5 ± 0.3	56.7 ± 2.1	267 ± 7
	No	23.6 ± 0.2	56.3 ± 2.3	266 ± 9

Table 5: Tensile properties of virgin UHMWPE and X3 before and after aging (ASTM 2003)

Functional fatigue testing was carried out according to ASTM International STP 1445 protocol [95]. Percentage survivorship at 1 million loading cycles are shown in Table 6. X3 had higher survivorship (89%) than Crossfire (79%) or N2/Vac (80%) [94].

MATERIAL	Number tested	Number failed	Survivorship (%)
N2/Vac	10	2	80
Crossfire	14	3	79
X3	9	1	89

Table 6: Survivorship of N2/Vac, Crossfire and X3 insert after fatigue testing

Wear testing was carried out for a total of 10 million cycles, using MTS hip joint simulators, reproducing level walking at 1 Hz with maximum and minimum loads of 2450 N and 150 N, respectively. Fetal bovine calf serum diluted to 50% concentration with deionized water was used as lubricant. Weight loss increased linearly during the tests. For 32 mm N2/Vac, Crossfire, and X3 acetabular components the wear rates were respectively 46.4, 3.6 and 1.3 mm3/million cycles [data not shown]. The wear of X3 was 62% lower than that of Crossfire and 97% lower than that of N2/Vac [94].

3.1.2 UHMWPE crosslinking and oxidation

Crosslinking of a polymer consists in the linking of two or more polymeric chains by means of covalent bonds (Figure 26). This results in the formation of a long branched molecule with increasing molecular mass, theoretically up to infinite. This process can be obtained either by chemical or by radiochemical reactions [95].
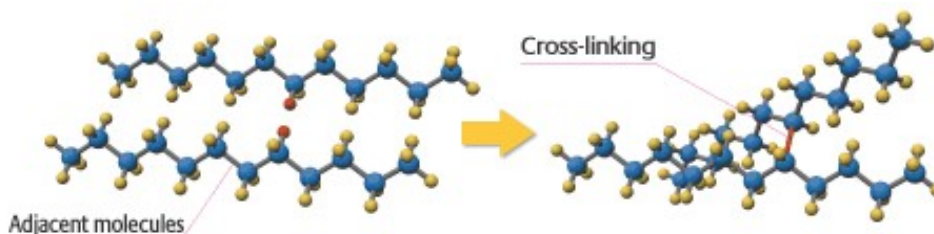
Figure 26: General schematization of the crosslinking process

Chemical crosslinking requests the addition of suitable reactants and additives, mixed with the resin powder during conversion to bulk rod or sheet, to stimulate the

polymerization process [96]. For this reason, chemical crosslinking is generally not used to process UHMWPE for medical applications.

Radiation crosslinking of polyethylene is induced by high energy radiation in an inert atmosphere [97]. Either gamma or electron beam (e-beam) irradiation can be used, but there are few important differences between the two methods, especially in terms of penetration of the radiations and radiation dose achieved. Gamma irradiation sources are usually based on the artificial isotope of cobalt (60Co) that generates gamma photons, while irradiation with electron beam is based on accelerated and charged particles. Commercial e-beam accelerators provide a radiation dose rate that is about two orders of magnitude larger than that of a gamma source. However, either electron beam or gamma rays have a mean energy some orders of magnitude higher than that of chemical bonds.

A complex energy transfer phenomena leads to the homolytic breakage of C-C and C-H bonds, giving H· radicals and primary and secondary macroradicals [98]. These macroradicals are formed throughout the amorphous phases of UHMWPE and likely in the crystalline phase. The radicals formed upon irradiation may then have different reactivity depending not only on their mobility. Since orthopedic UHMWPE has an important molecular mass (2×10^{-6} amu on average) and consequently a high viscosity, even in the molten state, macroradicals have very low mobility. They then undergo a fast recombination, giving back a C-C bond while dissipating energy with no effect on the polymer characteristic. The scission of C-C bonds is a stochastic process so primary macroradicals recombine in all three phases. H· radical instead have a diameter smaller than 1 Å and can diffuse even in the crystalline phase, where distances between C atoms are approximately 4 Å.

Crosslinking occurs primarily in the amorphous and third phases of UHMWPE, while in the crystalline domains the chain segments are not close enough to allow the recombination of the free radicals (lattice spacing are smaller than C-C bond length). Crosslink density increases with the absorbed radiation dose, but the process saturates at around 100 kGy. The effect of this process is a reduced chain mobility and chain stretch, resulting in decreased ductility of the polymer and meaning reduced elongation at break, toughness, and fatigue crack propagation resistance [99]. Conversely, irradiation does not affect strength of the polymer, since it is mainly dependent on its crystallinity [100]. Crosslinking has also a beneficial effect: it decreases the plastic deformation at the surface of the polymeric liner, decreasing the wear rate linearly respect to the radiation dose [89].

Manufacturers of orthopedic implants can choose different optimum radiation doses, between 50 and 100 kGy. In fact, the beneficial effects of crosslinking decrease rapidly above this range. Doses around 50 kGy favor some mechanical properties, such as toughness and elongation at break, while a dose around 100 kGy privileges wear resistance. For this reason the irradiation dose must be balanced, obtaining the desired degree of crosslinking but maintaining mechanical properties and/or oxidation resistance.

Of all degradation mechanisms, oxidation is one of the most important. Autoxidation is defined as auto-initiated oxidation by molecular oxygen, but commonly it describes the reaction of oxygen with organic materials by a free radical process [101]. Oxidation rate of hydrocarbon polymers is initially low, and normally increases due to the increasing concentration of hydroperoxide, then eventually decreases again to a constant level (Figure 27).
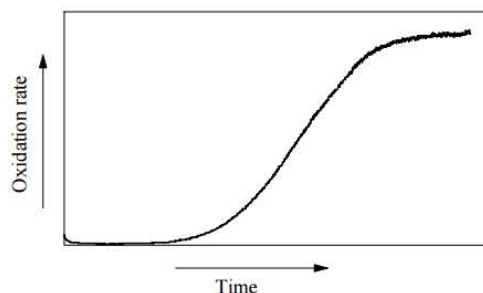
Figure 27: Typical curve of the rate of polypropylene oxidation

The free radical chain cascade reaction can be initiated thermally, photochemically, mechanically or by high-energy radiation. Susceptibility to oxidative degradation is determined by polymer structure (crosslinks, functional groups, unsaturations etc.) and content of chemical impurities.

Bolland et al. developed in the 1940s a scheme for the oxidation of short-chain hydrocarbons, known as Bolland's cycle (Scheme 7) [102].
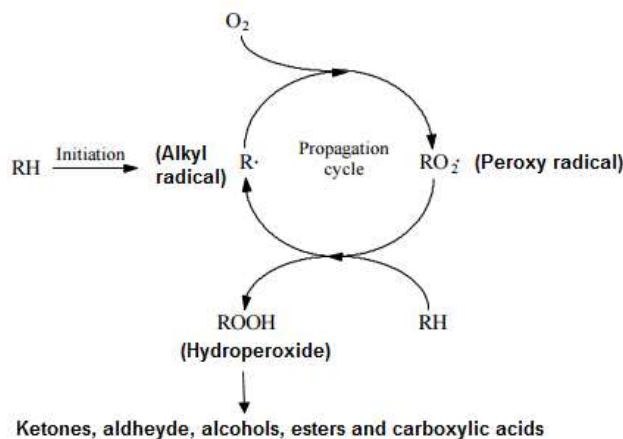
Scheme 1: Bolland's cycle

However, the scheme was derived for liquid solutions with homogeneous kinetics and high mobility of free radicals. On the contrary, the degradation of solid polymers is influenced also by restricted mobility of radicals, morphological variations and enhanced sensitivity of oxidation products on further oxidation.

The oxidation cycle is divided in three different steps: initiation, propagation, and termination. Initiation consists in the formation of macroradicals, because of homologous chemical bonds scission. The breakage of the bonds requires energy (from various sources such as heat, UV light or radiations). The radicals formed can then react either with other radicals or with oxygen, depending on concentration and

availability of the species. The second step, called propagation, proceeds with oxygen consumption by the material. The reaction between alkyl radicals and oxygen is usually very fast, leads to the formation of peroxy radicals, which can extract a H atom from the polymer, yielding a hydroperoxide and a new radical that can begin another propagation cycle. Hydroperoxides decompose to ketones, alcohols, carboxylic acids and esters, in variable amounts and even at room temperature. The main product of this decomposition are usually ketones [103]. Termination, i.e. the last step, consists in the end of the propagation cycle, when two radicals recombine, yielding a non radical product. This reaction occurs more likely between the peroxy radical and an alkyl macroradical, which migrates along the polymeric chain, with formation of peroxides [104].

The sctructure of semi-crystalline polymers hinders the diffusion of molecules and macroradicals. Thus, the availability of oxygen can be higher on the surface than in the bulk of the material, resulting in a oxidation depth profile [105]. Semi-crystalline polymers are inhomogeneous multiple-phases materials, in which the tightly packed lamellae can be more or less impermeable to oxygen, depending on the degree of crystallinity. The oxygen is then concentrated in the interlamellar amorphous regions of the polymer. In general, the oxidation starts in one spot and spreads around by propagation. This leads to the development of localized oxidation zones, called "hot spots" [106].

3.2 Ceramic materials

Ceramic materials are inorganic compounds consisting of metallic and non-metallic elements held together by ionic or covalent bonding [107]. They are produced by fusing or sintering powders, obtaining brittle, polycrystalline solids. The manufacturing process usually includes some steps: isostatic pressing, machining into near final shape, sintering of the powder by firing in a furnace, hot isostatic pressing to reduce porosity, tempering to improve toughness, and final high-precision polishing [108]. The processing of ceramic components must be performed in accordance with international quality standards and stringent FDA regulatory requirements [109].

The powder composition, in particular purity and size of granular particles, defines the strength of the material. Ceramic materials have some outstanding tribological properties, including elevated hardness that contributes to wear resistance and improved wettability, which contributes to lower the friction against UHMWPE under physiological loading [110].

Ceramic materials with biomedical applications have several useful properties such as higher wear resistance than metals, elevated stiffness, higher compressive and bending strength and inert behavior in a biological environment [111]. However, the weak point of ceramic materials is their brittleness, caused by voids, defects or flaws in the structure [107].

Ceramic materials started to be employed in hip arthroplasty in the 1970s, firstly in Europe and Japan [112, 113]. Their development was due to the necessity of reducing wear rates, with the aim of preventing the formation of debris and consequent osteolysis. This led in the 1990s to the development of new Ceramic-On-Ceramic bearing couples [114].

Different types of ceramics are clinically relevant in prosthetic joint replacements. The most praised are well-known alumina, zirconia, zirconia-toughened alumina composites, oxidized zirconium and silicon nitride.

3.2.1 Alumina

Alumina has a successful history in hip replacement designs since the 1970s [113, 115]. It was first introduced to replace CoCr surfaces in hip and knee replacements, thanks to its smoother, lower-friction surface, associated with the lowest bearing wear rates of any other material used in orthopedic surgery. Al_2O_3 bearings are the only with over 30-year of clinical survivorship and have a long-term track record for biostability and biocompatibility [116]. This material has evolved though gradual improvements in manufacturing over the decades and is now a widely recognized, well-validated ceramic biomaterial [117]. Progressive improvements over the years, compared with other ceramic materials properties, are listed in Table 7.

Property	Alumina (1970s)	Alumina (1980s)	Alumina (1990s)	Zirconia	ZTA
Bending strength (MPa)	>450	>500	>550	>900	>1000
Fracture toughness (MPa m$^{1/2}$)	4	4	4	8	5.7
Vickers hardness	1800	1900	2000	1250	1975
Grain size (μm)	4.5	3.2	1.8	<0.5	<1.5
Young's modulus (GPa)	380	380	380	210	350

Table 7: Various Properties of Alumina and Zirconia ceramics used in total hip reconstruction

However some drawbacks such as catastrophic fracture risk, limited design options and squeaking have been documented over the years, therefore it's still needed to develop more advanced ceramic materials for THA.

Al_2O_3 has polycrystalline hexagonal monophasic structure and shows resistance to corrosion, chemical and hydrodynamic stability. Its elevated hardness confers resistance to wear, but on the other side also lower flexural strength and fracture resistance [118]. According to the standard ISO 6474, alumina for biomedical applications must reach 99.5% purity level. Moreover, metal oxide and silica content must be lower than 0.1%, because they promote grain growth, impeding densification.

For this reason a minimal percentage of MgO (<0.5%) is added to inhibit grain growth, allowing to achieve a fully dense sintered body with a fine grain microstructure. The amount of CaO instead must be lower than 0.1%, since it leads to worse static fatigue resistance. Most alumina components are composed of α-Al$_2$O$_3$ grains, fused together by pressing and sintering at elevated temperatures, between 1600 and 1800 °C.

Alumina resistance increases with the reduction of porosity and grain dimension. Grain size bigger than 7 μm can lead to the lowering of mechanical properties by about 20% [119]. Al$_2$O$_3$ outstanding wear properties are due to extremely low surface roughness. Even after prolonged presence in the body, the amount of alumina debris released from the articulating surface is negligible. In contact with body fluids only a very thin (less than 50 Å) hydrated layer of Al(OH)$_3$ forms on the surface of the material, through hydrogen links between the water molecules and the oxygen atoms. This thin layer acts as a lubricating layer between implant components and reduces wear in COP bearings [120]. This property can be assessed measuring the surface wettability, by means of contact angle. The contact angle of alumina is 44°, whereas for example on polyethylene is 80° [121].

Physical and typical properties of alumina implants are summarized in Table 8, along with the International Standards Organization (ISO) requirements.

| Property	Commercially available Alumina	ISO Standard 6474
Alumina content (weight %)	>99.7	≥99.51
SiO$_2$+Na$_2$O (%)	<0.02	<0.1
Density (g/cm^3)	3.98	≥
Average grain size (μm)	3.6	<7
Hardness (Vickers)	2400	>2000
Bending strength (MPa)	595	>400
Surface finish Ra (μm)	0.02	
Compressive strength (MPa)	4000-4500	
Young's modulus (GPa)	380-420	
Fracture toughness (MN/m$^{3/2}$)	4-6	
Implant strength (N/cm^2)	40-50	

Table 8: Physical and typical properties of commercially available Alumina

A new improved pure alumina ceramic, BIOLOX®Forte (CeramTec AG, Plochingen, Germany) was introduced to the market in 1995 (Figure 28).
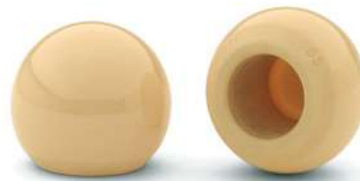
Figure 28: BIOLOX®Forte (CeramTec AG, Plochingen, Germany) femoral head

BIOLOX®Forte is a high purity alumina (>99.7%), with an addition of magnesium oxide (MgO) to prevent the discontinuous growth of alumina grains, leading to a more homogeneous and dense material with enhanced mechanical resistance. The grain size is 1.8 μm on average (Figure 29), as specified by the manufacturer. It has lower porosity and higher density (3.98 Mg/m^3) than previous materials, with typical density 3.95 Mg/m^3.
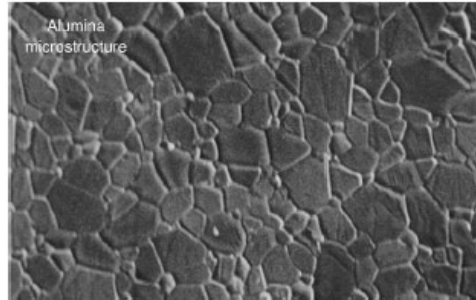

Figure 29: Micrograph of sintered Al_2O_3 microstructure with average grain size of 2 μm or less

BIOLOX Forte® follows the highest standards for biocompatibility, durability and stability. It also exhibits highest quality in surface roughness and roundness. Moreover, it is wear resistant and can articulate in either UHMWPE cups or ceramic inlays.

3.2.2 Zirconia

Ceramics based on zirconium oxide were introduced as an alternative to aluminum oxide ceramic. This material is considered to be less brittle and less prone to fracture. It showed to have a lower wear rate against UHMWPE respect to metallic femoral heads, such as stainless steel or CoCr [122]. Zirconia gained clinical application only recently because the one synthesized in the 1980s showed abnormal radioactivity [123] and tended to be unstable in vivo. Modern technology allowed obtaining a new, improved, non-radioactive and stable zirconia, starting from pure zirconium and adding chemical stabilizers.

Pure zirconia exists in three different crystallographic phases (Figure 30): cubic, tetragonal, and monoclinic. Transformation from one to another depends on various conditions such as temperature, mechanical stress and humidity.
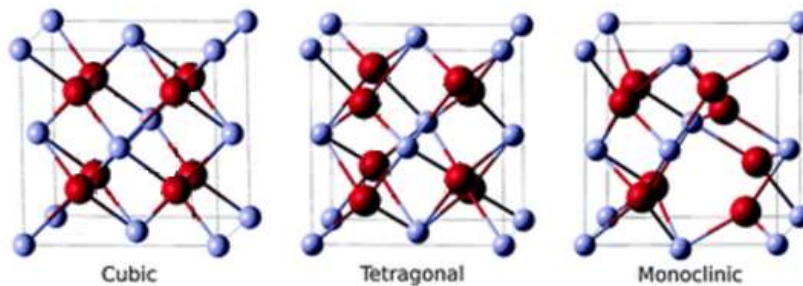
Figure 30: Cubic, tetragonal and monoclinic ZrO_2 lattice structures. Large dark red spheres and small light grey spheres represent O and Zr atoms, respectively

Crystallographic instability has been the main reason for not using zirconia for the bearing component of joint prosthesis. In fact, the transformation from the metastable tetragonal phase to the more thermodynamically stable monoclinic phase results in a volume increase of approximately 3-4% [124]. This volumetric swelling presents both advantages and disadvantages: it generates a compressive stress field at the tip of a propagating crack, resulting in crack growth resistance but can also have disastrous consequences if not properly controlled. New sintering methods, developed in the 1990s, permitted to obtain crystallographically stable zirconia by adding chemical stabilizers, for example: Y_2O_3, CeO_2 and Al_2O_3. These materials are known as partially stabilized zirconia (PSZ). [125].

PSZ materials have significantly higher compressive strength, bending strength, impact strength and fracture toughness, but have a lower elastic modulus than alumina ceramic. Among them, yttrium oxide PSZ (Y-PSZ) has the highest bending strength and fracture toughness followed by cerium oxide PSZ (Ce-PSZ) [126]. PSZ is mechanically stronger than alumina, while alumina is chemically more stable than PSZ in vivo. The advantage of zirconia over alumina in orthopedic applications is its lower stiffness, smaller average grain size and higher density [118]. The most common type of zirconia with biomedical applications is the Y-TZP, i.e. yttria stabilized-tetragonal phase, polycrystalline zirconia. Its chemical composition is about 93–94% zirconia (ZrO_2) and 5% yttria (Y_2O_3) [124].

To overcome concerns related to the brittleness of ceramic materials, surface modifications have been used to produce zirconia femoral heads [127]. Oxidized zirconium is a proprietary implant material, marketed under the trade name Oxinium (Smith and Nephew Orthopedics, Memphis, Tennessee, US) (Figure 31) [128].

Figure 31: Oxinium femoral head (Smith & Nephew Orthopedics)

Oxinium is a ceramic-metal composite with a surface layer of zirconia. The ceramic surface layer is highly adherent without pores or voids, which might be detrimental to oxide adhesion. Studies have demonstrated the superior wear performance of this material against UHMWPE, in comparison with CoCr metal alloy [129]. The material is fabricated by heating the zirconium alloy in the presence of air. This step converts the surface to a black zirconium oxide ceramic (~5 μm thick). Phase transformation from metastable tetragonal to stable monoclinic does not represent a problem with oxidized zirconium because it contains over 95% of stable monoclinic zirconia. It was first used for knee replacement in 1997 and then for hip replacement in 2002. The main issue is that Oxinium is only suitable for hard- on-soft bearings. Currently it cannot be used in hard-on-hard bearings [130]. Some outstanding properties include increased wettability, increased scratch resistance and lower wear rate against UHMWPE compared to CoCr femoral heads [131].

3.2.3 Alumina-Zirconia composites

Despite encouraging performances, Al_2O_3 and ZrO_2 ceramics have shown some drawbacks. Al_2O_3, even if widely used, showed some cases of catastrophic failure due to its extreme brittleness [132]. The mechanical properties of alumina can even restrict design options, limiting surgical flexibility to substitute precisely the joint [133]. On the other side, Yttria-stabilized ZrO_2 (YSZ) is unstable and could undergo phase transformation in vivo, with unpredictable, possible catastrophic outcomes [134].

Mixed composites of ZrO_2 and Al_2O_3 for hip replacement have been marketed and used in hip replacements starting from the 2000s. Two types of composite materials can be prepared: a stabilized zirconia matrix reinforced with alumina particles, called alumina toughened zirconia (ATZ) and an alumina matrix reinforced with zirconia particles, known as zirconia toughened alumina (ZTA). Both materials have proven to be biocompatible [135]. Moreover, both are provided with higher toughness values respect to monophasic ceramics [136].

ATZ materials, with a zirconia matrix, still show the issue related to hydrothermal instability. Consequently, they still need yttria to stabilise zirconia [137], while this addition can be avoided in ZTA materials, since alumina constrains the zirconia particles, keeping them in a metastable state [138]. Furthermore, the hardness is higher in composites with an alumina matrix, because it is harder than zirconia [139].

By now, zirconia-toughened alumina (ZTA) has shown encouraging success [140] although the long-term in vivo outcomes are yet unknown [141]. The advantages of ZTA relate to a higher toughness and fracture strength than previous alumina generations, even if they essentially share equivalent wear rates. ZTA derives its strength and toughness from the same mechanisms of ZrO_2 ceramic components [142]. The thermodynamically unstable tetragonal zirconia phase transforms to its more stable monoclinic form. The consequent volume expansion that arrests the advancing crack. Thus, both YSZ and ZTA owe their toughness to a phase instability of the material itself, rather than to its precise engineering [143]. Moreover, it is well known that warm temperatures and moist environments, conditions similar to the ones found in the human body, exacerbate this phase instability. An important drawback resides in the fact that ZTA is still an unstable ZrO_2 based material: its degradation may be delayed respect to ZrO_2 ceramic bearings, but it may manifest nonetheless [144].

Starting in 2000, a new composite material has been introduced on the market as a femoral head material. BIOLOX®Delta (CeramTec, Plochingen, Germany) (Figure 32) is a zirconia toughened alumina ceramic (ZTA) for biomedical applications.

Figure 32: BIOLOX ®Delta (CeramTec AG, Plochingen, Germany) femoral head

BIOLOX®Delta is composed of an alumina matrix (82% by volume) reinforced by zirconia (17 w/w%), strontium aluminate (0.5 w/w%), and chromium oxide (0.5 w/w%) [118]. BIOLOX®Delta shows stiffness and hardness in the same range of alumina, whereas flexural strength almost doubles. The additives are useful to provide crack tip blunting and toughening mechanisms, as well as to increase the hardness. Yttria- stabilized zirconia preserves the material resistance, while CrO keeps hardness at high levels. $\underline{SrAl_2O_4}$ allows the nucleation of larger acicular Y-TZP grains, which offer a wider surface on which the crack can dissipate its energy (Figure 33).
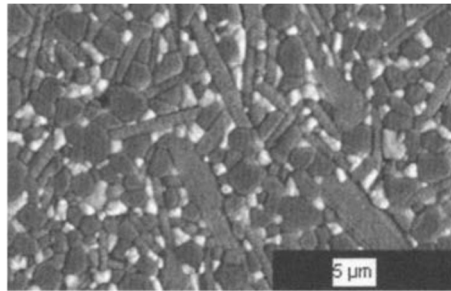
Figure 33: Micrograph of BIOLOX®Delta microstructure showing acicular Y-TZP grains

In case of a crack, the phase transformation at an individual zirconia grain acts as an obstacle to further crack propagation [145]. To gain full advantage of the toughening system, the monoclinic phase content is kept as low as possible. During production, especially after hard-machining, the monoclinic phase may increase and needs to be reversed by a heat treatment and polishing step, to transforms zirconia back to the tetragonal phase.

This ceramic bearing is now widely spread across the orthopedic industry in both femoral heads and acetabular liners.


3.2.4 Silicon nitride

Silicon nitride (Si_3N_4) is a non-oxide ceramic rarely observed in nature [146]. Synthetic Si_3N_4 was first developed in 1859, but commercial interest in the material increased only in the 1950s. In the 1980s was recognized its potential as a structural ceramic. In this decade, significant improvements were made in its synthesis, processing and properties. Currently silicon nitride finds industrial applications thanks to its high strength and fracture resistance under extreme operating conditions. Recently it has been used also in the orthopaedic field, to promote bone fusion in spinal surgery and to develop bearings with improved wear rates and longevity [147, 148].

During the last decades, mechanical properties of Si_3N_4 have been improved by refining processing methods and introducing additives. Three typical strategies are used to process the material: reaction bonding, sintering and pressure-assisted sintering. Reaction-bonded processing consists in the nitridation of a porous-shaped component, formed from silicon (Si) powder, which is heated in N_2 at elevated temperatures (1200–1400 °C). The resulting material has relatively low density, high

34

porosity (typically 15–20%) and low strength (i.e. flexural strength of 200–300 MPa). In sintering, Si_3N_4 powders are mixed with additives (for example Y_2O_3 and Al_2O_3) and then heated in an N_2 atmosphere (P=10–20 MPa) at temperatures >1700 °C. The additives aid the densification process. Hot pressing and hot isostatic pressing (HIP) are the common methods of pressure-assisted sintering: the powder, containing additives, is placed in a graphite die (hot pressing) or encapsulated in a metal can and subjected to high applied pressure (50 MPa in hot pressing; 150–200 MPa in HIP) at high temperatures (>1700 °C). Si_3N_4 processed with this method gains improvements in strength, but the manufacturing cost rises [149]. Improvements in processing and manufacturing made it possible to obtain Si_3N_4 ceramics with higher mechanical reliability. Si_3N_4 fabricated by hot pressing or hot isostatic pressing has a higher strength than Al_2O_3, even if they have comparable hardness.

Si_3N_4 can be improved also by an ''in situ toughening'' process. The ceramic material is thermally treated at high temperatures (>1700 °C) to grow the grains into an elongated, rod-like morphology (Figure 34). In this way, rod-like grains hinder the propagation of a crack. Pullout of the elongated grains behind the tip or deflection of the crack along the grain boundaries provide energy-dissipating mechanisms that reduce the tendency for fast crack growth.
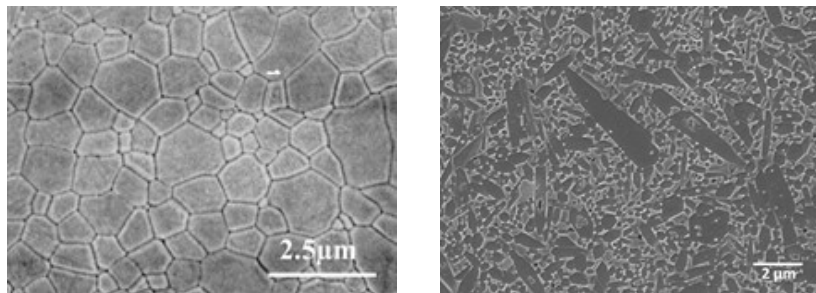
Figure 34: SEM images showing typical microstructures of ceramic bearing materials: dense, fine-grained Al_2O_3 (left) in situ toughened Si_3N_4 (right)

In situ toughened Si_3N_4 with elongated grains (>1 μm diameter) were shown to have fracture toughness values approaching 10 MPa $m^{1/2}$, compared with values of ≈3 MPa $m^{1/2}$ for the same material with less elongated, sub-micrometer diameter grains [150]. This mechanism is limited or absent in conventional Si_3N_4 [151].

Ceramic materials used in orthopaedic surgery underwent extensive studies and review for several decades, with the goal of assessing their advantages and disadvantages respect to each other and respect to metallic alloys [152, 153]. Si_3N_4 ceramics show some differences from other common ceramics presently used in orthopaedic surgery. Alumina and zirconia can be used presently in the bearings of total hip and total knee replacements only in their polished form, while Si_3N_4 can be formulated into both a porous substrate and a hard polished bearing surface. In porous form, it can support bone ingrowth for the fixation of the implant. In the polished form, it constitutes a smooth articulating surface in replacement implants. In theory, being a non-oxide ceramic, it should not be suitable for hip and knee bearings, but it was demonstrated that surface oxidation can be controlled or

eliminated by doping the material with selected additives, increasing its resistance to oxidation [154].

Hip and knee replacement bearings require biomaterials with low wear rates and frictional coefficients, which can remain stable in vivo for several decades. Si_3N_4 can articulate against itself, metal or PE with very low friction, since it can be polished to a very high quality surface finish (Ra 5 typically 0.01–0.05 μm) [155]. In particular, it shows very favourable tribological properties when articulating against itself in water. This is because a slightly thin oxide layer of SiO_2 forms on Si_3N_4 surface, with a thickness of 2-5 nm on average. According to Xu et al. [156] this reaction (I) has an activation energy of 13.6 KJ/mol, which is much smaller than that of static oxidation corresponding to about 84-108 KJ/mol, because it is triggered by friction. This phenomenon is common also in most metallic and other non-oxide materials. When this layer is removed through tribo-chemical wear (II), the surface immediately repairs itself because of re-oxidation [157].

$$Si_3N_4 + 6H_2O \rightarrow 3SiO_2 + 4NH_3 \qquad (I)$$
$$SiO_2 + H_2O \rightarrow Si(OH)_4 \qquad (II)$$
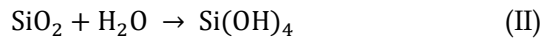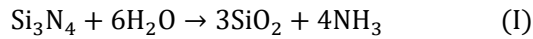
The hydrated silicon oxide represents a lubricating film between the articulating surfaces. This lubricating layer is effective in protecting the prosthetic components and results in low wear rates. When tested in a hip simulator, Si_3N_4 femoral heads produced against Si_3N_4 acetabular liners wear rates that were comparable with Al_2O_3–Al_2O_3 wear rates, which are the lowest of any orthopaedic bearing [158]. The in vivo environment should be even more favorable, since human synovial fluid is an excellent lubricant.

Oxide ceramics, for example Al_2O_3 and stabilized ZrO_2, were commonly used in orthopaedic applications because of their excellent biocompatibility. Recent cytotoxicity assays showed that Si_3N_4 ceramics have similar, favourable biocompatibility properties [159]. Si_3N_4 may even encourage cell adhesion, proliferation and differentiation. Thanks to this property, it could support bone cell growth and metabolism.

Recently, Amedica (Salt Lake City, Utah, USA) commercialized a Si_3N_4 ceramic for hip bearing applications (Figure 35). The material consists of 90% Si_3N_4 powder (with a mean particle size of 0.5 μm), 6 wt% yttrium oxide (Y_2O_3) and 4 wt% alumina (Al_2O_3). Wear testing of COM and COC bearings in a hip simulator demonstrated ultralow wear rates, comparable to or lower than alumina-alumina.

Figure 35: Representative hip and other reconstructive implants produced from biomedical Si_3N_4 (Amedica, Salt Lake City, Utah, USA)

Chapter 4
Experimental procedures

4.1 Preparation of specimens

Four different ceramic materials were tested: BIOLOX®Forte *(CeramTec AG, Plochingen, Germany)*, BIOLOX®Delta *(CeramTec AG, Plochingen, Germany)*, Oxinium (*Smith and Nephew Orthopedics, Memphis, Tennessee, US*) and Silicon Nitride (*Amedica, Salt Lake City, Utah, USA)*. For each ceramic material, two femoral heads as received by the manufacturers were cut to obtain a set of 6 spherical caps (i.e., 3 from each ball).

The new generation of highly crosslinked polyethylene Stryker X3™ (*Stryker Orthopedics Inc., Mahwah, New Jersey, USA*) was selected as a reference sample to study the influence of each ceramic material on the oxidative degradation of polyethylene after accelerated aging. Six as received acetabular liners were sectioned through their thickness (Figure 36) to obtained 5 pieces from each liner, 30 pieces in total. The polyethylene specimens were cut with identical size and shape, maintaining the original concave surface of the liner on one side. The concave side was then coupled to the convex surface of the spherical cap obtained from the ceramic femoral heads.
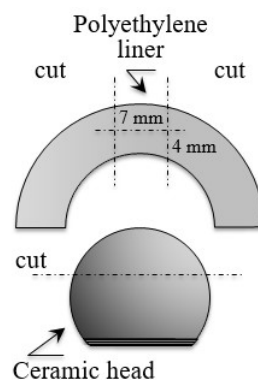

Figure 36: Schematic draft of the sample preparation procedure

4.2   Accelerated aging protocol

Oxidation of UHMWPE takes long time (months to years) to reach appreciable levels at ambient or body temperature. Hence, thermal aging techniques have been developed to accelerate the oxidation of UHMWPE, with the expectation that the mechanical behavior after accelerated aging will be comparable to naturally aged material [160]. Generally, the aim of these accelerated aging protocols is to evaluate the oxidation resistance of UHMWPE materials [161, 162] and also to precondition components that subsequently will be tested to assess wear rates [163, 164, 165].

It is well known that aging at elevated temperatures will accelerate the oxidation of UHMWPE [166]. For this reason a number of different protocols has been developed

over the years, based on either elevated temperature alone, or elevated temperature combined with elevated pressure in oxygen.

The current standard artificial aging protocols are based mainly on the techniques proposed by Sun et al. [167] and Sanford et al. [168]. Following the technique proposed by Sun et al., specimens are thermally aged in a standard air furnace for up to 23 days at 80°C pressurized to 1 atmosphere. Conversely, following the technique proposed by Sanford et al., specimens are aged under 5 atmospheres of pure oxygen at 60° and 70°C for up to 14 days. The American Society for Testing and Materials has recently standardized both methods. An ASTM standard for accelerated aging of UHMWPE has recently been published (ASTM F2003-00). It includes both method A (21 days at 80°C in air) and method B (14 days at 70°C in 5 bar oxygen). However, these protocols have not been completely successful in reproducing the complex process of natural aging both during real-time shelf aging and implantation. For example, they fail in simulating the inhomogeneous variations of physical and mechanical properties through the thickness of the material [169, 170]. Moreover, they show poor interlaboratory reproducibility (especially for method B) [171].

In this case, an alternative protocol for accelerated aging of UHMWPE has been tuned. This method aims to reproduce partially the conditions found in the human body, especially the moist environment.

All the polyethylene samples were gamma irradiated with an average dose of 32 kGy before aging test, with the aim of increasing the free radical concentration in the polymer, namely the reactivity of the surface exposed to the oxygen dissolved in water. The polyethylene samples were then tested in static contact with each ceramic spherical cap. In addition, other six polyethylene samples were tested in contact with the convex surface of six spherical sections obtained from the outer part of new Stryker X3™ cups, which were not irradiated before aging. The surfaces were dipped in pure water before being coupled to the respective counter surface and immediately placed into the autoclave (Figure 37) at temperatures between 90°C (363K) and 120°C (393K), under water-vapor pressure ranging from ambient pressure to 0.1 MPa for 24h. Commercially available metal clamps (Figure 38) were used to assure a constant pressure between the two components during accelerated aging in autoclave.
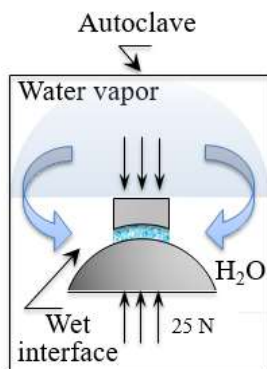
Figure 37: Schematic arrangement of the specimens inside the autoclave
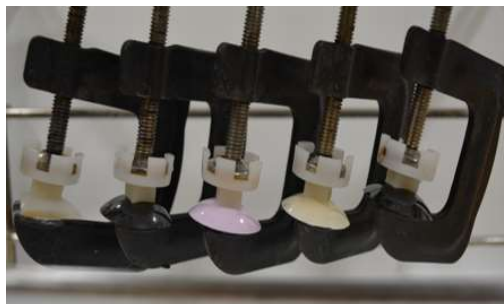
Figure 38: Coupling of the surfaces using commercially available metal clamps

Following these procedures, the presence of water interlayer between the concave and convex surfaces was preserved throughout the entire experiment. After the completion of the accelerated aging procedure, the samples were dried and cooled down with a rate of 100°/h. The test was repeated three times, using two couples for each type of material in each experimental session.

4.3   Raman spectroscopic analysis

Raman spectra were collected using a triple-monochromator (T-64000, Jovin-Ivon/Horiba Group, Kyoto, Japan) equipped with a charge-coupled detector (i.e. a high resolution CCD camera). The laser excitation source was a monochromatic blue line, emitted by an Ar-ion laser at a wavelength of 488nm. The laser power on the UHMWPE surface was typically about 100 mV at the laser head.

A confocal pinhole with an aperture-diameter of 100 μm, placed in the optical path and acting as a spatial filter, enabled to exclude photons scattered from regions outside the focal plane of the probe. Thus, only the signals from a limited in-depth region close to the selected abscissa of the focal plane were brought to the detector. The resulting in-depth spatial resolution was of about 6 μm [172]. The experiments were conducted with a confocal configuration of the probe, corresponding to a x100 objective lens. Numerical objective aperture and confocal pinhole diameter were fixed as: NA=0.9 and Φ=100 μm respectively.

Square maps of Raman spectra were collected on the surface of the samples, with the aid of an automated sample stage. The size of the maps was 50×50 μm and the Raman spectra constituting the maps were collected with a step of 5 μm. For each polyethylene sample three maps were collected over three separated locations, both before and after accelerated aging test. The spectral integration time was typically 20 seconds, and the recorded spectra (collected in the range between 1250 and 1550 cm^{-1}) were averaged over two successive measurements at each selected location. All Raman spectra were collected at room temperature. Given the curved nature of the investigated surfaces, the focus was manually maintained to sharpen the optical probe. Spectral deconvolution has been performed by means of an automatic fitting algorithm enclosed in a commercially available computational package (Labspec 3, Horiba/Jobin-Yvon, Kyoto, Japan), using mixed Gaussian/Lorentzian curves.

4.4   XPS surface analysis

The surface of the samples was also studied by means of X-ray photoemission spectroscopy, using a JPS-9010 MC photoelectron spectrometer (JEOL Ltd., Tokyo, Japan) with an X-ray source of monochromatic MgK_α (output 10 kV, 10 mA). The surface of the samples was cleaned up by Ar^+ sputtering in the pre-chamber. The measurements were then conducted in the vacuum chamber at around 2×10^{-7} Pa, setting the analyzer pass energy to 10 eV and the voltage step size to 0.1 eV. The X-ray

angle of incidence and the take-off angle were 34° and 90°, respectively. For each type of coupling, one polyethylene component was analyzed on the center of the oxidized concave surface.

In addition, the same analysis was carried on two Si_3N_4 unaged samples and two Si_3N_4 samples tested in autoclave, to measure any possible increase of oxygen on the surface that occurred during accelerated aging in humid condition.
The atomic sensitivity factors used for the calculation of Carbon, Oxygen, Silicon and Nitrogen atom % were 4.079, 10.958, 2.387 and 7.039, respectively.

4.5   Cathodoluminescence analysis

Cathodoluminescence (CL) spectra were collected in a field-emission gun scanning electron microscope (FEG-SEM, SE-4300, Hitachi Co., Tokyo, Japan) equipped with a CL device. Electron irradiation was made with an acceleration voltage of 5 kV. Preliminary calibrations proved that the acceleration voltage was below the threshold for perturbation of the stoichiometric structure of the material upon electron beam impingement. The CL device consisted of an ellipsoidal mirror and a bundle of optical fibers, which enabled to collect and to transmit the CL emission into a highly spectrally resolved monochromator (Triax 320, Jobin-Yvon/Horiba Group, Tokyo, Japan). A 150 g/mm grating was used throughout the experiments. A liquid nitrogen-cooled 1024x256 pixels CCD camera was used to analyze the CL emission of the material.

Spectral lines were analyzed with the aid of a commercially available software package (LabSpec 4.02, Horiba/Jobin-Yvon, Kyoto e Japan). Spatially resolved maps of electro-stimulated luminescence were collected on about 10 areas with focusing the electron beam on the sample surface. A lateral step of 50 nm was adopted, which led to the automatic collection of 1600 measurement points per each map. Spectral fitting was conducted by following a deconvolution procedure with Gaussian-Lorentzian spectral modes after subtracting a linear baseline. The CL probe size was preliminarily calibrated and found in the order of 68 and 280 nm in depth and in plane, respectively. All mathematical procedures followed for modeling the CL intensity emission were carried out with the aid of commercially available computational software (Mathematica 5.2; Wolfram Research Inc., Champaign e IL).

Chapter 5
Results

5.1 Raman spectroscopic analysis

The relationship between the observed Raman bands and the vibrational modes of polyethylene has been amply documented in the literature [59, 173, 174, 175].

Raman spectra of polyethylene (Figure 39) can be divided in three sub-region of interest:

- from 1000 to 1150 cm−1 dominated by the C-C stretching vibration mode;
- around 1300 cm−1 mainly represented by the -CH₂- twisting vibration;
- between 1350 and 1500 cm−1 characteristic of -CH₂- bond wagging.

The peak at 1414 cm−1 is characteristic of an orthorhombic crystalline phase, while the intensity of the peak located at 1293 cm−1 can be used to approximate the overall degree of crystallinity of the UWMWPE structure.
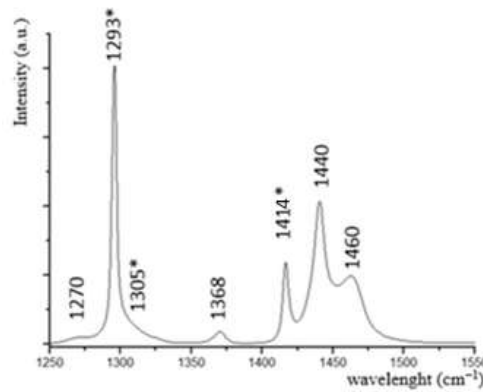
Figure 39: Typical Raman spectra of polyethylene

These features of the Raman spectrum make it possible to quantify the volume fraction of crystalline (a_c), amorphous (a_a) and third (α_b) phases. The volume fraction variations of the three phases were calculated from the relative intensities of selected Raman bands of UHMWPE, according to the method introduced by Strobl and Hagerdon [59]. The method is based on a set of equations that includes the intensities of vibrational bands located at 1293, 1305 and 1414 cm-1, as obtained from unpolarized Raman spectra, as follows:

$$\alpha_c = \frac{I_{1414}}{0.46(I_{1293} + I_{1305})} \qquad \text{(III)}$$

$$\alpha_a = \frac{I_{1305}}{I_{1293} + I_{1305}} \qquad \text{(IV)}$$

$$\alpha_b = 1 - \alpha_c - \alpha_a \qquad \text{(V)}$$

where *I* is the integral intensity, after spectral deconvolution, of each individual Raman

band identified by the subscript. Thanks to the equations (III)~(V), the Raman spectroscopic method can be used to characterize the partially crystalline structure of polyethylene.

In this study, selected xyz locations of the samples were probed nondestructively by means of Raman spectroscopy: 2-D data maps were collected by scanning the samples parallel to the surface of the sample, both before and after accelerated aging. After accelerated aging, the laser focus was repositioned in the same xyz locations selected before thanks to the sub-micrometric step precision of the automated xy.

Figure 40 shows the maps of crystalline volume fractions collected before (A through E) and after (F through J) the accelerated aging process. Each of the 5 couplings was tested. The shown maps are typical of a series of 10 similar maps recorded on each investigated couple and represent local crystallinity values averaged within a Raman probe whose dimensions were ~1 and 6 μm in width and depth, respectively. Increased crystallinity values were generally observed after exposure in autoclave environment, especially for the UHMWPE samples aged in contact with oxide ceramics. Typically, the crystallinity maps exhibited maxima as high as 75% and located at hot spots few micrometers in dimension. Despite the similar values found for the maximum crystallinity at the hot spots, clear differences could be found among different tested samples. The crystallinity values were detectably lower for UHMWPE vs. Si_3N_4 and the control UHMWPE vs. UHMWPE couples, while no significant differences in the recorded patterns could be noticed among samples in contact with oxide heads with a more clearly enhanced crystallinity.

In Figure 41 are shown the maps of crystallinity increases, $\Delta\alpha_c$, for the all series of tested couples (A trough E) including the UHMWPE vs. UHMWPE control couple. These maps were obtained by subtracting the crystallinity values collected before accelerated aging from those recorded at exactly the same locations after 24 h autoclave exposure in contact with the concave counterparts. The histograms (F trough J) are representative of the statistical distribution of $\Delta\alpha_c$ through the collected maps. As seen in these figures, the statistical distribution of $\Delta\alpha_c$ tended to be shifted toward higher values and to be broadened in all the UHMWPE vs. oxide couples. On the other hand, for both UHMWPE vs. Si_3N_4, and UHMWPE vs. UHMWPE the frequency distributions were similarly sharp and the increases in crystallinity was similarly low.

Figure 42 shows the average value of $\Delta\alpha_c$, being 9.37, 9.43, and 10.52% for the oxide couples UHMWPE vs. ZTA, UHMWPE vs. Al_2O_3, and UHMWPE vs. m-ZrO_2, respectively, and 5.08 and 6.42% for UHMWPE vs. UHMWPE and UHMWPE vs. Si_3N_4, respectively. Statistical analyses were performed according to the unpaired Student's t-test. A p value <0.05 was considered statistically significant. The only statistically significant variance was found between UHMWPE vs. oxides and UHMWPE vs. Si_3N_4 couples (p=0.003), while UHMWPE vs. UHMWPE and UHMWPE vs. Si_3N_4 couples showed a statistically insignificant variance. The differences among the three different UHMWPE vs. oxide couples were also statistically insignificant.
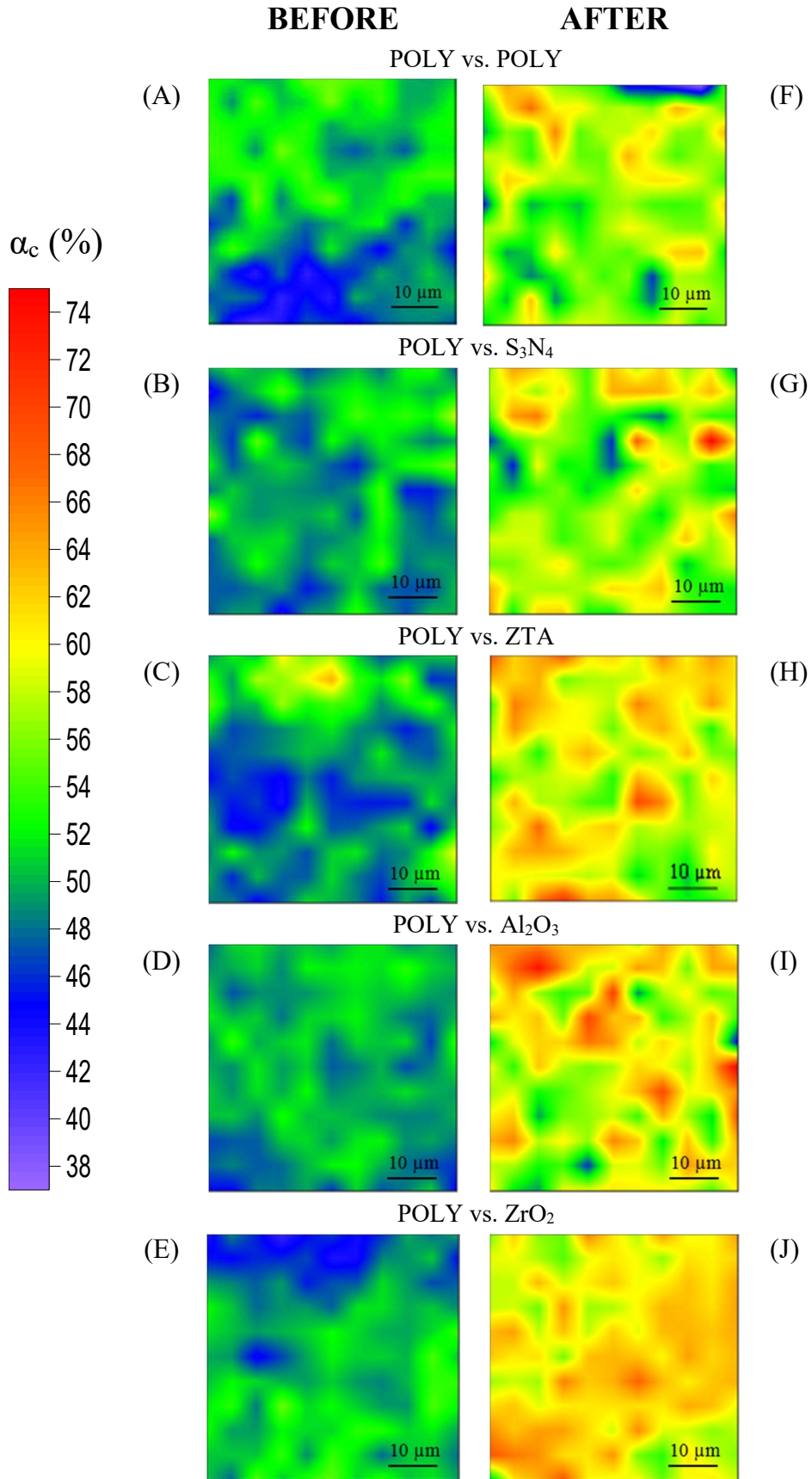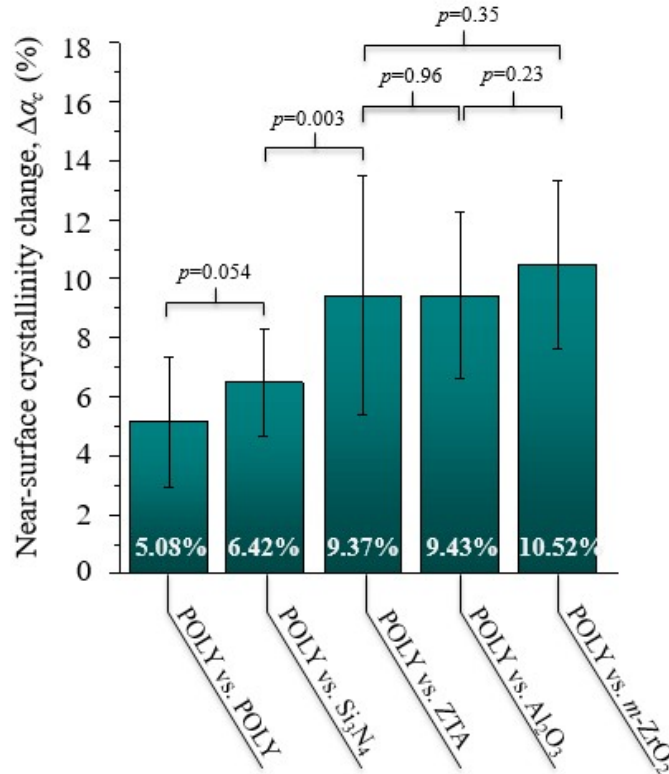
Figure 40: Maps of crystalline volume fractions collected before (A through E) and after (F through J) the accelerated aging process
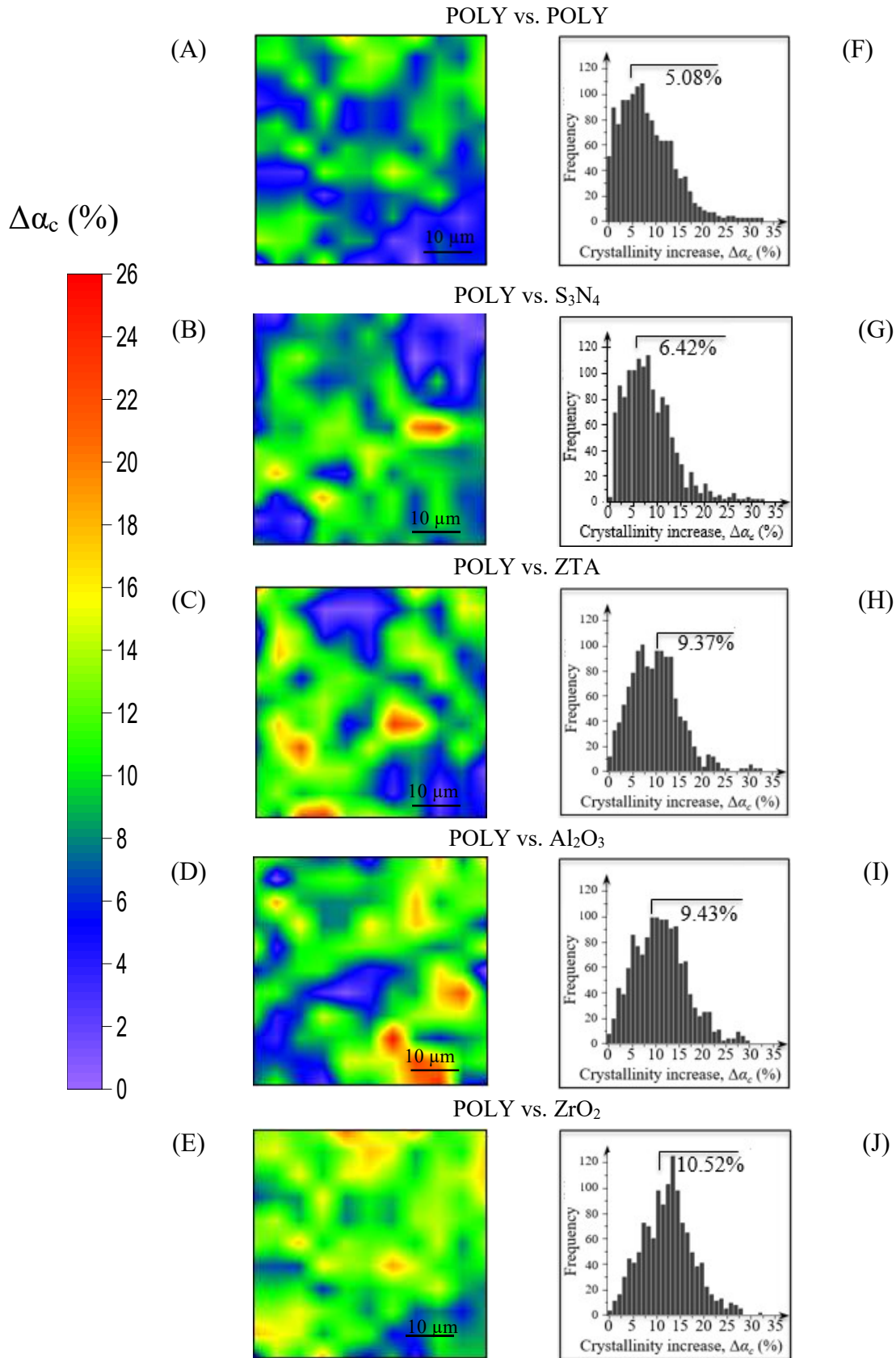
Figure 41: Maps of crystallinity increases, $\Delta\alpha_c$, for the all series of tested couples (A trough E) and histograms (F trough J) representative of the statistical distribution of $\Delta\alpha_c$

Figure 42: Δα_c trends for each different tested couple, including standard deviations and the results of the respective analyses of variance

The variation of crystalline phase fraction, triggered by the oxidative degradation, was then converted in oxidation index (*OI*) using a phenomenological equation [176].

The oxidation index is usually measured by Fourier transformed infrared (FTIR). However, the correlation between crystallinity and *OI* can be obtained by fitting the experimental data with an exponential function (VI) that represents the phenomenological relationship between the two parameters, as follows:

$$OI = \exp\left\{a \cdot \tan\left[b(\Delta\alpha_{(c-c_0)} - c)\right] + d\right\} \tag{VI}$$

where α_{c_0} is the crystalline fraction of X3™ UHMWPE as received.

The best fitting was obtained with a, b, c, and d equal to 0.22, 4.04, -0.40 and -0.04, respectively.

Figure 43 shows the maps of calculated *OI* values, before (A through E) and after (F through J) the accelerated aging process. As is seen, *OI* values increase after 24 h autoclave exposure in contact with the concave counterparts. Particularly, *OI* values were lower for UHMWPE vs. Si_3N_4 and the control UHMWPE vs. UHMWPE couples, while samples in contact with oxide heads show enhanced *OI* values, with no significant differences in the recorded patterns.
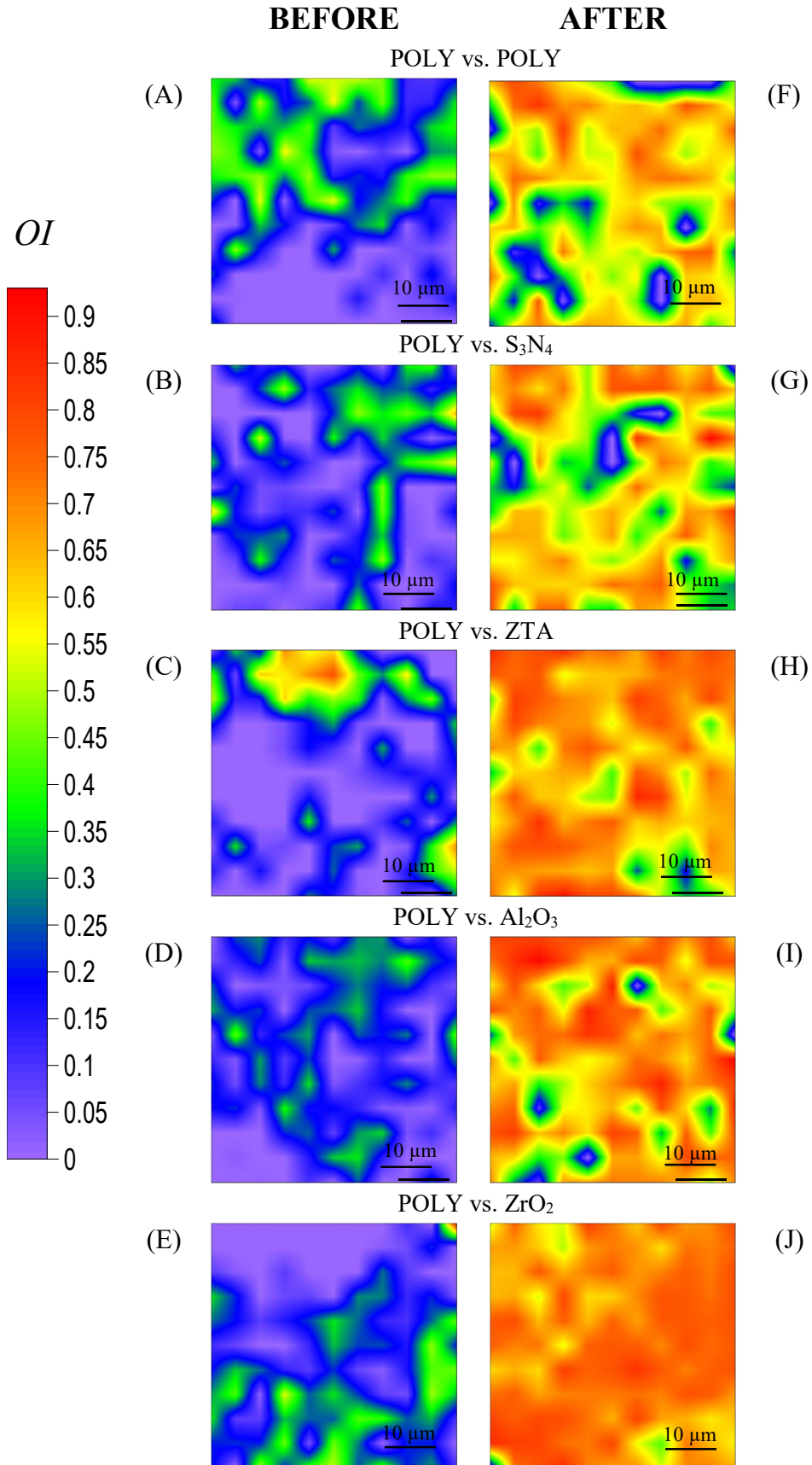
Figure 43: Maps of calculated OI values, before (A through E) and after (F through J) the accelerated aging process

Figure 44 shows the difference in oxidation index, ΔOI, as obtained from the $\Delta\alpha_c$ values in Figure 42. Again, the ΔOI values measured after 24 h autoclave exposure were clearly higher in UHMWPE samples coupled with oxide ceramics as compared to the couple including the non-oxide Si_3N_4 head and the control UHMWPE vs. UHMWPE couple, which showed similar behavior.
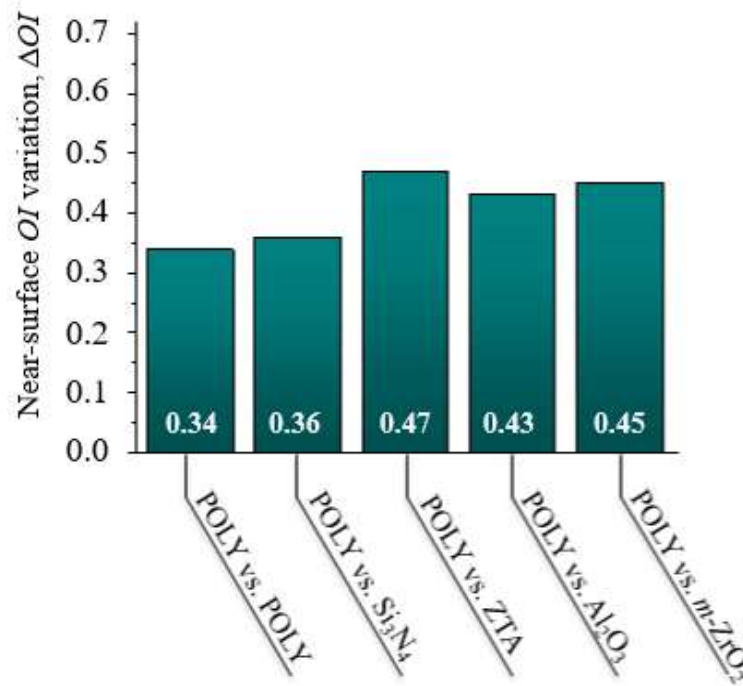
Figure 44: ΔOI trends for each different tested couple

Figure 45 shows the maps of the variations of crystallinity, $\Delta\alpha_c$, (A through E) compared to the corresponding maps of variation of oxidation index, ΔOI, (F through J). The comparison between these maps shows that the variation in oxidation index is commonly related to a variation in crystallinity.

The comparison for each material between the fractional variations at exactly the same locations of the crystalline, third (semi-crystalline) and amorphous phases, respectively, is shown in Figure 46. Such microscopic analysis revealed that the major fraction of newly formed crystalline phase developed at the expenses of the third phase, while only a minor variation could be found in the local pattern of amorphous phase fraction.
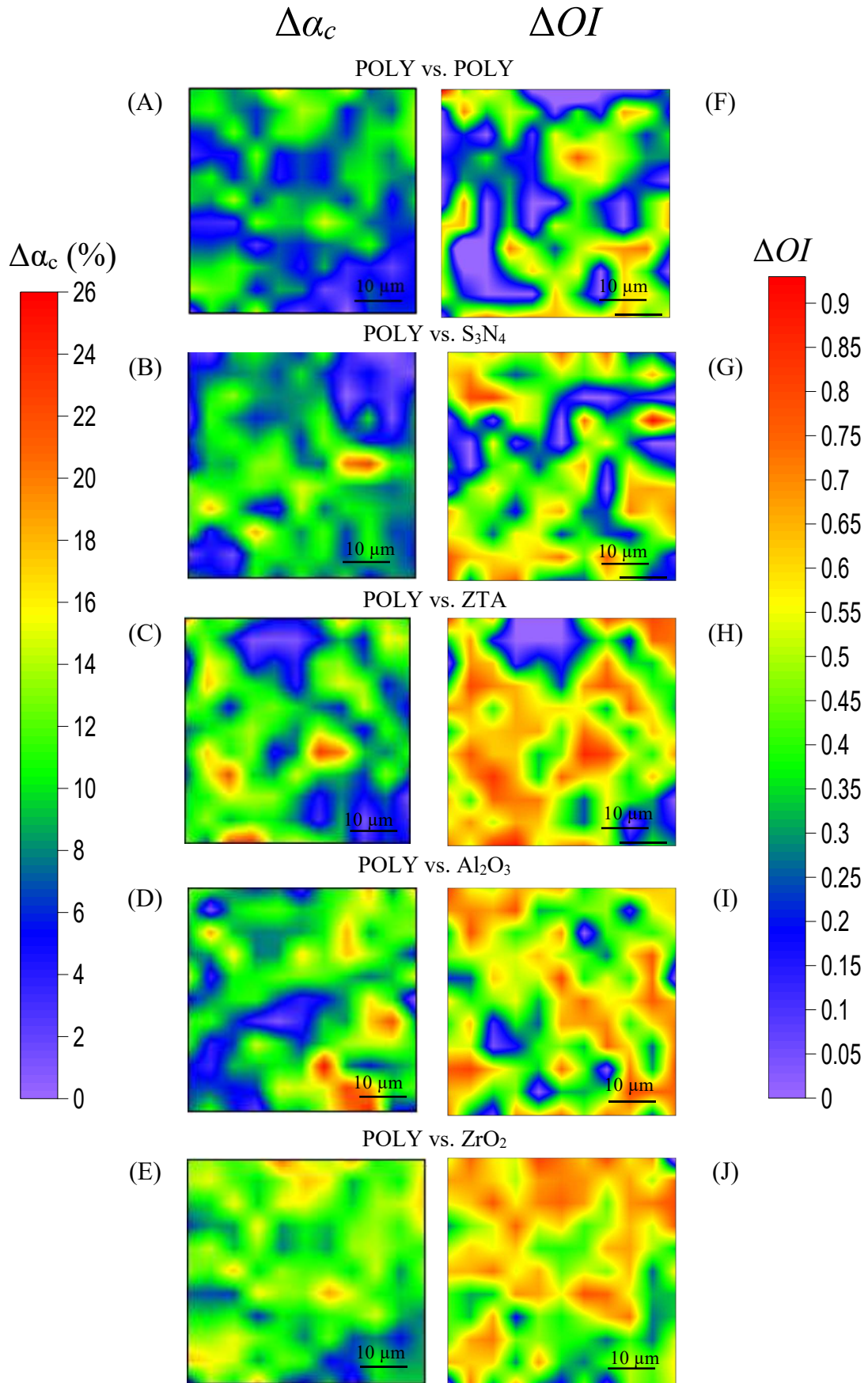
Figure 45: Maps of variations of crystallinity, $\Delta\alpha_c$, (A through E) compared to the corresponding maps of variation of oxidation index, ΔOI, (F through J)

Figure 46: Comparison between the maps of fractional variations of the crystalline, third (semi-crystalline) and amorphous phases, respectively.

5.2 XPS surface analysis

XPS surface analysis were conducted before and after accelerated aging, both on polyethylene and Si_3N_4 surfaces. The goal was to measure any possible increase of oxygen on the surface that occurred during aging in humid condition.

5.2.1 XPS on UHMWPE

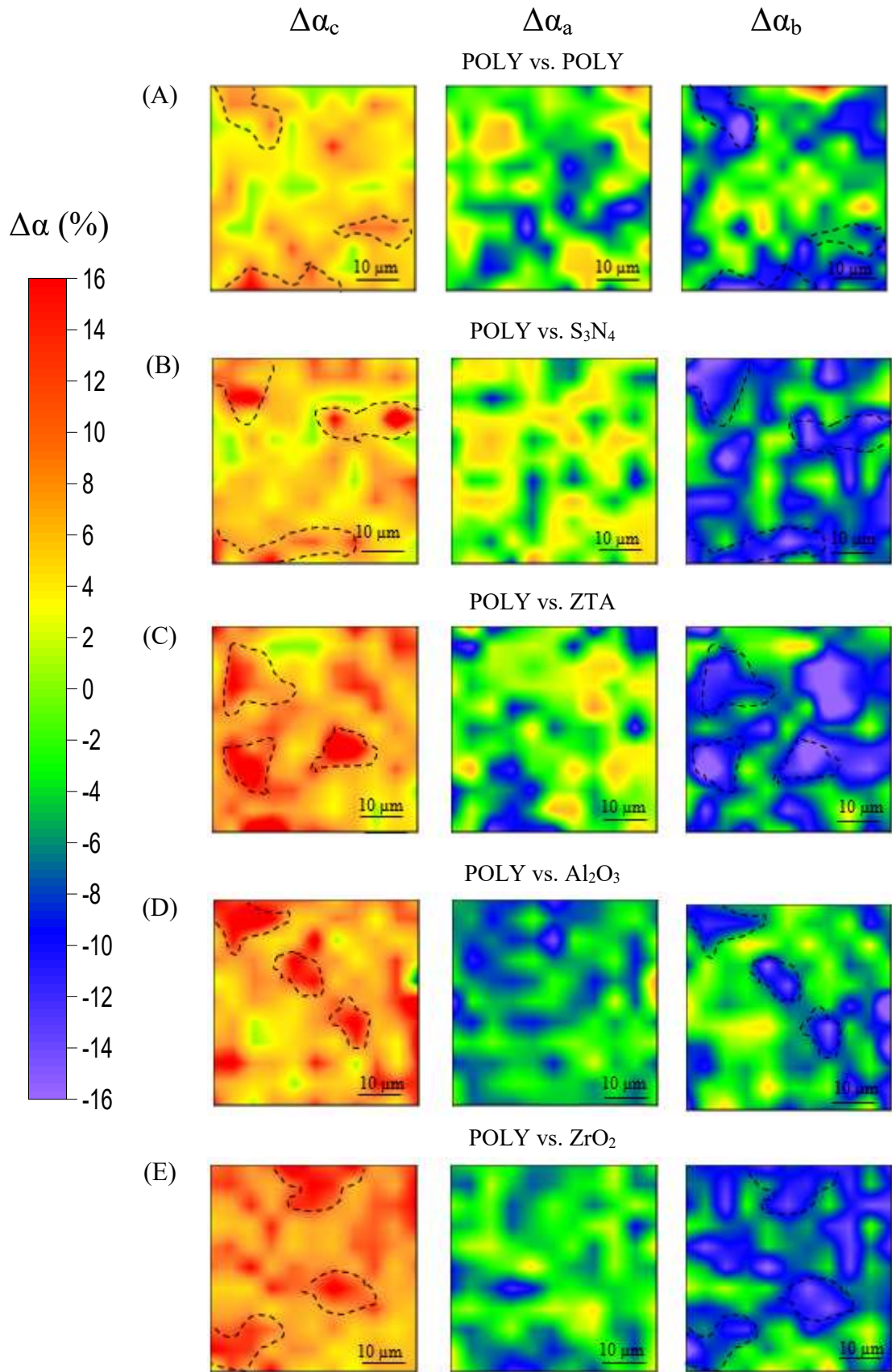The elemental fractions at the UHMWPE surface were determined, after the accelerated aging, by averaging measurements in three different zones of three different sample. All the tested couples, including UHMWPE vs. Al_2O_3, UHMWPE vs. ZTA, UHMWPE vs. m-ZrO_2, UHMWPE vs. Si_3N_4, and the control UHMWPE vs. UHMWPE, were investigated. The XPS spectra obtained were fitted with Voigtian functions and the outputs was quite homogeneous for different samples of each couple.

Figure 47 shows the comparison between averaged elemental fractions. Since the carbon signal showed quite similar very strong intensities in all the XPS spectra of differently coupled UHMWPE samples, it was omitted from the histogram. However, it must be clarified that the carbon fraction corresponds to the missing percentage to reach 100%. Emissions from N and Si are equally weak and quite constant before and after accelerated aging, and are obviously surface contaminations from machining. Moreover, they tend to disappear after robust etching. The oxygen signal was clearly stronger by at least a factor two in couples including oxide ceramics as compared to both the UHMWPE vs. Si_3N_4 and the control UHMWPE vs. UHMWPE couples.

Figure 48 shows the details of the O1s zone of the XPS spectrum of UHMWPE samples belonging to different couples after autoclaving. As is seen, the peak intensity is higher for UHMWPE samples coupled with oxide ceramics.
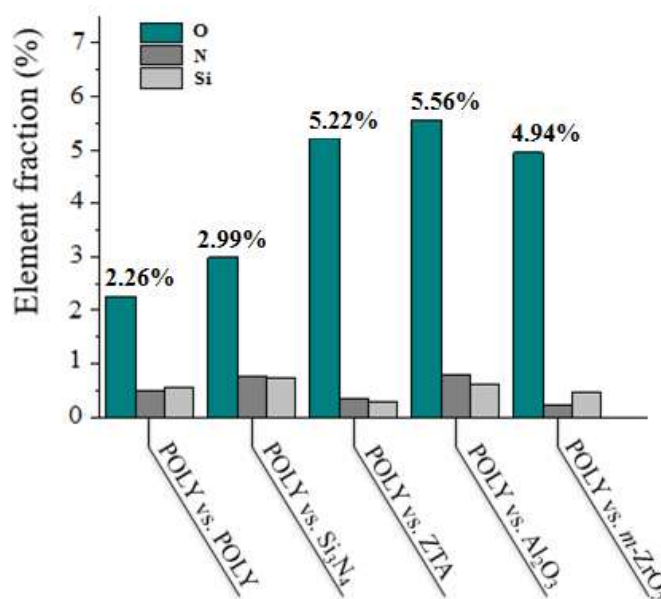
Figure 47: histogram of averaged elemental fractions of UHMWPE
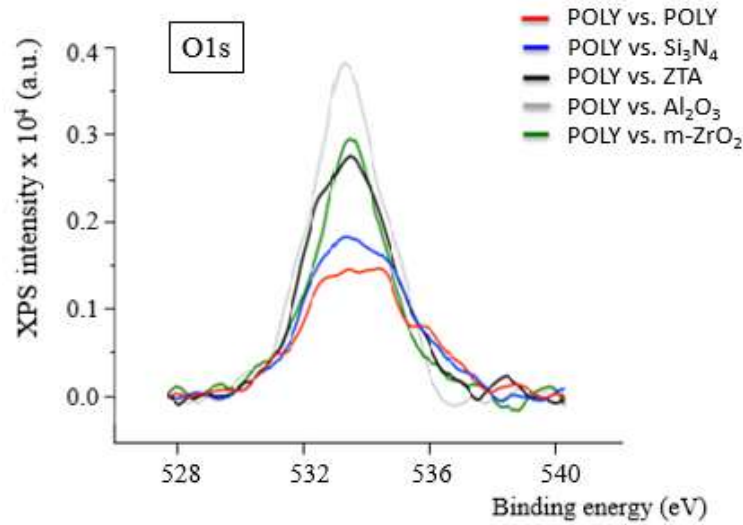
Figure 48: O1s zone of the XPS spectrum of UHMWPE

5.2.2 XPS on Si$_3$N$_4$

XPS analysis of Si$_3$N$_4$ were conducted on two unaged and two aged samples, to investigate the evolution of oxygen toward the non-oxide ceramic side upon autoclaving, explaining the "missing" oxygen fraction on the UHMWPE side as compared to UHMWPE samples coupled to oxide ceramics (see Figure 47).

Figure 49 illustrates the O1s XPS spectra obtained from exactly the same Si$_3$N$_4$ sample, before and after the UHMWPE-coupled autoclave experiment, showing the change in oxygen content at the surface of this non-oxide ceramic. While the two spectra are similar in appearance, the O1s peak after autoclaving is clearly greater in intensity, broader, and slightly shifted toward higher energy (*i.e.*, 533 eV), which is typical of Si-O bonding in silica and silicon oxynitride. This change in intensity corresponds to ~30% increase in oxygen content and correlates with the lower observed oxygen of its mated UHMWPE liner. The Si content (not shown here) decreased by ~1% after aging, which is explainable by the corresponding increase in oxygen concentration at the ceramic's surface. Similarly, the nitrogen content also decreased at the surface of the aged Si$_3$N$_4$ sample (Figure 50) although its change was not statistically significant (*i.e.*, p = 0.2). Moreover, the N1s peak was clearly shifted toward 398 eV, which is the typical binding energy of N in silicon oxynitride.
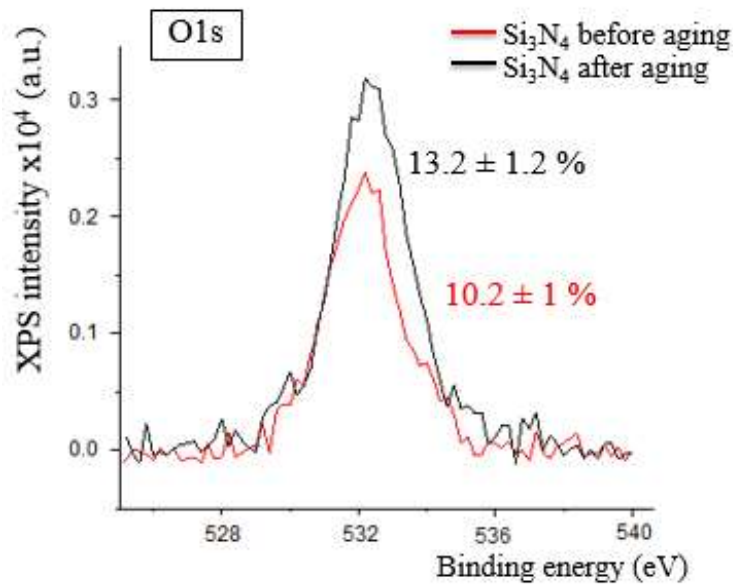
Figure 49: O1s zone of the XPS spectrum of Si_3N_4
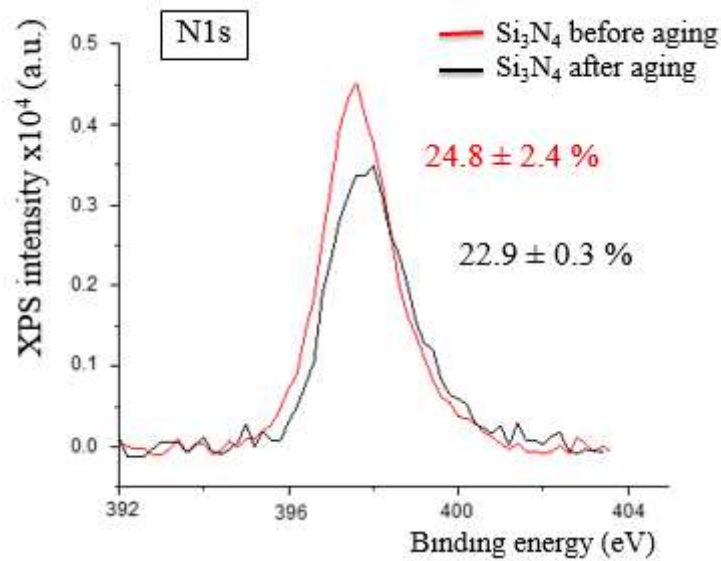
Figure 50: N1s zone of the XPS spectrum of Si_3N_4

5.3 Cathodoluminescence analysis

Preliminary experiments were carried out in order to validate the penetration depth of the electron beam during low-voltage CL data acquisition, since electron scatter depths for the investigated ceramics covered relatively narrow ranges in different ceramics. The recorded calibration data revealed that the CL analyses were always confined into depths in the range 150~250 nm.

Figure 51 shows a comparison between the CL spectra of the ZTA ceramic counterface before and after autoclaving. The spectra arises from intra-gap transitions

at oxygen vacancy sites trapping one or two electrons (i.e., V_O^* and V_0) in the Al_2O_3 lattice [177]. Under oxidizing conditions, exposure of metal oxides to vapor triggers water splitting and hydrogen dissolution into the sub-lattice, which generates hydrogen defects [178, 179], as follows:

$$H_2O \text{ (g)} + 2O_O^x \rightarrow 2(OH)_O^* + 2e' + \frac{1}{2}O_2(g) \tag{VII}$$

$$H_2O \text{ (g)} + MO \rightarrow 2H_i' + V_O^{**} + \frac{1}{2}O_2(g) \tag{VIII}$$
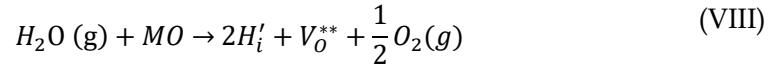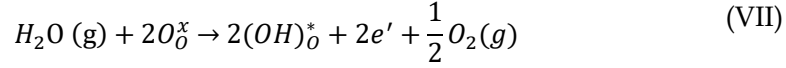
where O_O^x are oxygen on oxygen metal oxide sub-lattice sites, $(OH)_O^*$ are hydroxide ions on normal oxygen sites, e' are electron defects formed from water splitting, MO is metal oxide sub-lattice, H_i' are hydrogen interstitial defects and V_O^{**} are oxygen vacancies.

Electrons formed by hydrogen dissolution may also interact with other positive defects. They occupy energy levels in double charged oxygen vacancies, V_O^{**}, leading to the enhancement of single-charged or neutral oxygen vacancies. Therefore, the increase in CL intensity recorded for ZTA after the aging treatment may reflect the occurrence of the reactions reported in Eq. (VII) and (VIII), which show the catalytic production of oxygen from water splitting at the oxide interface.

The intensity is proportional to the concentration of the vacancies. After accelerated aging the intensity increases, as a result of a flow of oxygen atoms out of the oxide ceramic structure.
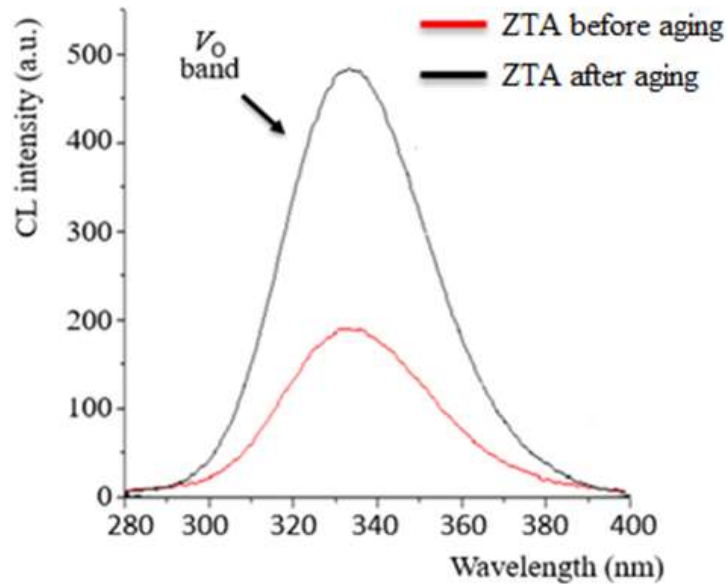
Figure 51: CL spectra of the ZTA sample before and after autoclaving in contact with UHMWPE

Conversely, Figure 52 reports on the CL spectra recorded on the Si_3N_4 surface before and after autoclaving. The emission observed in cathodoluminescence experiments is generated from inter band gap emissions (defect related energy level) in the Si_3N_4 samples, due to off-stoichiometry sites in the lattice.

According to Robertson [180, 181], the main defects in the chemically ordered Si_3N_4

network are the Si-Si and N-N like-atom bonds and the Si and N dangling broken bonds. In particular: the antibonding orbitals with an energy level of 4.6 eV are associated with Si–Si like-atom bond sites, N_4^+ vacancies defects at 3.2 eV are associated with the presence of N–N like-atom bonds, Si dangling bonds ($N_3\equiv Si^{\bullet}$, denoted as $\equiv Si^{\bullet}$ or K^0 centers) at 2.3 eV and N dangling bonds ($Si_2=N^{\bullet}$, denoted as $=N^{\bullet}$ or N_2^0 centers) at 1.3~1.5 eV [182, 183].

As reported in the literature, the fitting procedure is based on a spectral deconvolution involving 6 gaussian sub-bands (Table 9), at around 316, 380, 478, 566, 626 and 668 nm respectively, originated by defects induced by the luminescence center.

Band	Assignment	Wavelenght
1	CB$\rightarrow$$N_2^0$	316 ± 3
2	$N_4^+$$\rightarrow$VB	380 ± 2
3	CB$\rightarrow$$V_N^{3+}$	478 ± 3
4	$K^0$$\rightarrow$VB	566 ± 1
5	NBOHC (Si-O$^{\cdot}$)	626 ± 1
6	CB$\rightarrow$ N_4^+ $N_4^+$$\rightarrow$$N_2^0$	668 ± 3

Table 9: Luminescence bands in silicon nitride samples

Nitrogen-vacancy V_N^{3+} (band 3) presents the maximum emission compared to the other bands. Bands 1 and 6 nm are associated to the introduction of Al or Y ions in the silicon nitride lattice to replace Si, while bands 2 and 4 are associated to the the substitutions of N by oxygen ions. Band 5 is related to the non-bridging oxygen hole centers (NBOHC) in the SiO_2 surface as a consequence of the breakage of the bond betweeen silicon and oxygen.

As shown in Figure 52, a reduction in intensity and a clear morphology change were induced in the Si_3N_4 spectrum by the autoclaving cycle. The two main features of this spectral variation are:

(a) the reduction of the CL intensity of the N-vacancy peak located at around 478 nm, due to the formation of the silicon oxynitride glass (in agreement with the XPS data on Si_3N_4 which showed the N1s peak shifting toward higher binding energy, see Figure 50).

(b) the increase in the intensity of the CL emission at around 630 nm corresponding to a characteristic defective cluster in silica glass, which represents oxygen-rich centers of SiO [184].

The evolution of the observed CL spectra supports thus the hypothesis that an oxygen rich phase formed at the Si_3N_4 surface.
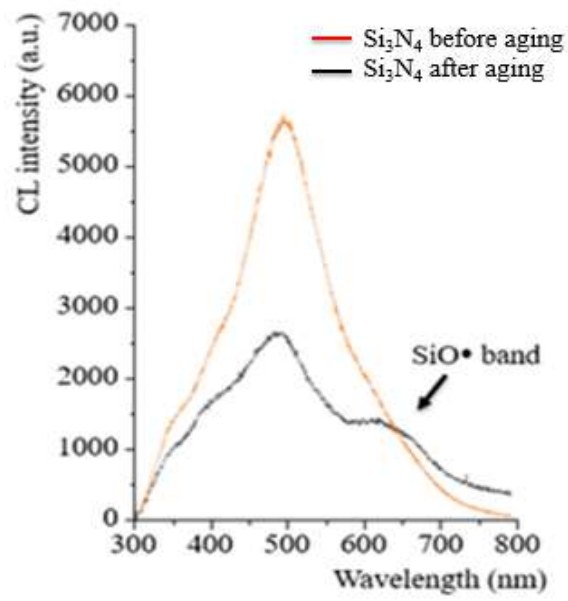
Figure 52: CL spectra of the Si_3N_4 sample before and after the autoclaving in contact with UHMWPE

Chapter 6
Discussion

As widely discussed in literature, ionizing radiations form free radicals through the radiolytic cleavage of C-H and C-C bonds in polyethylene. These free radicals recombine with each other and form cross-links in the microstructure of the polymer. The free radicals generated during irradiation, however, become trapped in the crystalline phase [185] and adversely affect the long-term oxidative stability of the material.

On the long-term period, the presence of residual free radicals causes embrittlement [74]. Oxidative embrittlement of UHMWPE is initiated when the residual free radicals react with oxygen. A complex cascade of events leads to the formation of peroxy free radicals, hydroperoxides, and ultimately carbonyl species, mainly ketones, esters, and acids. The formation of these species can be accompanied by chain scission, reducing the molecular weight of the polymer. This eventually leads to recrystallization, increase in stiffness, and embrittlement of the UHMWPE component, decreasing mechanical properties and wear resistance of the material.

As expected, all the gamma irradiated UHMWPE samples underwent oxidation during accelerated aging, revealing increased crystallinity. In fact, increasing crystallinity values were generally observed after exposure in autoclave environment. As later will be discussed, despite similar maximum crystallinity in correspondence of the hot spots, clear differences could be found among different tested samples, especially for the UHMWPE samples aged in contact with oxide ceramics.

To state which UHMWPE phase underwent the most oxidation, fractional differences at exactly the same locations for the crystalline, third (semi-crystalline) and amorphous phases were compared (see Figure 46). This microscopic analysis revealed that the major fraction of newly formed crystalline phase developed at the expenses of the third phase, while only a minor variation could be found in the local pattern of amorphous phase fraction.

According to previous publications on the crystallization behavior of UHMWPE, [186, 187, 188], the oxidation process leads ultimately to the breaking and shortening of polyethylene chains. Enhancement of their molecular mobility enables the chains to reorganize into an ordered structure of lower free energy. It has also been demonstrated that irradiation of polyethylene triggers recrystallization for the same reasons, [189, 190, 191], with small angle x-ray scattering revealing an increase in lamellar thickness after exposure to γ-rays [192]. Combined studies of gamma irradiated samples show in fact that chain scission occurs on the surface and crosslinking in the center. The chain scissioning on the surface of the sample creates the molecular mobility needed in the amorphous region to form new crystals and breaking of the tie chains and loops in the interface that allow for growth of already existing crystals [193].

Considering these prior experimental observations, it can be hypothesized that in the early stages of oxidation, the decrease of the third rather than the amorphous phase is correlated with an increase in polyethylene lamellar thickness. In fact, the third phase is the intermediate layer that separates the ordered lamellae of the crystalline phase from the random organization of the amorphous phase. This connecting phase is characterized by polyethylene molecules aligned in the same direction as the lamella axis, but without the lateral order of the orthorhombic structure, presumably due to boundary stresses generated by the highly entangled chains of the adjacent amorphous phase. The onset of oxidation and reduction of molecular weight may have released these stresses enabling the molecular chains to reacquire their lateral order, which led to lamellar thickening. If from one hand it is well known that oxygen dissolves mainly in the amorphous phase rather than in the third phase, while it cannot diffuse in the tightly packed lamellae [194], on the other hand, during aging, the free radical availability in the third phase might have been higher than that in the amorphous phase. In fact, many free radicals remain trapped in the crystalline lamellae after irradiation because they are not able to recombine forming cross-links. They eventually migrate outside, leaving the crystalline phase and entering the third phase.

In other words, the formation of oxidized species can occur in both the amorphous and intermediate phases, causing, in both cases, a release of stress within the interconnected structure, a reduction of the third phase, and a concurrent increase in lamellar thickness, which will lead to a decrease in material toughness. A schematic diagram depicting the chain-scission and subsequent re-crystallization mechanisms is provided in Figure 53.
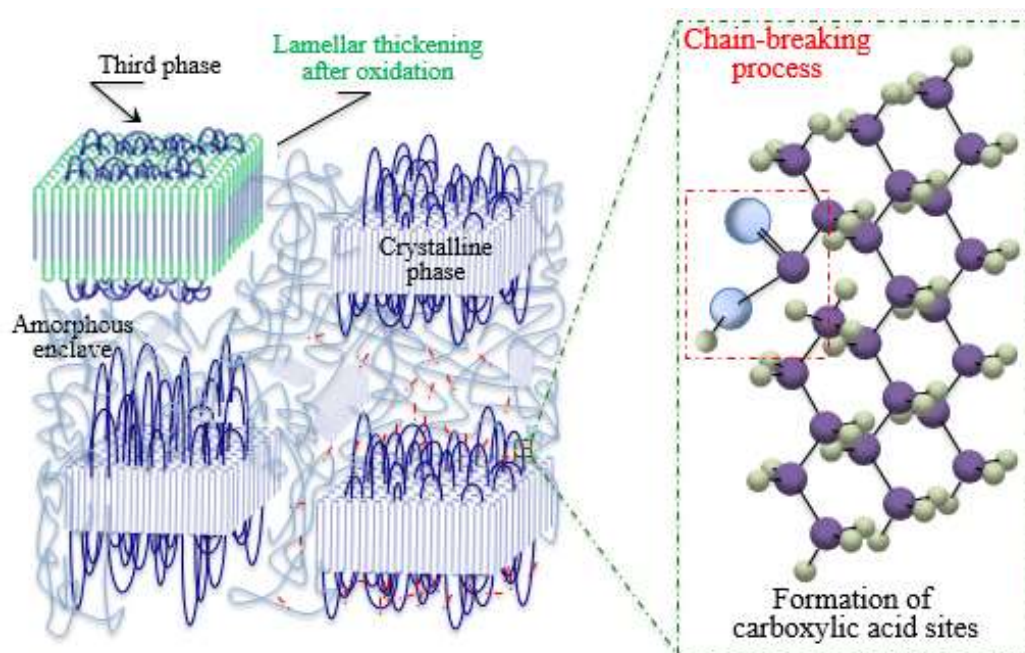

Figure 53: Diagram describing the chain-scission and secondary crystallization mechanisms

Summarizing the obtained spectroscopic results, it is evident that altered crystallinity and oxidation index values are induced by the presence of different femoral head counterparts. It is worth noting that statistically relevant differences between polyethylene coupled with oxide and non-oxide ceramics were detected, even if one of the most innovative UHMWPE on the market was chosen and testing was conducted under static conditions. In fact static coupling, short-term exposure, and relatively low environmental temperature, should in principle lead to the observation of a least amount of microstructural burden on the UHMWPE side. However, the experiments revealed a role of the head counterpart in the evolution of the near-surface UHMWPE microstructure in hydrothermally activated environment.

In detail, the contact UHMWPE vs. UHMWPE is the one that gives the least burden to the microstructure, at most because oxygen molecules could have similar probability to diffuse into either parts of the couple. Accordingly, the concave side of this homogenous couple is the least affected by evolutional changes in terms of enhanced crystallinity and oxidation index. Conversely, clear difference was found between UHMWPE liners coupled with oxide and non-oxide heads. The collected data would suggest that femoral heads made of oxide ceramics are not as effective as those made of Si_3N_4 in preventing some oxygen dissolved in body fluids from reaching the polyethylene surface. In other words, non-oxide head components may play a protective role for the polymeric component. In fact, the oxidation rate of irradiated polyethylene depends on the amount of free radicals present in the polymer and on the concentration of available oxygen for fixed temperature and time of exposure. From this point of view, for fixed environmental conditions, the amount of oxygen made available to diffuse toward the UHMWPE side may have been larger for liners coupled with oxide than non-oxide ceramic heads.

These results suggest a mechanism of surface chemistry whereby oxidative degradation of UHMWPE liners may be delayed *in vivo* through the oxygen scavenging action of non-oxide ceramic femoral heads. This behavior may rely on the peculiar physical chemistry of Si_3N_4 surfaces, terminating with a silicon rich layer, which undergoes the steady growth of an amphoteric SiO_2-rich layer, thus attracting oxygen from the surrounding environment [195]. The O_2 chemisorption rate is fast, leading to quick saturation. In the case of Si_3N_4 surfaces interacting with liquid solutions, although the chemisorption of H_2O does not proceed as fast as in the case of molecular oxygen, it equally leads to the formation of a chemically stable oxide (or oxynitride) surface layers and the surface H:O ratio is ~1:1. The structure of a silicon oxide layer naturally formed on a Si_3N_4 surface is schematically illustrated in Figure 54.
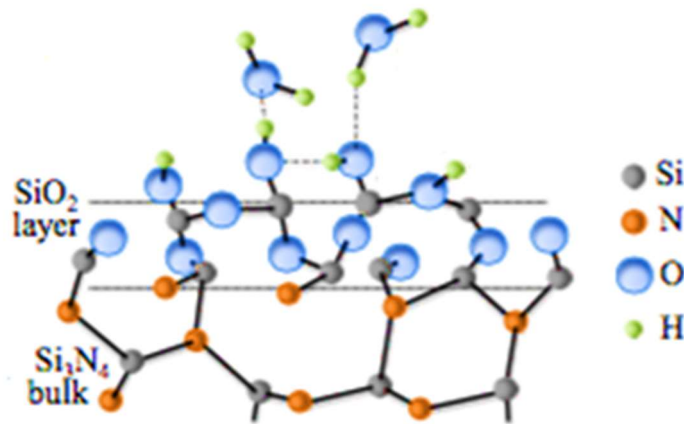
Figure 54: Molecular structure of a silicon oxide layer naturally formed on a Si3N4 surface

The reactions governing the formation of this SiO_2-rich layer are given by the following equations [196]:

$$Si_3N_{4(s)} + 3O_{2(g)} \rightarrow 3SiO_{2(s)} + 2N_{2(g)} \qquad \text{(IX)}$$

$$Si_3N_{4(s)} + 6H_2O_{(l)} \rightarrow 3SiO_{2(s)} + 4NH_{3(g)} \qquad \text{(X)}$$
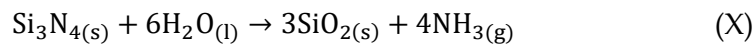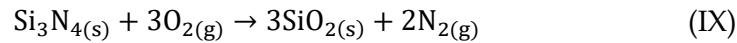
However, the near-surface region is composed of Si–N, Si–N–O, and Si–O bonds and for this reasons the surface chemistry of Si_3N_4 becomes more complex than how Equations (IX) and (X) would indicate [197].

Figures 55 (a) and (b) provide a hypothesis for the cascading set of events that occurred at the wet interface between Al_2O_3 and UHMWPE counterparts during hydrothermal activation. According to Equations (VII) and (VIII), water molecules splitting at the interface with Al_2O_3 produced dissolution of hydrogen and defective electrons in the sub-lattice and the catalytic formation of free oxygen molecules into the tribolayer. Then, this oxygen flowed toward and reacted with the UHMWPE surface in accordance with the oxidation mechanisms above described. XPS spectra of UHMWPE (Figure 47) and CL spectra of alumina-zirconia counter-surface (Figure 51) statistically confirm this hypothesis.

The formation of oxygen promoted by the Al_2O_3 into the water interlayer might have enhanced the crystallization (Δa_c) and oxidation (ΔOI) of the UHWMPE. Note especially that the other two oxide ceramics (*i.e.*, ZTA and *m*-ZrO_2) generated crystallization and oxidation indices in their respective UHMWPEs that were not statistically different than those produced in the Al_2O_3/UHMWPE couple. These results are perhaps not surprising given that the formation of hydrogen defects in zirconia sub-lattice has also been reported as possible in oxygen rich and oxygen poor conditions [179].

Figures 56 (a) and (b) show an opposite model of the events leading to oxygen scavenging by Si_3N_4 in contact with its UHMWPE counterpart during hydrothermal activation. In the autoclave environment, the wet interface produced a flow of oxygen out of the tribolayer toward the non-oxide ceramic. This free oxygen reacted with the

Si₃N₄ to form a silicon oxynitride glass phase at its surface. Therefore, this process protected the UHMWPE surface from a fraction of the oxygen dissolved in the water interlayer, and consequently limited the extent of the chain-scission/re-crystallization occurring at the surface of its UHWMPE counterpart.
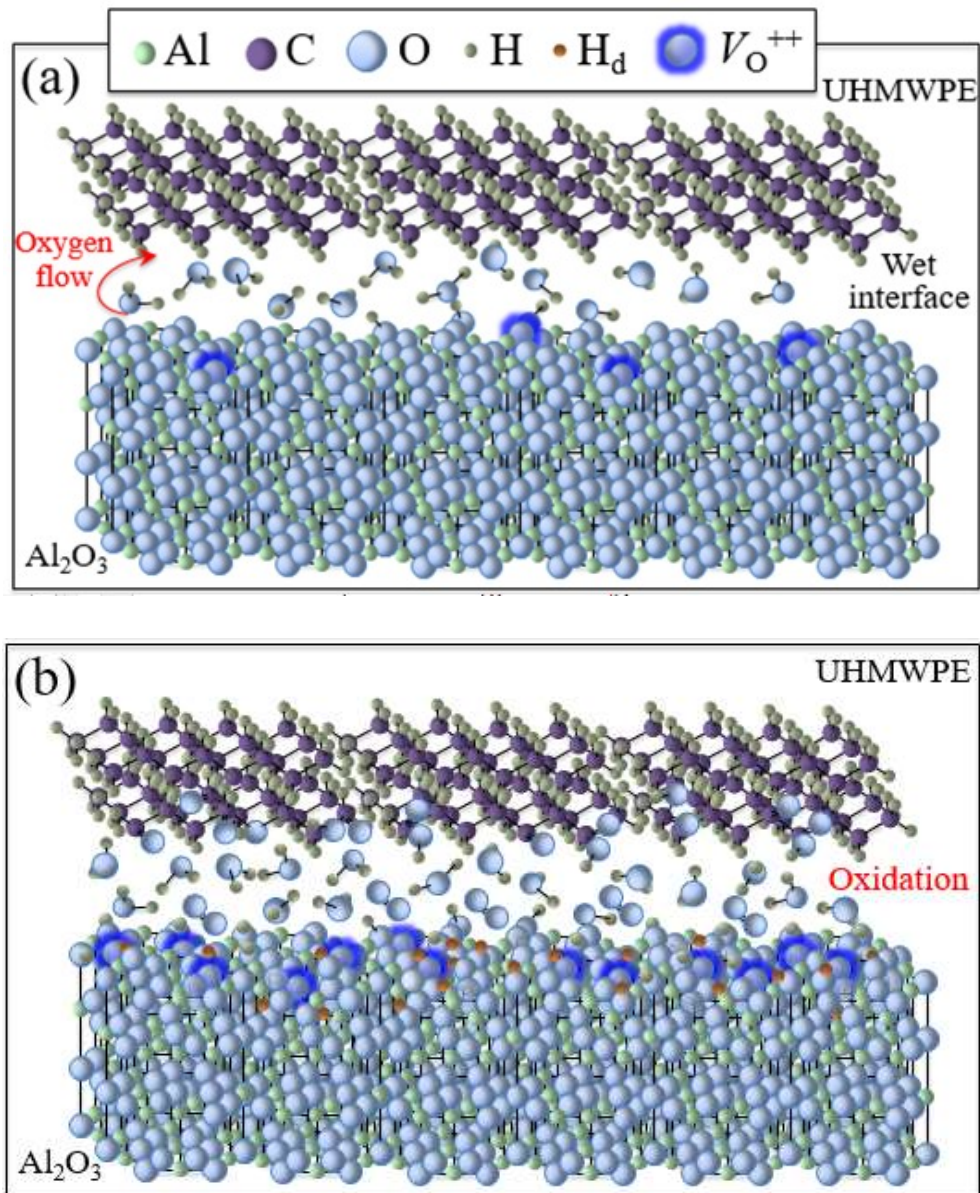
Figure 55: The interaction occurring at the interface between Al_2O_3 and UHMWPE during hydrothermal activation. An initially nearly stoichiometric Al_2O_3 surface (a) diverges toward oxygen off-stoichiometry; and, (b) forms hydrogen defects (H_d) and oxygen vacancies along with oxygen molecules dissolved in water
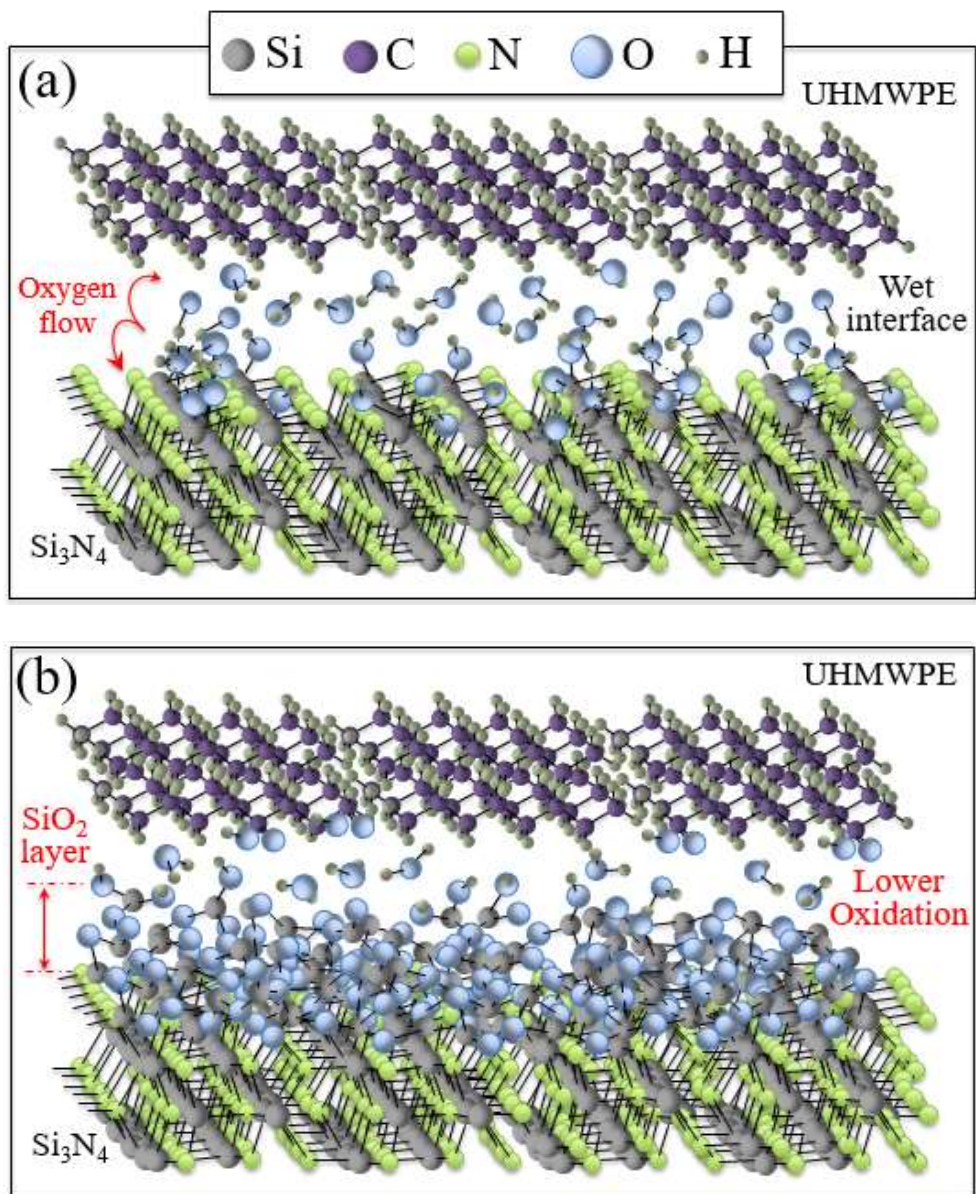
Figure 56: The interaction occurring at the interface between Si_3N_4 and UHMWPE during hydrothermal activation. The pristine Si_3N_4 surface (a) forms a layer of silicon oxynitride, and, (b) attracts free oxygen from the interface thereby protecting the UHMWPE structure from oxidation

Chapter 7
Conclusions

By employing various surface spectroscopy tools, the aim of the present study was to verify a method for determining oxygen stoichiometry in UHMWPE/ceramic couples subjected to static contact in a hydrothermally activated environment. In particular, it was investigated how the surface chemistry of ceramic materials may affect the oxidative degradation and joint lifetime of polyethylene liners.

The main outputs obtained by means of Raman, X-Ray Photoemission and Cathodoluminescence spectroscopy, can be summarized, as follows:

(i)   Oxygen affinity of various bioceramics plays a fundamental role in the degradation of UHMWPE.

(ii)   Oxide ceramics are not bio-friendly to polyethylene. It was shown that during hydrothermal aging, their surfaces catalyze the reaction of water splitting and production of molecular oxygen that may diffuse toward and react with their polyethylene counterparts.

(iii)   Conversely, non-oxide Si_3N_4 appeared to be a polyethylene friendly bioceramic because it trapped oxygen at its surface, thereby delaying the oxidative degradation of its UHMWPE counterpart. This latter behavior relies on the peculiar physical chemistry of Si_3N_4 surfaces, which terminate with a silicon rich layer, which undergo the steady growth of an amphoteric SiO_2-rich layer, thus attracting oxygen from the surrounding environment.

(iv)   The third (semi-crystalline) phase of the UHMWPE showed an increase in oxidation, while the amorphous phase was less affected.

The evidences provided in this study clearly substantiate the importance of oxygen chemistry at the interface of UHMWPE and bioceramic couples even under static circumstances.

Further assessments under dynamic conditions are needed to validate the clinical relevance of this new tribochemical paradigm.

It is noteworthy that monitoring the surfaces of bioceramic/UHMWPE couples could be adopted as a new *in vitro* evaluation technique for assessing and predicting polyethylene degradation in artificial hip joints. Its use could lead to both improved materials and designs, resulting in enhanced device lifetimes.

Chapter 8
Appendix
Introduction to Spectroscopy

In this study some different spectroscopic techniques were used, namely, Raman, cathodoluminescence (CL) and XPS spectroscopy. Therefore, a quick description of these techniques, from both theoretical and applicative point of view, is provided in the following chapter.

The science known as spectroscopy is a branch of physics regarding the study of radiation absorbed, reflected, emitted, or scattered by a substance after its interaction with solids, liquids or gases materials, no matter whether the radiation is electromagnetic, mechanic or embodied in particles [198]. In fact, although, the term 'radiation' only deals with photons, in spectroscopy it also involves the interactions of other types of particles, such as neutrons, electrons, and protons, which are used in investigating the matter [199].

The analysis of the radiation spectrum after its interaction with the electronic and magnetic configuration of the material system allows obtaining physical information regarding the material under examination.

Experimentally all the available spectroscopic methods are based on the use of a proper excitation source, a sample that interacts with the beam and a detection apparatus for the probe. Depending on the nature of the excitation source, it is possible to distinguish several spectroscopic techniques, which lie in different portions of the electromagnetic energy spectrum.

Figure 57 offers a good panoramic view of different spectroscopic methods, associated with specific portions of the electromagnetic spectrum. In particular, the Raman spectrum is generated from the interaction between a beam of irradiating light and the vibrations that occur in a crystal at discrete frequencies. Therefore, as direct expressions of the details of the vibrational modes themselves, the Raman bands are intimately related to the crystallographic structure.

While Raman spectroscopy can provide a detailed picture of the material structure, CL spectroscopy, is capable of visualizing surface vacancies through their optical activity. Moreover, the penetration depth of electrons depends on the energy of the impinging electron beam; therefore, using low acceleration voltages, the probing depth can be confined to the nanometer range, thus obtaining a spatial resolution several orders of magnitude higher as compared to Raman laser probes.

XPS spectra are obtained by irradiating a material with a beam of X-rays while simultaneously measuring the kinetic energy and number of electrons that escape from the first nanometers of the material being analyzed. XPS can thus be used to analyze the surface chemistry of a material.
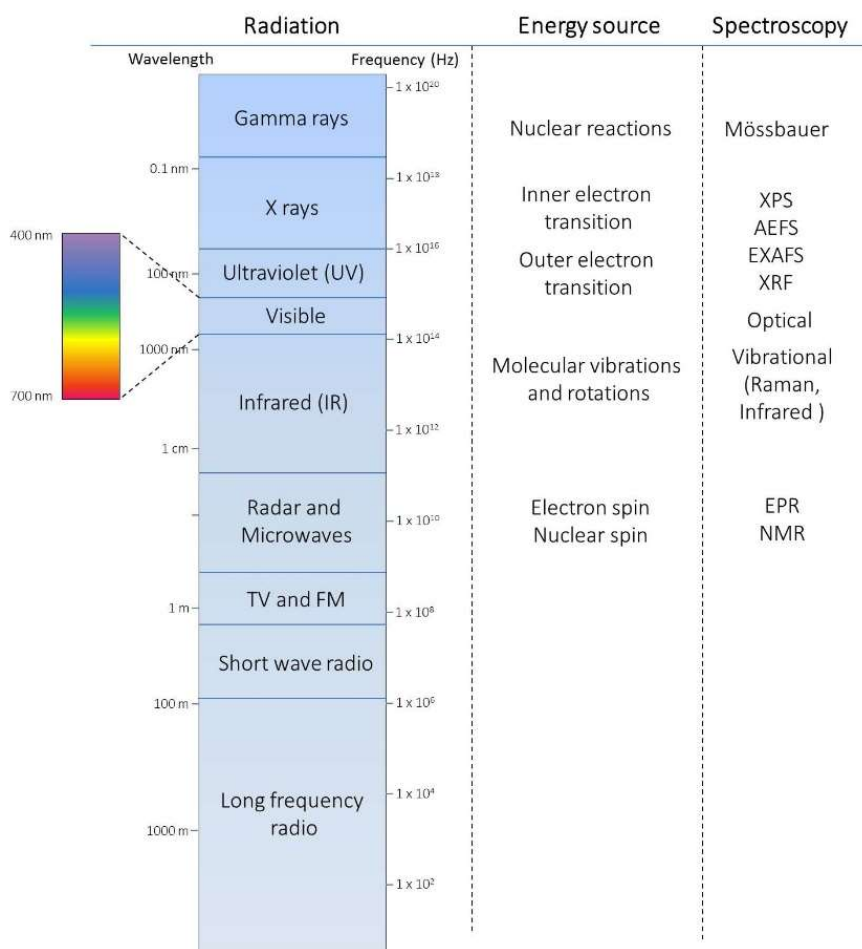
Figure 57: The different regions of the electromagnetic spectrum in relationship with different energy sources and spectroscopic methods

8.1   Raman Spectroscopy

8.1.1 Introduction to Raman Spectroscopy

Raman spectroscopy can be described as a spectroscopic technique generally used in condensed matter physics and chemistry for studying vibrational, rotational, and other low-frequency modes in a system. This technique is based on the inelastic scattering of monochromatic light after its interaction with a material system.

The first independent prediction of the inelastic scatter of light was made by Adolf Smekal in 1923 [200], just few year before its experimental proof made by Sir Chandrasekhara Venkata Raman in 1928 [201], who received the Nobel prize for his discovery in 1930. Despite the successful theoretical description of the underlying effect, Raman spectroscopy developments occurred quite slowly before the 1960s because of experimental problems such as the very weak intensity of the Raman band, compared with the much greater intensity of the Rayleigh scattering, and the several hours exposure time for obtaining a photographic record of the spectrum of scattered

64

light. The quality of the recorded spectra increased considerably with the advent of laser sources. The advantages brought by this new technology were the capability to focus a very intense light onto the samples and the wide range of available exciting wavelengths, which can mitigate or even suppress undesired fluorescence emission. In fact the monochromatic laser source is now selected depending on the sample to investigate, varying its wavelength in the visible, in the near visible or in the near ultraviolet range. During the last decades, huge improvements were made also in the detection system technology. The first step was the developments of high sensitivity photomultipliers tube in the 1970s. Although, the real revolution was the invention of the charge coupled device (CCD) and its utilization as a Raman detector in 1987. This system allows a time-resolved signal acquisition, making possible to record an entire spectrum of wavelength in a time in an order of magnitude of seconds [202]. Therefore, following the technology improvements in optics, microelectronics and computer science modern Raman spectroscopy has become very sophisticated.

8.1.2 Scattering process

When light interacts with matter, the photons may be absorbed or scattered, or may not interact with the material and may pass straight through it. If the energy of an incident photon corresponds to the energy gap between the ground state of a molecule and an excited state, the photon may be absorbed and the molecule promoted to the higher energy excited state. This change is measured in absorption spectroscopy by the detection of the loss of that energy of radiation from the light. It is also possible for the photon to interact with the molecule and scatter from it. In this case, there is no need for the photon to have an energy that matches the difference between two energy levels of the molecule [203].

There are many forms of scattering, such as: Debye or Mie (elastic scattering, which occurs from relatively large particles or molecules with dimensions comparable with the wavelength of the incident radiation), Brillouin (inelastic scattering, which typically occurs in scattering from solid materials), Thompson (elastic scattering where light is scattered by charged particles), Compton (an inelastic form of Thompson scattering), but the main scattering mechanisms are Rayleigh and Raman scattering.

Rayleigh is an elastic scattering from small particles such as atoms or molecules, which is dependent on wavelength, with shorter wavelengths being more scattered.

Raman is an inelastic scattering mechanism where the frequency of the scattered radiation is changed by the gain or loss of energy, which corresponds to energy levels in an atom or molecule. A light wave, meant as a propagating oscillating dipole can interact and distort the cloud of electrons around the nuclei of a molecule, which size is much smaller than that of the oscillating dipole. The oscillating dipole causes the electrons to polarize and go to a higher energy state. At that instant, the energy present in the light wave is transferred into the molecule. This results in a high energy form of the molecule, often called the virtual state of the molecule, that is unstable and therefore the light is released immediately as scattered radiation. The process differs

from an absorption process in many ways: the additional energy does not promote an electron to any one excited state of the static molecule and the lifetime of the excited state is very short compared to most absorption processes. Moreover, the radiation is scattered as a sphere and not lost by energy transfer within the molecule or emitted at a lower energy.

The most intense form of scattering is Rayleigh scattering, which occurs when the electron cloud relaxes without any nuclear movement. If only electron cloud distortion is involved in scattering, the photons will be scattered with very small frequency changes, as the electrons are comparatively light. This scattering process is regarded as elastic (the electron decays back to the same level from which it started and there is no appreciable change in energy) and is the dominant process.

Raman scattering on the other hand is a much rarer event which involves only one in 10^6–10^8 of the photons scattered. This occurs when the light and the electrons interact and the nuclei begin to move at the same time. Since the nuclei are much heavier than the electrons, there is an appreciable change in energy of the molecule and the process is inelastic (the excited molecule relaxes to a vibrational level different from the original state) [203]. The final vibration state of the molecule can be either higher or lower in energy than the original state (Figure 58). If the molecule is in its ground vibrational state (m), the Raman scattering process leads to absorption of energy by the molecule and its promotion to a higher energy excited vibrational state (n), so the scattered radiation is of a lower frequency than the excitation radiation. Raman bands of this type are referred to as Stokes lines. However, due to thermal energy, some molecules may be present in an excited state (higher vibrational state, n). Scattering from these states to the ground state (m) is called anti-Stokes scattering and involves transfer of energy to the scattered photon. The scattered radiation has a higher frequency than the source radiation [204].
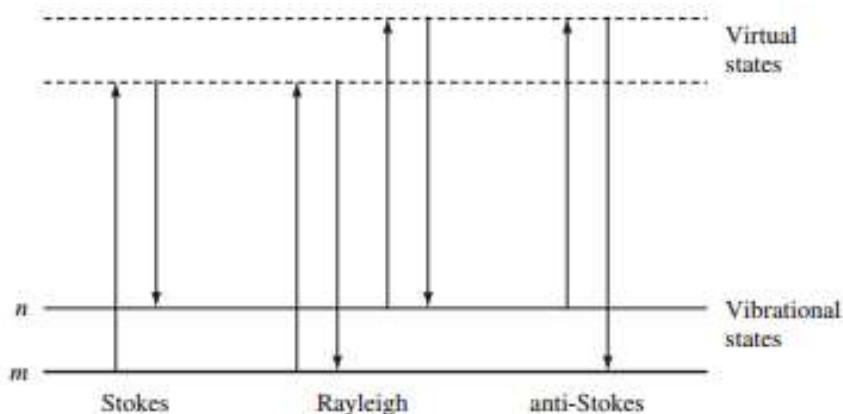
**Figure 58**: Diagram of the Rayleigh and Raman scattering processes. The two states marked m and n are different vibrational states of the ground electronic state

The relative intensities of the two processes depend on the population of the various states of the molecule. The populations can be calculated from the Boltzmann equation, however at room temperature, the number of molecules expected to be in an

excited vibrational state will be small. Thus, compared to Stokes scattering, anti-Stokes scattering (Figure 59) will be weak and will become weaker as the frequency of the vibration increases, due to decreased population of the excited vibrational states. Usually, Raman scattering is recorded only on the low-energy side to give Stokes scattering, but occasionally anti-Stokes scattering is preferred. For example, fluorescence interference occurs at a lower energy than the excitation frequency and consequently anti-Stokes scattering can be used to avoid interference [203].

Rayleigh scattering has a considerably higher probability of occurring than Raman scattering because the most probable event is the energy transfer to molecules in the ground state and reemission by the return of these molecules to the ground state.
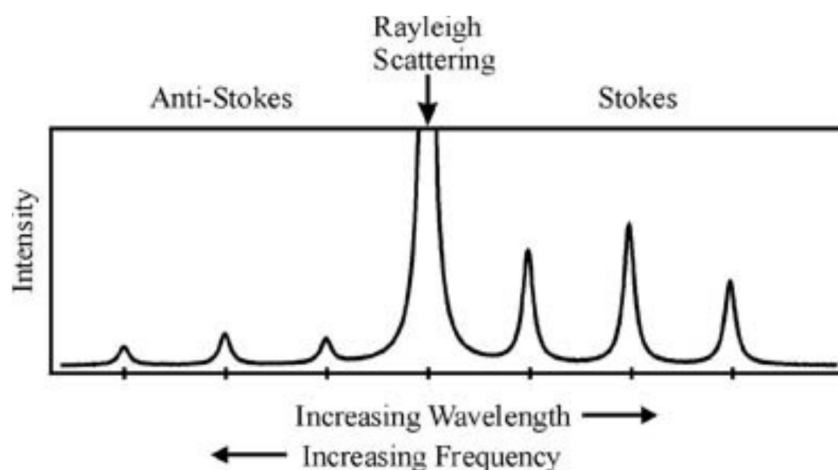
Figure 59: Raman spectrum of carbon tetrachloride, obtained with a laser having a wavelength of 488.0 nm as the source

A Raman spectrum shows a plot of light intensity (usually given in counts, counts per second or arbitrary units) versus wavenumber shift, which is defined as the difference in wavenumbers (cm⁻¹) between the observed radiation and that of the source $\Delta\tilde{v}$. By IUPAC convention a given Raman band is thus identified in the spectrum by a quantity called Raman shift $\Delta\tilde{v}$, which is the difference between the wavenumber of the exciting source $\tilde{v}_0$ and that of the scattered light $\tilde{v}'$:

$$\Delta\tilde{v} = \tilde{v}_M = \tilde{v}_0 - \tilde{v}' \qquad\qquad (XI)$$

$\Delta\tilde{v}$ is positive for Stokes Raman band and negative for anti-Stokes line. Raman lines are found on both sides of the Rayleigh lines and the pattern of shifts on each side is identical.

Because the anti-Stokes lines are appreciably less intense than the corresponding Stokes lines, only the Stokes part of a plot is often considered and labelled simply wavenumber v, (cm⁻¹), rather than wavenumber shift $\Delta\tilde{v}$. It is noteworthy that fluorescence may interfere seriously with the observation of Stokes shifts but not with anti-Stokes. With fluorescing samples, anti-Stokes signals may, therefore, be more useful despite their lower intensities [205].

8.1.3 Wave Model of Raman

The electric field E of an incident beam of radiation on a solution of an analyte, having a frequency ν_0, can be described by the following equation:

$$E = E_0 \cos(2\pi\nu_0 t) \qquad \text{(XII)}$$

where E_0 is the amplitude of the wave. This electric field, upon interaction with an electron cloud of an analyte bond, induces a dipole moment m in the bond, given by:

$$m = \alpha E = \alpha E_0 \cos(2\pi\nu_0 t) \qquad \text{(XIII)}$$

where α is a proportionality constant called the *polarizability* of the bond. This constant is a measure of the deformability of the bond in an electric field and varies as a function of the distance between nuclei according to the equation:

$$\alpha = \alpha_0 + (r - r_{eq})\left(\frac{\partial \alpha}{\partial r}\right) \qquad \text{(XIV)}$$

where α_0 is the polarizability of the bond at the equilibrium internuclear distance r_{eq} and r the internuclear separation at any instant. The change in this distance varies with the frequency of the vibration ν_m according to:

$$r - r_{eq} = r_m \cos(2\pi\nu_m t) \qquad \text{(XV)}$$

where r_m is the maximum internuclear separation relative to the equilibrium position. Substituting Equation (XV) into (XIV) gives:

$$\alpha = \alpha_0 + \left(\frac{\partial \alpha}{\partial r}\right) r_m \cos(2\pi\nu_m t) \qquad \text{(XVI)}$$

Substituting Equation (XVI) into Equation (XIII) we can obtain an expression for the induced dipole moment m:

$$m = \alpha_0 E_0 \cos(2\pi\nu_0 t) + E_0\, r_m \left(\frac{\partial \alpha}{\partial r}\right) \cos(2\pi\nu_m t)\cos(2\pi\nu_o t) \qquad \text{(XVII)}$$

Using the trigonometric identity for the product of two cosines

$$\cos x \cos y = \{\cos(x + y) + \cos(x - y)\}/2$$

From Equation (XVII) can be obtained:

$$m = \alpha_0 E_0 \cos(2\pi\nu_0 t) + \frac{E_0}{2} r_m \left(\frac{\partial \alpha}{\partial r}\right) [2\pi t(\nu_0 - \nu_m)]\cos(2\pi\nu_o t) \qquad \text{(XVIII)}$$
$$+ \frac{E_0}{2} r_m \left(\frac{\partial \alpha}{\partial r}\right) [2\pi t(\nu_0 + \nu_m)]\cos(2\pi\nu_o t)$$

The first term of Equation (XVIII) represents Rayleigh scattering, which occurs at the excitation frequency ν_0. The second and third terms correspond to the Stokes and anti-Stokes frequencies of $\nu_0 - \nu_m$ and $\nu_0 + \nu_m$, respectively. Selection rules for

Raman scattering require that there be a variation in polarizability during the vibration, $(\frac{\partial \alpha}{\partial r})$ must be greater than zero for Raman lines to appear. The selection rules also predict that Raman lines corresponding to fundamental modes of vibration occur with $\Delta v = \pm 1$. Much weaker overtone transitions appear at $\Delta v = \pm 2$. For a given bond, the energy shifts observed in a Raman experiment should be identical to the energies of its IR absorption bands, provided the vibrational modes involved are both IR and Raman active [205].

8.1.4 Raman Instrumentation

Raman apparatus able to record Raman spectra generally consists of five main components: a source of monochromatic light to induce the Raman scattering; a microscope device to focus incident and collect the Raman light; a spectrograph, that split the collected light in a spectrum of frequencies, a detector, which transduces the light in an electrical signal; a post- acquisition software, which serves as visual interface able to display the spectrum of frequency. The instrumentation, which is able to correctly visualize and display a noise-free Raman scattering spectrum, consists also in several fundamental component. Among them is worthy to note the notch filter that can cut-off the elastic Rayleigh scattering of the laser and the optical polarizer, which enables the collection of the polarized Raman light).

An overall view of the instrument is shown in Figure 60.
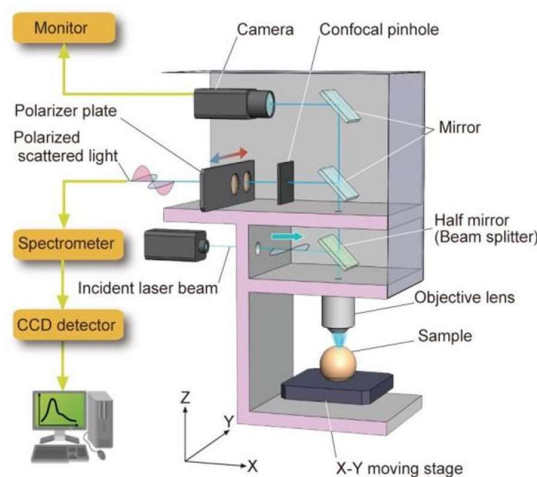
Figure 60: Schematic draft of the T-64000 Raman spectrophotometer.

All the experimental Raman data reported in this thesis were obtained in backscattering optical probe configuration with using a triple monochromator (T-64000, Horiba/Jobin-Yvon., Kyoto, Japan) equipped with liquid nitrogen-cooled charge coupled device (CCD). The T64000 spectrometers can basically work in two different modes: a single configuration in which only one monochromator, the spectrograph, is employed and a triple configuration, in which a double (twin) 1800gr/mm grating works as a pre-monochromator before the spectrograph. The

detector used to acquire the spectrum is a multichannel 1024 x 256 pixels CCD camera device (CCD-3500V, Horiba Ltd., Kyoto, Japan) mounted in the plane of the exit image. The CCD is liquid-nitrogen cooled down to 140 K. During the experiments, the laser line used as light excitation source was a continuous wave (CW) water-cooled 488 nm Ar-ion laser (Stabelite 2017, Spectra Physics, Mountain View, CA, USA). The laser beam is focused on the sample by means of an optical microscope, which has three different objective long focus lenses: a 100x objective lens with NA=0.9, a 50x objective lens with NA=0.X and a 20x objective lens with NA=0.9. The 100x objective lens, the most used during the experiments, and allows obtaining a spot size of about 1 μm. Since the light is collected in backscattering configuration, the scattered light must be separated from the incident beam using a beam splitter.

When the laser spot is focused onto a solid or liquid sample, the property of the beam, such the penetration depth and its shape, strictly depends by the refractive index and the absorption characteristics of the material. Hence, the Raman scattering will occur within this so-called probe volume and detected with different intensity along the beam length and across the focal plane. Therefore, the spectrum measured from a point on the surface of the sample will carry with it the information, sometimes undesired, from the crystallographic planes below the surface. However, the T64000 Raman spectrometer is equipped with a set of cross-slit, which allow the modulation of the Raman probe and hence work in confocal mode, thus excluding those information from the region out-of-focus. The confocal microscopy is a well-known technique commonly employed in the Raman spectroscopy and in other imaging microscopy [206]. As depicted in Figure 61, through two filtering pinhole, one placed on the laser beam path (enhancing the Gaussian shape of the probe) and the other one located in the exit focal plane of the microscope (improving both lateral and axial space resolution), it is possible to exclude the light originating from the out-of-focus planes. The signal from the surface is brought to a focus at the aperture and passes without significant attenuation. On the other hand, out-of-focus light from below the surface is brought to a focus before the aperture and is thereby cut off.
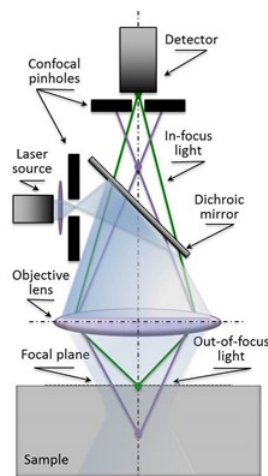
Figure 61: Schematic draft of the confocal configuration

8.2 X-RAY photoelectron spectroscopy

8.2.1 Introduction to X-ray photoelectron spectroscopy

X-ray photoelectron spectroscopy (XPS), also known as electron spectroscopy for chemical analysis (ESCA), represents the most used among the electron spectroscopies, both in academic or industrial settings, for defining the elemental composition and/or speciation of the outer 1–10 nm of any solid substrate [207]. In fact, together with Auger-electron spectroscopy (AES) it represents a powerful research tool for surface chemical analysis [208], allowing studying physical and chemical phenomena occurring at the surface of various materials (ranging from metals, oxides, semiconductors ceramics, polymers and biomaterials).

The photoelectric effect was firstly discovered by Heinrich Rudolf Hertz, in 1887, but the phenomena was later explained by Albert Einstein, in 1905. In 1907, P.D. Innes managed to record broad bands of emitted electrons as a function of velocity, in effect recording the first XPS spectrum. Other researchers, including Henry Moseley, Rawlinson and Robinson, independently performed various experiments. In the 1950s Kai Siegbahn and his research group in Uppsala (Sweden) developed several significant improvements in the equipment, and in 1954 recorded the first high-energy-resolution XPS spectrum, revealing the potential of XPS [209]. In 1969, a small group of engineers, in cooperation with Siegbahn, produced the first commercial monochromatic XPS instrument. Siegbahn received then the Nobel Prize for Physics in 1981 [210].

The popularity of XPS stems from its abilities and attributes such as:
(a) identification and quantification of the elemental composition of any solid surface with all elements from Li–U detectable;
(b) revelation of the chemical environment where the respective element exists in;
(c) sensitivity (concentrations down to 0.1 atomic %);
(d) surface specificity (less than 10 nm):
(e) ease of analysis (minimal sample preparation is required) [207].

8.2.2 Physical basis of XPS

XPS works on the principle of photoelectric effect, in which soft X-rays are used as exciting photon source. An X-ray photon interacts with a core level electron transferring its photon energy and causing electron emission by the photoelectric effect, as illustrated in Figure 62. Electrons reaching the surface are emitted in the vacuum.
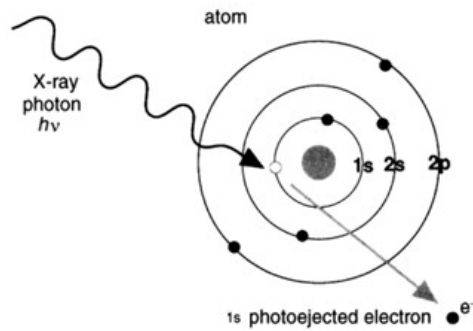
Figure 62: Photoemission process

Photoelectron production is a single step process in which an electron initially bound to an atom/ion is ejected by a photon. Since photons are a massless (zero rest mass), chargeless packages of energy, these are annihilated during photon–electron interaction with complete energy transfer occurring. If this energy is sufficient, it will result in the emission of the electron from the atom/ion. The kinetic energy (E_k) that remains on the emitted electron is the quantity measured. This is useful since this is of a discrete nature and is a function of the electron binding energy (E_b), which, in turn, is element and environment specific [207].

Since the X-ray energy with a particular wavelength is known, and because the emitted electrons' kinetic energies can be experimentally measured, the electron binding energy of each of the emitted electrons is given by the following equation, based on the work of Ernest Rutherford (1914):

$$E_b = h\nu - (E_k + \phi) \qquad\qquad (XIX)$$

where E_b is the binding energy (BE) of the emitted electron, $h\nu$ is the energy of the X-ray photons being used, E_k is the kinetic energy of the electron as measured by the instrument and ϕ is the instrument's spectrometer work function (Figure 63). This equation is essentially a conservation of energy equation. The work function term ϕ is an adjustable instrumental correction factor that accounts for the few eV of kinetic energy given up by the photoelectron as it becomes absorbed by the instrument's detector. It is a constant that rarely needs to be adjusted in practice.
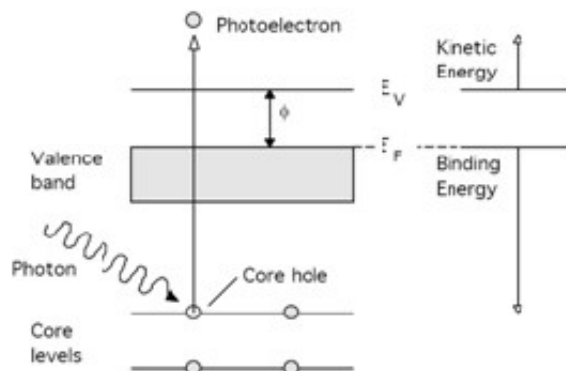
Since the binding energy of an electron in a particular shell of the atom is unique to each element, elements on the surface of the material, except for Hydrogen (H) and Helium (He), can be identified and the material relative composition can be determined. XPS spectral lines are identified by the core shell (1s, 2s, 2p, 3s, 3p, 3d, etc.) from which the electron was emitted [180]. Therefore, the measured photoelectron spectrum is a direct indication of the binding energies of the different atomic electron levels and is often directly calibrated in eV of binding energy: The lower the kinetic energy, the higher the binding energy.

XPS spectra are usually given by intensity (counts per second, Y-axis) as a function of the binding energy (X-axis). Because binding energy and kinetic energy have a different sign, the binding energy scale is plotted with increasing energy from right to left. Besides photoelectron core level and valence band peaks, spectra contain also Auger electron peaks (X-ray induced Auger electron spectra, often called XAES) and may further contain satellite peaks and energy loss peaks. In fact, using X-ray sources without monochromator, the main peak $K_{\alpha 1,2}$ is accompanied by satellite peaks caused by X-ray lines such as $K_{\alpha 3,4}$ (Figure 64). This family of minor peaks is characterized by intensity and spacing specific of the anode material [211].
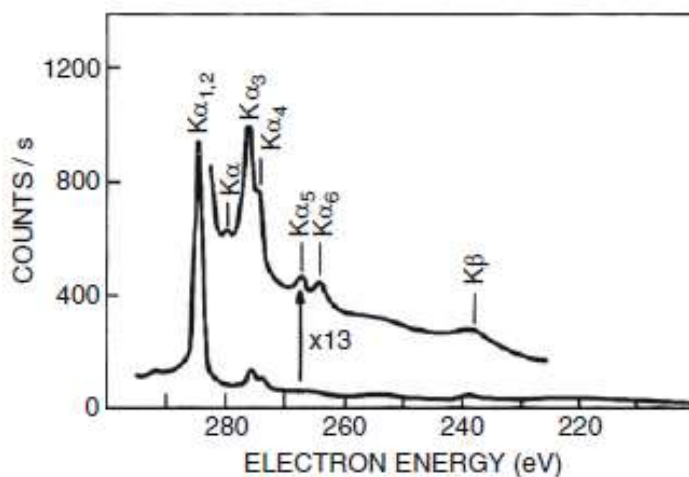
Figure 64: Satellite peaks ($K_{\alpha 3,4,5,6}$) of Al K radiation source without monochromator

In addition to the photoelectrons, Auger electrons are emitted due to relaxation of the energetic ions left after photoemission (Figure 65), approximately 10^{-14} seconds after the photoelectric event. In Auger process, an outer electron falls into the inner orbital vacancy and a second electron is emitted, carrying off the excessive energy, in order to conserve energy released in the previous step. Auger emission is independent of the photon energy and therefore of the X-ray source [212]. Thus, photoionization normally leads to two emitted electrons: a photoelectron and an Auger electron, with energies that cannot exceed the energy of the ionizing photon.
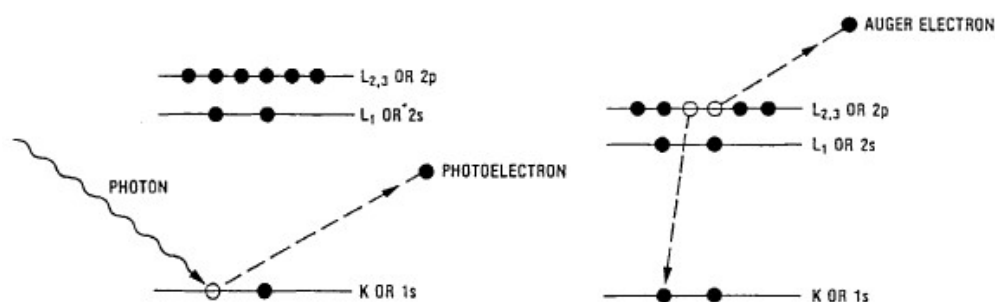
Figure 65: Comparison between photoelectric process (left) and Auger process (right).

Any change in the bonding state of an atom gives rise to changes in the observed spectral characteristics: binding energy, peak width and shape and valence band changes. In fact, chemical bonding in a compound usually causes a change of the binding energy as compared to bonding in the pure element, which is called "chemical shift" and can be explained by the effective charge potential change on an atom [213].

Usually the line shape of an XPS peak is represented by a combination of Gaussian and Lorentzian functions, or, physically more correct, using a convolution of a Lorentzian with a Gaussian (Voigt function) [214]. Empirical tail functions can be added to take care of asymmetric lines. Photoelectron spectra of the elements are compiled in handbooks, generally provided by the instrument manufacturers and in Internet databases.

The natural line width ΔE_0 is determined by the lifetime of the core hole state left by photoemission (lifetime broadening) and can be estimated by the uncertainty principle as:

$$\Delta E_0 = \frac{h}{\tau} = \frac{4.1 \times 10^{-15}}{\tau} \tag{XX}$$

where h is the Planck constant in eV s and τ is the lifetime in seconds [215].

8.2.3 XPS instrumentation

As illustrated in Figure 66, an XPS instrument primarily consists of an X-ray source, extraction optics, energy filters and a detection system.

Sources used in XPS must be able to produce photons of a sufficient energy to access a suitable number of core electron levels. Photons of this energy lie within the X-ray region of the electromagnetic spectrum. X-rays used in commercially available XPS instruments can be produced by X-ray tubes, depending on the different geometry are referred to as monochromatic sources or standard sources, and by synchrotron sources.
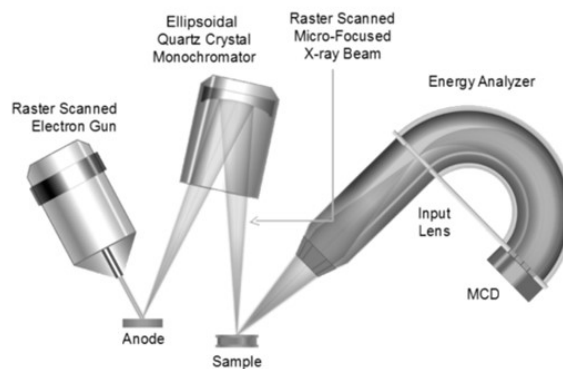
Figure 66: Draft of XPS instrumentation

X-ray tubes produce X-rays by directing a sufficiently energetic electron beam at some metallic solid. This metallic object is referred to as the X-ray anode, with the electron source being the cathode. Although any solid can in principle be used as an X-ray anode, Mg and Al have become the most commonly used in XPS. The characteristic Mg K_α radiation at 1253.6 eV and the Al K_α radiation at 1486.6 eV possess sufficiently high energies for core level excitation. This popularity stems from relatively high energy and intensity of $K\alpha$ X-rays, minimal energy spread and ease of manufacture and use of such anodes.

Standard sources essentially consist of a water-cooled anode that attracts negative charge and faces the target (sample). Irradiation of this anode with energetic electrons then results in an unfocused X-ray beam that floods the entire sample. Standard sources, if compared to monochromatic sources, are less expensive, have no limits in the selection of the anode material and allow switching between anode materials (typically Al and Mg). On the contrary, disadvantages include a larger energy spread (when using Al and Mg anodes, both the $K_{\alpha 1}$ and $K_{\alpha 2}$ lines overlap, producing a single peak of larger full width at half maxima (FWHM)), the presence of additional satellite peaks and their lower photon flux per unit area (due to the unfocused nature of these sources).

Monochromatic sources consist of the elements found in a standard source but the X-rays are reflected off a concave single crystal as illustrated in Figure 67.
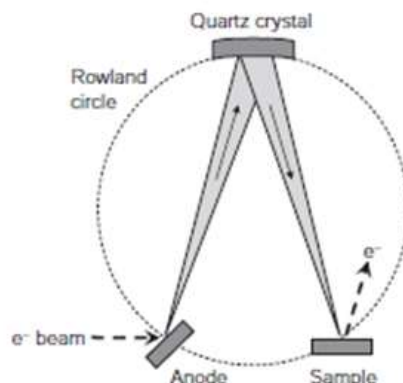
Figure 67: Schematic of a monochromatic source geometry: only X-rays with specific wavelength will reflect off a crystal at some specific angle defined by the crystal lattice spacing

The Bragg diffraction criteria (1913) stipulates that photons can only be reflected constructively if:

$$n\lambda = 2d\sin\phi \qquad\qquad (XXI)$$

where n is the diffraction order, λ is the wavelength, d is the crystal atomic spacing, and ϕ is the angle of diffraction. Since λ, and hence the energy, of the $K_{\alpha 1}$ and $K_{\alpha 2}$ X-rays is different, the latter is filtered out. This, combined with the concavity introduced into the crystal, results in a focused X-ray beam at the sample surface with the narrower energy spread obtainable with a standard source (Figure 68).
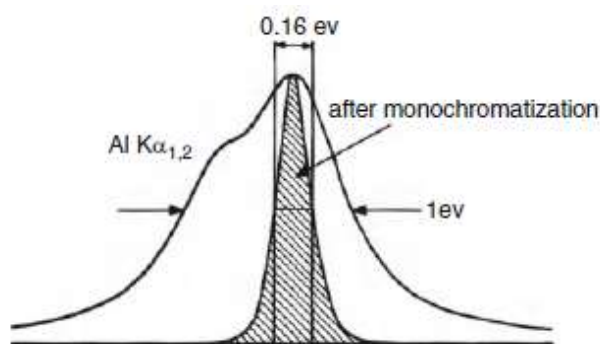
Figure 68: Effect of a monochromator crystal on the Al $K_{\alpha 1,2}$ radiatio*n*

The main advantage of these sources when compared to standard sources lies in a focused X-ray beam and the narrower energy spread of the resulting X-rays, while primary disadvantages include their higher cost and the limited number of anodes allowable within a specific geometry.
X-rays of narrower energy spread than this can only be produced in synchrotrons.

Since information in XPS is derived from the kinetic energy of the electron emissions, effective analysis requires an energy filter with both a high-energy resolution and a high transmission. The former allows for the separation of closely spaced peaks, optimizing speciation identification, while the latter allows maximum sensitivity. The two primary energy filter configurations used in XPS include Cylindrical Mirror Analyzer (CMA) and concentric Hemispherical Analyzer (CHA). These are by far the most commonly used in modern dedicated XPS instruments.

In XPS, it is not only important to measure the energy of the electron emissions but also the number of electrons produced. Indeed, XPS spectra are plotted in units of energy versus intensity, with the energy defined by the energy analyzer used and the intensity defined by the number of electrons recorded by the detector. To obtain the best possible sensitivity, the detector must be capable of recording individual electrons, that is, operating in pulse counting mode. This signal is recorded in units of current (A), which are then represented in units of counts per second [207].

In addition, XPS instrumentation is equipped with an ultrahigh vacuum (UHV)-based stainless steel chamber that contains the sample stage, electron energy analyzer and detection system, an X-ray source (with or without monochromator) and an ion gun for sample cleaning and for depth profiling. Outside the UHV system are consoles

with the electronics supply systems and the computer with the data acquisition and processing software [215].

Sample preparation and mounting are not critical. The sample can be mechanically attached to the specimen mount, as received. Ordinarily volatile materials are removed from the surface by long-term pumping in a separate vacuum system or by washing with a suitable solvent sufficiently volatile. Ion sputter-etching or other erosion techniques can also be used to remove surface contaminants. Argon ion etching is commonly used for this purpose and for in depth analysis. It must be noted, however, that these methods for surface removal are likely to change the chemical nature of the surface [211].

All the experimental XPS data reported in this thesis were obtained using a JPS-9010 MC photoelectron spectrometer (JEOL Ltd., Tokyo, Japan) with a X-ray source of monochromatic MgK_α (output 10 kV, 10 mA).

8.3 Cathodoluminescence Spectroscopy

8.3.1 Introduction to Cathodoluminescence Spectroscopy

In general, luminescence is a common process in solid materials, in which a photon is emitted due to a photo-emissive electron transition from an excited electronic state to a state with lower energy, after the absorption of energy by the considered system. The spectroscopic information carried by the emitted photons strictly depends both on the excitation method (hence the source of energy), and on the mechanism of the process on which the radiation is generated (the type of the luminescent system). As shown in Table 10, several types of luminescence can be distinguished according to the excitation mechanism:

Name	Excitation mechanism
Photoluminescence	Light
Cathodoluminescence	Electrons
Radioluminescence	X-ray, α-ray, β-ray or γ-ray
Thermoluminescence	Heating
Electroluminescence	Electric field or current
Triboluminescence	Mechanical energy
Sonoluminescence	Sound waves in liquids
Chemiluminescence	Chemical reaction

Table 10: classification of different types of luminescence

The term cathodoluminescence (CL) indicates the general phenomena of the light emitted from a solid sample as a result of electron beam (cathode-ray) irradiation.

This phenomenon was observed for the first time in the middle of the 19th century during experiments of electrical discharges in evacuated glass tubes, which showed luminescence when the cathode ray hits the glass. It is worth to note that the observation of this phenomenon led Thompson, to discover the electron particle. Some years later Sir William Crooks, started to investigate in detail the luminescence emission from the cathode ray tube and a possible application in spectroscopy [216]. However, systematic observations of the luminescence induced by electron as a spectroscopic tool (as all the general luminescence) were not made until the middle sixties by Smith and Stenstrom [217]. The biggest improvement to this spectroscopic technique occurred with the development and the improvement of the scanning electron microscopy (SEM). Initial study about the possibility of the utilization of this equipment for CL measurement was made first by Krinsley and Hyde in 1971 [218]. Today, CL devices are normally commercialized by the same companies that produce the SEM instrumentation in a coupled CL-SEM apparatus.

8.3.2 Luminescence in band-gap materials

In general, the mechanism of luminescence could be described in terms of three fundamental processes: the absorption of excitation energy and stimulation of the system into an excited state, the transformation and/or transfer of the excitation energy, and the emission of photon and relaxation of the system to a non-excited state [219].

After the absorption of energy by the system, the electron could pass from the ground state level to an excited state, and return to the ground state level through radiative or non-radiative transitions. In the first case, the wavelength of emitted photons usually depends on the energy difference between the excited and the ground levels, in the second the absorbed energy can be dissipated as a result from interaction with the lattice or a through transfer of energy to other ions.

In band-gap materials (such as insulators or semiconductors) the valence band E_v, i.e. the last band filled by electrons, is detached by the conduction band E_c the next empty band, by an energy gap (Figure 69 a). If enough energy is provided the excitation process induces an electron to move from the valence band to the conduction band, with the generation of a hole (Figure 69 b). These holes can be visualized as positive charges with the same mass of electrons indicated before. Those promoted electrons, remain only a very short time in the conduction band, before losing energy and returning to the valence band [220]. When the energetic electrons attempt to return to the ground state valence band, they can fall directly back to the valence band, generally emitting UV radiation, or they may be temporarily trapped (on the scale of microseconds) by intrinsic (structural defects) and/or extrinsic (impurities) traps (Figure 69 c). If the energy, lost when the electrons vacate the traps, is emitted is in the appropriate energy/wavelength range, luminescence will result [221]. There are several possible ways in which the traps can interact to produce luminescence. From that trap, the electron might return to the ground state or it may

encounter multiple traps emitting photons with wavelengths dependent on the energy differences. The intensity of the CL is generally a function of the density of the traps. The time these electrons remain in the traps is quite variable producing photons with energies in the near-UV and visible portions of the electromagnetic spectrum the moment they leave the traps [222].
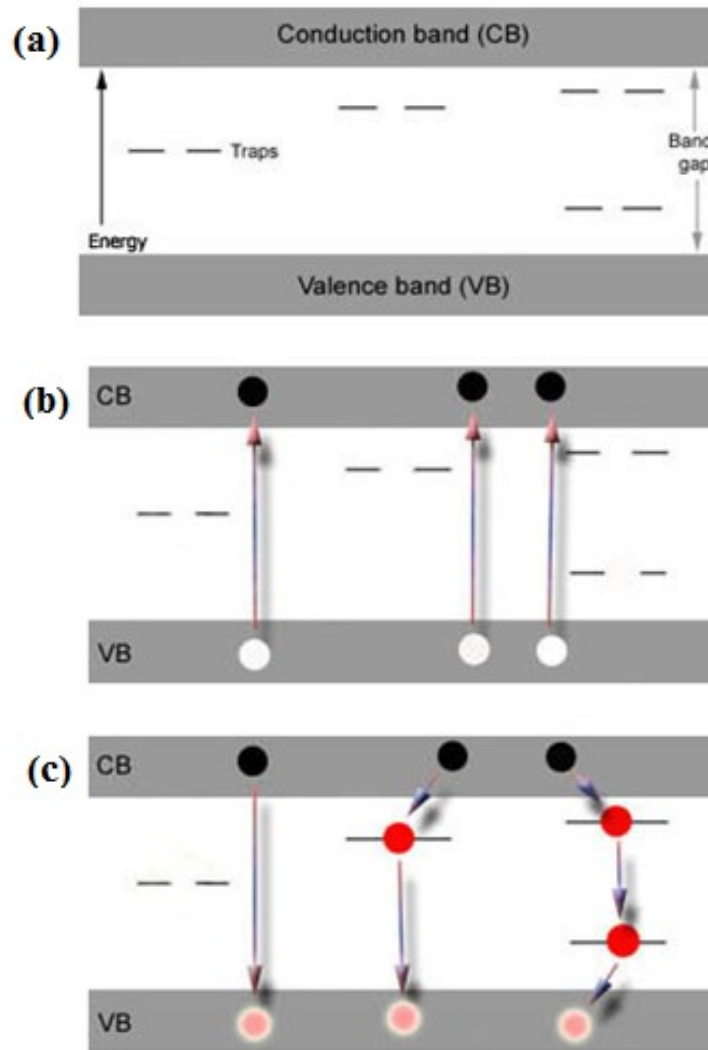
Figure 69: Generation of CL response in an insulator, as conceptualized with band theory

It is possible to distinguish the luminescence transition between "intrinsic" or fundamental emission, and "extrinsic" or activated emission [219]. **Intrinsic luminescence** is characteristic of the host lattice. It can be due to non-stoichiometry (vacancies), structural imperfections (poor ordering in the crystal, radiation damage, shock damage, etc.) and impurities (non-activators that distort the lattice). **Extrinsic luminescence** results from impurity atoms or defects in the structure. These impurities (generally called activators) generate luminescent centres and are most commonly transition elements, rare earth elements and actinide elements.

Photon emission is only possible if the gap next to the lower level is larger than some critical values. In fact in the case of a series of closely spaced traps at successively

lower energy levels, a promoted electron can cause a non-radiatively cascade (phonon emission) from one energy level to another reaching the ground state without any emission of photons [223].

8.3.3 Cathodoluminescence Instrumentation

The essential requirements of CL detection system designs are a high efficiency of light collection, transmission, and detection [224].

The luminescence signal, induced by electron irradiation, can be collected by means of additional equipment attached to the SEM, as shown in Figure 70 (a). This SEM-CL apparatus is composed by a SEM microscope equipped with optical devices that enables direct light collection from the specimen during the electronic bombardment.
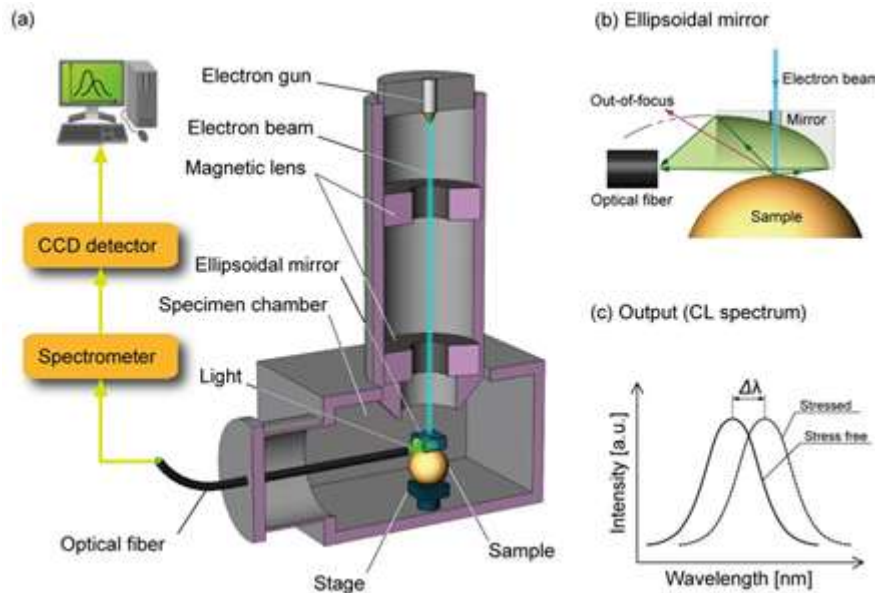
Figure 70: Schematic drafts of: (a) the cathodoluminescence device attached to an SEM; (b) an electron beam impinging on the sample that in turn emits a characteristic light collected by an ellipsoidal mirror and sent to the spectrometer; and, (c) example of an output spectrum recorded by the cathodoluminescence device

For this purpose, usually a parabolic or ellipsoidal mirror (Figure 70 (b)) is placed at a short distance above the sample surface. The mirror is not fixed and can be moved through a set of mechanical manipulators that allow the adjustment of the mirror position.

The penetration depth of electrons, and accordingly the excitation depth, depends on the energy of the impinging electron beam; therefore, using low acceleration voltages, the probing depth can be confined to the nanometer range, thus obtaining a spatial resolution several orders of magnitude higher as compared to laser probes [225]. CL equipment attached to an SEM offers advantages over conventional laser spectroscopy, the main advantage being the larger spatial resolution in the nanometer range.

The electron beam is properly focused on the sample surface with an electromagnetic lens, passes through an aperture on the mirror and impacts the surface. The light generated from the sample, which is placed at the focus point of the mirror (typically 1 mm or less below the mirror itself), is reflected to a detector, a CCD that allows the simultaneous collection of the entire range of wavelength (from about 300 to about 800 nm) [5].

The cathodoluminescence measurements were performed by a field-emission scanning electron microscope (FEG-SEM) with a Schottky-emission type gun (SE-4300, Hitachi Co., Tokyo, Japan) as the excitation source (Ceramic Physics Laboratory of Department of Materials Science and Engineering, Kyoto Institute of Technology). The FEG-SEM was mounted on an optical table, which aiding the optical alignment and reducing the vibration. A high-sensitivity CL detector unit (Horiba MP-32FE) was employed for the collection of light upon reflection into an ellipsoidal mirror and transmission through an optical fibre. The spectrum of the emitted light (Figure 49 (c)) was analysed using a high-resolution monochromator (Triax 320, Jobin-Yvon, Horiba Group, Tokyo, Japan), equipped with a char ge-coupled device (CCD) camera.

Bibliography

[1] Notiziario dell'Istituto superiore di Sanità, **18** [12], (2005)

[2] Rapporto ISTISAN 9/22

[3] U. Holzwarth, G. Cotogno, "Total Hip Arthroplasty-State of the Art, Challenges and Prospects", *JRC Scientific and Policy Reports*, European Commission (2012)

[4] S. Affatato, "Perspectives in Total Hip Arthroplasty", Woodhead Publishing, Kidlington, (2014)

[5] G. Pezzotti, "Advanced materials for joint implants", Pan Stanford Publishing, Singapore, (2013)

[6] M. M. Groh, J. Herrera, "A comprehensive review of hip labral tears", *Curr. Rev. Musculoskelet. Med.*, **2**, 105-117, (2009)

[7] J. C. Thompson, "Netter's Concise Atlas of Orthopaedic Anatomy", Elsevier Saunders, Philadelphia, (2002)

[8] J. A. Ralphs, M. Benjamin, "The joint capsule: structure, composition, aging and disease", *J. Anat.*, **184**, 503-509, (1994)

[9] N. Pastalanga, R. Soames, "Anatomy and human movement", Churchill Livingstone, Edinburgh, (2007)

[10] S. T. Channel, J. H. Beaty, "Campbell's Operative Orthopaedics", Mosby Elsevier, Philadelphia, (2007)

[11] J. Kelsey, "The Epidemiology of diseases of the Hip: A review of the literature", *The International Journal of Epidemiology*, **6**, 269-280, 1977

[12] Australian Orthopaedic Association National Joint Replacement Registry, Annual Report, Adelaide, (2015)

[13] Z. Jotanovic, R. Mihelic, G. Gulan, B. Sestan, Z. Dembic, "Osteoarthritis of the hip: An overview", *Periodicum Biologorum*, **117**, 95-108, (2015)

[14] N. Arden, F. Blanco, C. Cooper, A. Guermazi, D. Hayashi, D. Hunter, K. M. Javaid, F. Rannou, F. W. Roemer, J. Y. Reginster, "Atlas of Osteoarthritis", Springer Healthcare Communications, (2015)

[15] D. T, Felson, Y. Zhang, "An update on the epidemiology of knee and hip osteoarthritis with a view to prevention", *Arthritis & reumatism*, **41** [8], 1343-1355 (1998)

[16] D. J. Hunter, D.T. Felson, "Osteoarthritis", *British Medical Journal*, **332**, 639-42, (2006)

[17] Jr. Harris, "Rheumatoid arthritis: pathophysiology and implications for therapy", *N. Engl. J. Med.*, **322**, 1277-89, (1990)

[18] W. Katchamart, S. Johnson, HL Lin, V. Phumethum, C. Salliot, Bombardier C., "Predictors for Remission in Rheumatoid Arthritis Patients: A Systematic Review", *Arthritis Care & Research*, **62** [8], 1128 -1143, (2010)

[19] H. D. Van Tuyl, D. T. Felson, G. Wells, J. Smolen, B. Zhang, M. Boers, "Evidence for Predictive Validity of Remission on Long-Term Outcomes in Rheumatoid Arthritis: A Systematic Review", *Arthritis Care & Research*, **62** [1], 108 -117 (2010)

[20] D. Tönnis, "Congenital Dysplasia and Dislocation of the Hip in Children and Adults", Springer Berlin Heidelberg, (1987)

[21] R. Gul, J.C. Coffey, G Khayyat, A. J, McGuinness, "Late presentation of developmental dysplasia of the hip", *Irish Journal of Medical Science*, **171** [3], 139-140, (2002)

[22] J. J. McCarthy, P. V. Scoles, G. D.MacEwen, "Developmental dysplasia of the hip (DDH)", *Current Orthopaedics*, **19**, 223-230, (2005)

[23] H. Kim K., "Pathophysiology and new strategies for the treatment of Legg-Calve-Perthes disease", *American Journal of Bone and Joint Surgery*, **94** [7], 659-697, (2012)

[24] T. R. Yochum, L. J. Rowe, "Essentials of Skeletal Radiology", LWW, (1987)

[25] J. S. Siopack, H. E. Jergesen, "Total Hip Arthroplasty", *West J. Med.*, **162** [3], 243-249, (1995)

[26] R. Huiskes, H. Weinans, B. Van Rietbergen, "The Relationship Between Stress Shielding and Bone Resorption Around Total Hip Stems and the Effects of Flexible Materials", *Clinical Orthopaedics and Related Research*, **274**, 124-34, (1992)

[27] R. A. Brand, J. J, Callaghan, R. C. Johnston, "Total hip reconstruction", *Iowa Orthop. J.*, **11**, 19-42, (1991)

[28] M. Ikeda, S. Y. Komatsu, I. Sowa, M. Niinomi, "Aging behavior of the Ti-29Nb-13Ta-4.6Zr new alloy for medical implants", *Metall. Mater. Trans.*, **33**, 487-493, (2002)

[29] M. Niinomi, "Recent research and development in the titanium alloys for biomedical applications and healthcare goods", *Adv. Mater. Sci. Technol.*, **4**, 445-454, (2003)

[30] H. Bougherara, M. Bureau, M. Campbell, A. Vadean, L. Yahia, "Design of a biomimetic polymer-composite hip prosthesis", *A. J. Biomed. Mater. Res.*, **82** [1], 27-40, (2007)

[31] I. Kostensalo, M. Junnila, P. Virolainen, V. Remes, M. Matilainen, T. Vahlberg, P. Pulkkinen, A. Eskelinen, K. Mäkelä, "Effect of femoral head size on risk of revision for dislocation after total hip arthroplasty", *Acta orthopaedic,* **84** [4], 342-347, (2013)

[32] W. K. Barsoum, R. W. Patterson, C. Higuera, A. K. Klika, V. E. Krebs, R. Molloy, "A computer model of the position of the combined component in the prevention of impingement in total hip replacement", *Br. J. Bone Joint. Surg.*, **89**, 839-845, (2007)

[33] Pedersen DR, Callaghan JJ, Brown TD. Activity-dependence of the "safe zone" for impingement versus dislocation avoidance. Med Eng Phys 2005. 27: 323-328

[34] F. J. Kummer, S. Shah, S. Iyer, P. E. DiCesare, "The Effect of Acetabular Cup Orientations on Limiting Hip Rotation", *The Journal of Arthroplasty*, **14** [4], (1999)

[35] B. Espehaug, O. Furnes, L. I. Havelin, L. B. Engesaeter, S. E. Vollset, "The type of cement and failure of total hip replacements", *Br. J. Bone Joint Surg.*, **84** [6], 832-8, (2002)

[36] R. D. Mulroy, W. H. Harris, "The effect of improved cementing techniques on component loosening in total hip replacement. An 11-year radiographic review", *Br. J. Bone Joint Surg.*, **72** [5], 757-60, (1990)

[37] D. K. Collis, C. G. Mohler, "Comparison of clinical outcomes in total hip arthroplasty using rough and polished cemented stems with essentially the same geometry", *Am. J. Bone Joint Surg.*, **84**, 586-92, (2002)

[38] L. C. Jones, D. S. Hungerford, "Cement disease", *Clin. Orthop. Relat. Res.*, **225**, 192-206, (1997)

[39] C. J. Della Valle, R. A. Berger, S. Shott, A. G. Rosenberg, J. J. Jacobs, L. Quigley et al., "Primary total hip arthroplasty with a porous-coated acetabular component. A concise follow-up of a previous report", *Am. J. Bone Joint Surg.*, **86** [6], 1217-22, (2004)

[40] K. Y. Kim, "Long-term results of the cementless porous-coated anatomic total hip prosthesis", *Br. J. Bone Joint Surg.*, **87** [5], 623-7, (2005)

[41] M. I. Parker, G. Pryor, K. Gurusamy, "Cemented versus uncemented hemiarthroplasty for intracapsular hip fractures: A randomized controlled trial in 400 patients", *Br. J. Bone Joint Surg.*, **92**, 116-22, (2010)

[42] D. F. Williams, "The Williams dictionary of biomaterials", Liverpool University Press, Liverpool, (1999)

[43] S. Greenwald, J. P. Garino, "Alternative bearing surfaces: the Good, the Bad, and the Ugly", *The Journal of Bone and Joint Surgery*, **83-A** [2], 68-72, (2001)

[44] A. Buford, T. Goswami, "Overview of Metal-on-Polyethylene, Metal- on-Metal and Ceramic Hip Wear Mechanisms", *Prosthetic Hip Wear Mechanisms*, **15**, (2004)

[45] M. Semlitsch, H. G. Willert., "Clinical wear behaviour of ultra-high molecular weight polyethylene cups paired with metal and ceramic ball heads in comparison to metal-on-metal pairings of hip joint replacements", *Proceedings of the Institution of Mechanical Engineers, Part H: Journal of Engineering in Medicine,* **211** [1], 73-88, (1997)

[46] A. H. Hosman, H. C. Mei, S. K. Bulstra, H. J. Busscher, D. Neut, "Effects of metal-on-metal wear on the host immune system and infection in hip arthroplasty", *Acta Orthopaedics,* **81** [5], 526-534, (2010)

[47] M. Topolovec, A. Cor, I. Milosev, Metal-on-metal vs. Metal-onpolyethylene total hip arthroplasty tribological evaluation of retried components and periprosthetic tissue, the Journal of the mechanical behavior of biomedical materials, 34 (2014) 243-252

[48] G. M. Keegan, D. I. Learmonth, C. P. Case, "Orthopaedic metals and Their potential toxicity in the patient arthroplasty", *The Journal of Bone and Joint Surgery*, **89-B** [5], 567-573, (2007)

[49] J. Lazennec, P. Boyer, J. Poupon, M. A. Rousseau, C. Roy, P. Ravaud, Y. Catonné, "Outcome and serum ion determination up to 11 years after implantation of a cemented metal-on-metal hip prosthesis", *Acta orthopaedica*, **80** [2], 168-173, (2009)

[50] P. A. Revell, "Joint replacement technology", Woodhead Publishing Limited Cambridge, (2008)

[51] D. Hannouche, A. Zaoui, F. Zadegan, L. Sedel, R. Nizard, "Thirty years of experience with alumina-on-alumina bearings in total hip arthroplasty", *International Orthopaedics*, **35** [2], 207-213, (2011)

[52] C. Esposito, W. L. Walter, P. Campbell, "Squeaking in metal-on-metal hip resurfacing arthroplasty", *Orthopedics and Related Clinical Research*, **468** [9], 2333-2339, (2010)

[53] D. Dowson, "A comparative study of the performance of metallic and ceramic femoral head components in total replacement hip joints", *Wear*, **190**, 171-183, (1995)

[54] Y. H. Kim, J. W. Park, S. S. Kulkarni, "A randomised prospective evaluation of ceramic-on-ceramic and ceramic-on-highly cross-linked polyethylene bearings in the same patients with primary cementless total hip arthroplasty", *International orthopaedics*, **37** [11], 2131-2137, (2013)

[55] A. A. Edidin, S. M. Kurtz, "The influence of mechanical behaviour on the wear of four clinically relevant polymeric biomaterials in a hip simulator", J. Arthroplasty, **15**, 321–31, (2000)

[56] S. M. Kurt, O. K. Muratoglu, M. Evans, A. A. Edidin, "Advances in the processing, sterilization, and crosslinking of ultra-high molecular weight polyethylene for total joint arthroplasty", *Biomaterials,* **20**, 1659–88, (1999)

[57] A. Bellare, H. Schnablegger, R. E. Cohen, "A small-angle x-ray scattering study of high-density polyethylene and ultra-high molecular weight polyethylene", *Macromolecules*, **17**, 2325–33, (1995)

[58] P. Sajkiewicz, T. Hashimoto, K. Saijo, A. Gradys, "Intermediate phase in poly(ethylene) as elucidated by the WAXS. Analysis of crystallization kinetics", *Polymer*, **46** [2], 513–521, (2005)

[59] G. R. Strobl, W. Hagedorn, "Raman spectroscopic method for determining the crystallinity of polyethylene", *Journal of Polymer Science, Polymer Physics Edition*, **16** [7], 1181–1193, (1978)

[60] P. J. Veld, M. Hütter, G. C. Rutledge, "Temperature-dependent thermal and elastic properties of the interlamellar phase of semicrystalline polyethylene by molecular simulation", *Macromolecules*, **39** [1], 439–447, (2006)

[61] S. Pramanik, A. K. Argawal, K. N. Rai, "Chronology of total hip joint replacement and materials development", *Trends Biomater Artif Organs* , **19** [1], 15– 26, (2005)

[62] P. Eyerer, R. Ellwanger, H. A. Federolf, M. Kurth, H. Madler, "Polyethylene. In: Concise encyclopaedia of medical and dental materials". D. Williams, Cahn R, editors, The MIT Press, Massachusetts, (1990)

[63] P. Eyerer, A. Frank, R. Jin, "Characterization of ultrahigh molecular weight polyethylene (UHMWPE): extraction and viscometry of UHMWPE", *Plastverarbeiter,* **36**, 46–54, (1985)

[64] K. S. Han, J. F. Wallace, R. W. Truss, P. H. Geil, "Powder compaction, sintering, and rolling of ultra-high molecular weight polyethylene and its composites", *J. Macromol. Sci-Phys.*, **19**, 313–49, (1981)

[65] R. Gul, "Improved UHMWPE for use in total joint replacement", Ph.D. Dissertation, Massachusetts Institute of Technology, Boston, (1997)

[66] A. Barnetson, P. R. Hornsby, "Observations on the sintering of ultrahigh molecular weight polyethylene (UHMWPE) powders", *J. Materials Sci. Letters,* **14**, 80–4, (1995)

[67] A. V. Shenoy, D. R. Saini, "Compression moulding of ultra-high molecular weight polyethylene", *Plast. Rubber Proc. Appl.,* **5**, 313–17, (1985)

[68] A. Bellare, R. E. Cohen, "Morphology of rod stock and compression moulded sheets of ultra-high- molecular-weight polyethylene used in orthopaedic implants", *Biomaterials*, **17**, 2325–33, (1996)

[69] L. Pruitt, L. Bailey, "Factors affecting the near-threshold fatigue behaviour of surgical grade ultra-high molecular weight polyethylene", *Polymer*, **39**, 1545–53, (1998)

[70] S. M. Kurtz, J. Turner, M. Herr, A. A. Edidin, "Deconvolution of surface topology for quantification of initial wear in highly crosslinked acetabular components for THA", J. Biomed. Mater. Res., **63** [5], 492-500, (2002)

[71] J. Song, P. Liu, M. Cremens, P. Bonutti, "Effects of machining on tribological behavior of ultra-high molecular weight polyethylene (UHMWPE) under dry reciprocating sliding", *Wear*, **225**, 716-723, (1999)

[72] M. S. Jahan, C. Wang, "Combined chemical and mechanical effects on free radicals in UHMWPE joints during implantation", *J. Biomed. Mater. Res.*, **25**, 1005–17, (1991)

[73] C. M. Rimnac, R. W. Klein, F. Betts, T. M. Wright, "Post-irradiation aging of ultra-high molecular weight polyethylene", *J. Bone Joint Surg.*, **76A** [7], 1052–6, (1994)

[74] L. C. Sutula, J. P. Collier, K. A. Saum, B. H. Currier, J. H. Currier, W. M. Sanford, "Impact of gamma sterilization on clinical performance of polyethylene in the hip", *Clin. Orthop.*, **319**, 28–40, (1995)

[75] W. L. Sauer, K. D. Weaver, N. B. Beals, "Fatigue performance of ultra-high-molecular-weight polyethylene: effect of gamma radiation sterilization", *Biomaterials*, **17** [20], 1929-1935, (1996)

[76] S. M. Kurtz, W. J. Hozack, J. J. Purtill, M. Marcolongo, M. J. Kraay, V. M. Goldberg, "Significance of in vivo degradation for polyethylene in total hip arthroplasty", *Clin. Orthop. Relat. Res.*, **453**, 47–57, (2006)

[77] M. D. Ries, K. Weaver, N. Beals, "Safety and efficacy of ethylene oxide sterilized polyethylene in total knee arthroplasty", *Clin. Orthop.*, **331**, 159–63, (1996)

[78] J. P. Collier, L. C. Sutula, B. H. Currier, J. H. Currier, R. E. Wooding, I. R. Williams, "Overview of polyethylene as a bearing material: comparison of sterilization methods", *Clin. Orthop.*, **333**, 76–86, (1996)

[79] S. D. Bruck, E. P. Mueller, "Radiation sterilization of polymeric implant materials", *J. Biomed. Mater. Res.,* **22** [A2 Suppl], 133–44, (1988)

[80] M. S. Kyi, J. Holton, G. L. Ridgway, "Assessment of the efficacy of a low temperature hydrogen peroxide gas plasma sterilization system", *J. Hosp. Infect.,* **31**[4], 275–84, (1995)

[81] M. Goldman, L. Pruitt, "Comparison of the effects of gamma radiation and low temperature hydrogen peroxide gas plasma sterilization on the molecular structure, fatigue resistance, and wear behavior of UHMWPE", *J. Biomed. Mater. Res.,* **40** [3], 378–84, (1998)

[82] L. A. Feldman, H. K. Hui, "Compatibility of medical devices and materials with low-temperature hydrogen peroxide gas plasma", *Med. Dev. Diag. Indust.*, **19** [12], 57–62, (1997)

[83] H. A. McKellop, F. W. Shen, P. Campbell, T. Ota, "Effect of molecular weight, calcium stearate, and sterilization methods on the wear of ultra-high molecular weight polyethylene acetabular cups in a hip simulator", *J. Orthop. Res.*, **17** [3], 329–39, (1999)

[84] A. Wang, A. Essner, V. K. Polineni, C. Stark, J. H. Dumbleton, "Lubrication and wear of ultra-high molecular weight polyethylene in total joint replacements", *Tribol.*

Int., **31** [1–3], 17–33, (1998)

[85] R. H. Hopper, A. M. Young, K. F. Orishimo, C.A. Engh, "Effect of terminal sterilization with gas plasma or gamma radiation on wear of polyethylene liners", *Am. J. Bone Joint Surg.,* **85-A** [3], 464–8, (2003)

[86] R. D. Crowninshield, O. K. Muratoglu, "How have new sterilization techniques and new forms of polyethylene influenced wear in total joint replacement?", *J. Am. Acad. Orthop. Surg.,* **16** [Suppl 1], 80–5, (2008)

[87] J. J. Callaghan, J. M. Cuckler, J. I. Huddleston, J. O. Galante, "How have alternative bearings (such as metal-on-metal, highly cross-linked polyethylene, and ceramic-on-ceramic) affected the prevention and treatmentof osteolysis?", *J. Am. Acad. Orthop. Surg.,* **16** [Suppl 1], 33–8, (2008)

[88] O. K. Muratoglu, C. R. Bragdon, D. O. O'Connor, M. Jasty, W. H. Harris, "1999 HAP Paul Award. A novel method of crosslinking UHMWPE to improve wear, reduce oxidation and retain mechanical properties", *J. Arthroplasty,* **16** [2], 149–60, (2001)

[89] H. McKellop, F. W. Shen, B. Lu, P. Campbell, R. Salovey, "Development of an extremely wear resistant ultra-high molecular weight polyethylene for total hip replacements", *J. Orthop. Res.,* 17 [2], 157–67, (1999)

[90] S. M. Kurtz, C. Cooper, R. Siskey, N. Hubbard, "Effects of dose rate and thermal treatment on the physical and mechanical properties of highly crosslinked UHMWPE used in total joint replacements. Transactions of the 49th orthopedic research society", New Orleans, LA, (2003)

[91] S. M. Kurtz, M. Manley, A. Wang, S. Taylor, J. Dumbleton, "Comparison of the properties of annealed crosslinked (Crossfire) and conventional polyethylene as hip bearing materials", *Bull. Hosp. Jt. Dis.,* **61** [1-2], 17–26, (2002-2003)

[92] A. Wang, H. Zeng, S. S. Yau, A. Essner, M. Manley, J. H. Dumbleton, "Wear, oxidation, and mechanical properties of a sequentially irradiated andannealed UHMWPE in total joint replacement", *J. Phys. D. Appl. Phys.,* 39, 3213–19, (2006)

[93] J. H. Dumbleton, J. A. D'Antonio, M. T. Manley, W. N. Capello, A. Wang, "The basis for a second generation highly crosslinked UHMWPE", *Clin. Orthop. Relat. Res.,* **453**, 265–71, (2006)

[94] A. Wang, M. T. Manley, P. Serekian, "Wear and structural fatigue simulation of crosslinked ultra-high molecular weight polyethylene for hip and knee bearing applications: ASTM International STP 1445", (2003)

[95] V. S. Ivanov, Radiation chemistry of polymers. Utrecht, The Netherlands; (1992)

[96] F. W. Shen, H. A. McKellop, R. Salovey, "Irradiation of chemically crosslinked UHMWPE", *J. Poly. Sci. Poly. Phys.,* **34**, 1063–77, (1996)

[97] D. J. Carlsson, "Degradation and stabilisation of polymers subjected to high energy radiation", in Atmospheric oxidation and antioxidants, vol. II., Scott G. editor, Amsterdam, Elsevier, (1993)

[98] P. Bracco, V. Brunella, M. P. Luda, M. Zanetti, L. Costa, "Radiation-induced crosslinking of UHMWPE in the presence of co-agents: chemical and mechanical characterization", *Polymer,* **46**, 10648–57, (2005)

[99] S. J. Gencur, C.M. Rimnac, S.M. Kurtz, "Fatigue crack propagation resistance of

virgin and highly crosslinked, thermally treated ultra-high molecular weight polyethylene", *Biomaterials*, **27** [8], 1550–7, (2006)

[100] O. K. Muratoglu, C. R. Bragdon, D. O. O'Connor, M. Jasty, W. H. Harris, R. Gul, "Unified wear model for highly crosslinked ultrahigh molecular weight polyethylenes (UHMWPE)", *Biomaterials*, **20** [16], 1463–70, (1999)

[101] G. Scott, "Atmospheric Oxidation and Antioxidants", Elsevier Publishing Company, Amsterdam, (1965)

[102] J. L. Bolland, G. Gee, Trans. Farraday Soc., **42**, 236, (1946)

[103] L. Costa, M. P. Luda, L. Trossarelli, "UHMWPE.1. Meccano-oxidative degradation", *Polym. Degr. Stab.*, **55**, 329-338, (1997)

[104] L. Costa, I. Carpentieri, P. Bracco, "Post electron-beam irradiation oxidation of orthopaedic UHMWPE", *Polym. Degr. Stab.*, **93**, 1695–703, (2008)

[105] G. Ahlblad, PhD thesis "Imaging chemiluminescence Applied to Oxidation of Rubber Materials and Polyamide", Royal Institute of Technology, Stockholm, Sweden, (1998)

[106] N. C. Billingham, *Macromol. Chem.*, Macromol. Symp., **28**, 145, (1989)

[107] K. S. Katti , D. Verma , D. R. Katti, "Materials for joint replacement", *Joint Replacement Technology*, P. Revell (ed.), Cambridge , Woodhead Publishing Ltd., (2008)

[108] G. Griesmayr, M. Dietrich, J. Kasprowitsch, H. Dobbs, "Improvements in processing and manufacturing at CeramTec", H. Zippel and M. Dietrich editors, *Bioceramics in joint arthroplasty, 8th Biolox symposium proceedings*, Darmstadt: Steinkopff Verlag, 209–14, (2003)

[109] M. Morlock, R. Nassutt, M. A. Wimmer, E. Schneider, "Influence of resting periods on friction in artificial hip joint articulations", J. P. Garino and G. Willmann editors, *Bioceramics in joint arthroplasty, Proceedings of the 7th international BIOLOX symposium*. Stuttgart: Thieme, 6–20, (2002)

[110] D. G. Poitout (ed.), Biomechanics and Biomaterials in Orthopedics © Springer-Verlag London 2004

[111] H. Dobbs, "Quality improvement resulting from legal and regulatory developments", H. Zippel and M. Dietrich editors, *Bioceramics in joint arthroplasty, 8th Biolox symposium proceedings,* Darmstadt: Steinkopff Verlag, 205–8, (2003)

[112] P. Boutin, "Alumina and its use in surgery of the hip (Experimental study)", *Presse Med.,* **79** [14], 639–40, (1971)

[113] T. Shikata, H. Oonishi, Y. Hashimato, "Wear resistance of irradiated UHMW polyethylenes to Al_2O_3 ceramics in total hip prostheses", *Trans. of the 3rd Annual Meeting of the Soc for Biomater*, 118, (1977)

[114] M. Boehler, H. Plenk Jr., M. Salzer, "Alumina ceramic bearings for hip endoprostheses: the Austrian experiences", *Clin. Orthop.*, **379**, 85–93, (2000)

[115] P. Boutin, "Total arthroplasty of the hip by fritted aluminum prosthesis", "Experimental study and 1st clinical applications", *Rev. Chir. Orthop. Reparatrice Appar. Mot.*, **58** [3], 229–46, (1972)

[116] S. B. Bal, M. N. Rahaman, "Orthopedic applications of silicon nitride ceramics", *Acta biomaterialia*, **8** [8], 2889-2898, (2012)

[117] D. Hannouche, M. Hamadouche, R. Nizard, P. Bizot, A. Meunier, L. Sedel, "Ceramics in total hip replacement", *Clin Orthop Relat Res*, **430**, 62–71, (2005)

[118] D. Kluess, W. Mittlemeier, R. Bader, "Ceramics for joint replacement", *Joint Replacement Technology* , P. Revell (ed.), Cambridge , Woodhead Publishing Ltd, (2008)

[119] J. E. Ritter Jr., D. C. Greenspan, R. A. Palmer, "Use of Fracture Mechanics Theory in Lifetime Predictions for Alumina and Bioglass coated Alumina", *J. Biomed. Mater. Res.*, **13**, 251–263, (1979)

[120] G. Willmann, *Mater. wiss. Werkst. tech.*, **24**, 315 (1993)

[121] B. E. Bierbaum, J. Nairus, D. Kuesis, J. C. Morrison, D. Ward, "Ceramic-on-ceramic bearings in total hip arthroplasty", *Clin Orthop*, **405**, 158-63, (2002)

[122] B. Derbyshire, J. Fisher, D. Dowson, C. Hardaker, K. Brummitt, "Comparative study of the wear of UHMWPE with zirconia ceramic and stainless steel femoral heads in artificial hip joints", *Med. Eng. Phys.*, **16**, 229-36, (1994)

[123] T. Hopf, O. Sherr, B. Glöbel, C. Hopf, "Vergleichende tierexperimentelle Untersuchung zur gewebsveträglichkeit und messungen der radioaktiviät vershiedener rötgenkontrastmittel", *Z. Orthop.*, **127**, 620-4, (1989)

[124] B. Cales, "Zirconia as a sliding material: histologic, laboratory, and clinical data", *Clin. Orthop.,* **379**, 94–112, (2000)

[125] F. Komine, M. B. Blatz, H. Matsumura, "Correspondence to Current status of zirconia-based fixed restorations", *Journal of Oral Science*, **52** [4], 531-539, (2010)

[126] T. Yamamuro, "A new model of bone-conserving cementless hip prosthesis made of high -tech materials", S. Imura, M. Wada, H. Omori editors, "Joint arthroplasty", Tokyo: Springer Verlag, 213-24, (1990)

[127] B. M. Spector, M. D. Ries, R. B. Bourne, W. S. Sauer, M. Long, G. Hunter, "Wear performance of ultra-high molecular weight polyethylene on oxidized zirconium total knee femoral components", *Am. J. Bone Joint Surg.*, **83-A** [Suppl 2], 80–86, (2001)

[128] N. P. Sheth , P. Lemetowski , G. Hunter , J. P. Garino, "Clinical applications of oxidized zirconium", *J. Surg. Orthop. Adv.*, **17** [1], 17 – 26, (2008)

[129] P. Hernigou, G. Mathieu, A. Poignard, O. Manicom, P. Filippini, A. Demoura, "Oxinium, a new alternative femoral bearing surface option for hip replacement", *Eur. J. Orthop. Surg. Traumatol.*, **17**, 243–246, (2007)

[130] V. Good, M. Ries, R. L. Barrack, K. Widding, G. Hunter, D. Heuer, "Reduced wear with oxidized zirconium femoral heads", *Am. J. Bone Joint Surg.*, **85-A** [Suppl 4], 105–10, (2003)

[131] R. B. Bourne, R. Barrack, C. H. Rorabeck, A. Salehi, V. Good, "Arthroplasty options for the young patient: Oxinum on cross-linked polyethylene", *Clin. Orthop. Relat. Res.,* **441**, 159–67, (2005)

[132] D. P. Rhoads, K. C. Baker, R. Israel, P. W. Greene, "Fracture of an alumina femoral head used in ceramic-on-ceramic total hip arthroplasty", *J. Arthroplasty*, **23**[1239], 1225–30, (2008)

[133] J. P. Garino, "Modern ceramic-on-ceramic total hip systems in the United States: early results", *Clin. Orthop. Relat. Res.*, **379**, 41–7, (2000)

[134] I. C. Clarke, M. Manaka, D. D. Green, "Current status of zirconia used in total hip

implants", *Am. J. Bone Joint Surg.*, **85** [Suppl. 4], 73–84, (2003)

[135] J. Chevalier, A. H. De Aza, G. Fantozzi, M. Schehl, R. Torrecillas, "Extending the lifetime of orthopaedic implants", *Advanced Mater.*, **12** [21], 1619–21, (2000)

[136] G. Fantozzi, G. Orange, "Thermomechanical properties of zirconia toughenedalumina materials", J. S. Moya, S. De Aza editors, *Processing of advanced ceramics,* Soc Esp Ceram Vidr Arganda del Rey, Madrid, Spain, 187–215, (1986)

[137] D. J. Green, R. H. J. Hannink, M. V. Swain, "Transformation toughening of ceramics", Boca Raton, FL, CRS Press, Inc., 232, (1989)

[138] N. Claussen, "Fracture toughness of Al_2O_3 with an unstabilized ZrO_2 dispersed phase", *J. Am. Ceram. Soc.*, **59** [1–2], 49–51, (1976)

[139] R. Heros, G. Willmann, "Ceramics in total hip arthroplasty: history, mechanical properties, clinical results andcurrent manufacturing state of the art", *Seminars Arthroplasty,* **9**, 114–22, (1998)

[140] B. Masson, "Emergence of the alumina matrix composite in total hip arthroplasty", *Int. Orthop.*, **33**, 359–63, (2009)

[141] G. Maccauro, G. Bianchino, S. Sangiorgi, Development of a new zirconia-toughened alumina: promising mechanical properties and absence of in vitro carcinogenicity. Int J Immunopathol Pharmacol 2009;22:773–9

[142] M. Fernandez-Fairen, A. Blanco, A. Murcia, P. Sevilla, F. J. Gil, Aging of retrieved zirconia femoral heads. Clin Orthop Relat Res 2007;462:122–9

[143] G. Pezzotti, K. Yamada, A. Porporati, M. Kuntz, K. Yamamoto, Fracture toughness analysis of advanced ceramic composite for hip prosthesis. J Am Ceram Soc 2009;92:1817–22

[144] G. Pezzotti, T. Saito, Y. Takahashi, K. Fukatsu, N. Sugano, Surface topology of advanced alumina/zirconia composite femoral head as compared with commercial femoral heads made of monolithic zirconia. J Am Ceram Soc 2011;94:945–50

[145] K. Haraguchi, N. Sugano, T. Nishii, H. Miki, K. Oka, H. Yoshikawa, Phase transformation of a zirconia ceramic head after total hip arthroplasty. Journal of Bone & Joint Surgery – British Volume. Sep 2001 ;83(7):996-l 000

[146] F. L. Riley, Silicon nitride and related materials. J Am Ceram Soc 2000;83:245–65

[147] C. R. Howlett, E. McCartney, W. Ching, The effect of silicon nitride ceramic on rabbit skeletal cells and tissue. An in vitro and in vivo investigation. Clin Orthop Relat Res 1989;244:293–304;

[148] M. Mazzocchi, D. Gardini, P. L. Traverso, M. G. Faga, A. Bellosi, On the possibility of silicon nitride as a ceramic for structural orthopaedic implants. Part II: chemical stability and wear resistance in body environment. J Mater Sci Mater Med 2008;19(8):2889–901

[149] W. Wang, M. Hadfield, A. A Wereszczak, Surface strength of silicon nitride in relation to rolling contact performance. Ceram Int 2009;35:3339–46

[150] C. W. Li, J. Yamanis, Super-tough silicon nitride with R-curve behavior. Ceram Eng Sci Proc 1989;10(7–8):632–45

[151] P. F. Becher, Microstructural design of toughened ceramics. J Am Ceram Soc 1991;74:255–69

[152] B. S. Bal, J. Garino, M. Ries, M. N. Rahaman, Ceramic materials in total joint arthroplasty. Semin Arthroplasty 2006;17:94–101;

[153] M. N. Rahaman, A. Yao, S. B. Bal, J.P. Garino, M. D. Ries, Ceramics for prosthetic hip and knee joint replacement. J Am Ceram Soc 2007;90:1965–88

[154] M. Luo, G. Y. Hou, J. F. Yang, Manufacture of fibrous b-Si3N4 reinforced biomorphic SiC matrix composites for bioceramic scaffold applications. Mater Sci Eng C 2009;29:1422-7

[155] M. Mazzocchi, A. Bellosi, On the possibility of silicon nitride as a ceramic for structural orthopaedic implants. Part I: processing, microstructure, mechanical properties, cytotoxicity. J Mater Sci Mater Med 2008;19:2881–7

[156] J. Xu, K. Kato, Formation of tribochemical layer of ceramics sliding in water and its role for low friction, Wear 245, 61-75 (2000)

[157] S. Hah, C. B. Burk, T. E. Fischer, "Surface quality of tribochemically polished silicon nitride", J. Electrochem. Soc., **146**, 1505–9, (1999)

[158] C. Iliev, "On the wear behaviour of silicon nitride sliding against metals in water", *Ind. Lubr. Tribol.*, **62**, 32–6, (2010)

[159] A. Yamamoto, R. Honma, M. Sumita, T. Hanawa, "Cytotoxicity evaluation of ceramic particles of different sizes and shapes", *J. Biomed. Mater. Res.*, **68**, 244–256, (2004)

[160] W. M. Sanford, K. A. Saum, "Accelerated oxidative aging testing of UHMWPE", *Biomaterials*, **21**, 1451-60, (2000)

[161] D. C. Sun, A. Wang, C. Stark, J. H. Dumbleton, "The concept of stabilization in UHMWPE", Trans Fifth World Biomater Cong, (1996)

[162] W. G. Di Maio, W. B. Lilly, W. C. Moore, K. A. Saum, "Low wear, low oxidation radiation crosslinked UHMWPE", *Trans. Orthop. Res. Soc.*, **23**, (1998)

[163] H. McKellop, B. Yeom, D. C. Sun, W. M. Sanford, "Accelerated aging of irradiated UHMW polyethylene for wear evaluations", *Orthop. Res. Soc.*, **21**, (1996)

[164] K. W. Greer, M. B. Schmidt, J. V. Hamilton, "The hip simulator wear of gamma-vacuum, gamma-air, and ethylene oxide sterilized UHMWPE following a severe oxidative challenge", *Trans. Orthop. Res. Soc.*, **23**, (1998)

[165] W. M. Sanford, W. C. Moore, D. McNulty, C. Frisinger, T. P. Schmalzried, "Hip simulator study of the effect of sterilization and oxidation on UHMWPE wear", *Trans. Orthop. Res. Soc.*, **22**, (1997)

[166] A. A. Edidin, C. W. Jewett, A. Kalinowski, K. Kwarteng, S.M. Kurtz, "Degradation of mechanical behavior in UHMWPE after natural and accelerated aging", Biomaterials, 21, 1451-1460, (2000)

[167] D. C. Sun, C. Stark, J. H. Dumbleton, "Development of an accelerated aging method for evaluation of long-term irradiation effects on UHMWPE implants", *Polym. Reprints.*, **35**, 969–970, (1994)

[168] W. M. Sanford, K. A. Saum, "Accelerated oxidative aging testing of UHMWPE", *Trans. Orthop. Res. Soc.*, **20**, (1995)

[169] M. P. Bostrom, A. P. Bennett, C. M. Rimnac, T. M. Wright, "The natural history of ultra high molecular weight polyethylene", *Clin. Orthop.*, **309**, 20–28, (1994)

[170] C. M. Rimnac, R. W. Klein, A. H. Burstein, T. M. Wright, T. J. Santner, "In vitro chemical and mechanical degradation of UHMWPE: One year results", *Trans. Orthop. Res. Soc.*, **19**, (1994)

[171] S. M. Kurtz, O. Muratoglu, L. Mounib, "Interinstitutional reproducibility of standard accelerated ageing methods for UHMWPE", in 46th Annual Meeting of the Orthopaedic Research Society, Orlando, FL, USA, (2000)

[172] G. Pezzotti, T. Kumakura, K. Yamada, T. Tateiwa, L. Puppulin, W. Zhu, "Confocal Raman spectroscopic analysis of cross-linked ultra-high molecular weight polyethylene for application in artificial hip joints", *Journal of biomedical optics*, **12**, (2007)

[173] F. Rull, A. Prieto, J. Casado, F. Sobron, H. Edwards, "Estimation of crystallinity in polyethylene by Raman spectroscopy", *Journal of Raman spectroscopy*, **24**, 545-50, (1993)

[174] M. Glotin, L. Mandelkern, "A Raman spectroscopic study of the morphological structure of the polyethylenes", *Colloid and Polymer Science*, **260**, 182-92, (1982)

[175] C. C. Naylor, R. J. Meier, B. J. Kip, K. P. Williams, S. M. Mason, N. Conroy, "Raman spectroscopy employed for the determination of the intermediate phase in polyethylene", *Macromolecules*, **28**, 2969-78, (1995)

[176] L. Puppulin, S. Della Negra, N. Sugano, O. Sbaizero, G. Pezzotti, "Surface modification induced by in-vitro wear and oxidation on γ-irradiated UHMWPE hip liners belonging to different commercial generations", *J. Mech. Behav. Biom. Mat.*, **53**, 414-426, (2016)

[177] M. Ghamnia, C. Jardin, and M. Bouslama, "Luminescent Centres F and F+ in α-Alumina Detected by Cathodoluminescence Technique," *J. Electron Spectros. Relat. Phenomena*, **133** [1-3], 55–63, (2003)

[178] T. Norby, M. Widerøe, R. Glöckner, Y. Larring, "Hydrogen in oxides," *Dalton transactions*, **3012** [8], (2004).

[179] M. Youssef, B. Yildiz, "Hydrogen defects in tetragonal ZrO_2 studied using density functional theory," *Physical Chemistry Chemical Physic*, **16**, 1354-1365, (2014)

[180] J. Robertson, "Electronic structure of silicon nitride", *Philosophical Magazine B*, **63**, 47-77, (1991)

[181] J. Robertson, M.J. Powell, "Gap states in silicon nitride", *Applied Physics Letters*, **44**, 415-417, (1984)

[182] C. Di Valentin, G. Palma, G. Pacchioni, "Ab initio study of transition levels for intrinsic defects in silicon nitride", *The Journal of Physical Chemistry C*, **115**, 561-569, (2010)

[183] J. Robertson, W. Warren, J. Kanicki, "Nature of the Si and N dangling bonds in silicon nitride", *Journal of non-crystalline solids*, **187**, 297-300, (1995)

[184] L. Skuja, "The Origin of the Intrinsic 1.9 eV Luminescence Band in Glassy SiO2,," *J. Non. Cryst. Solids*, **179,** 51–69, (1994)

[185] S. K. Bhateja, R. W. Duerst, E. B. Aus, E. H. Andrews, "Free radicals trapped in polyethylene crystals", *J. Macromol. Sci. Phys.*, **B34** [3], 263–72, (1995)

[186] F. J. Medel, F. García-Álvarez, E. Gómez-Barrena, J. A. Puértolas, "Microstructure

Changes of Extruded Ultra High Molecular Weight Polyethylene After Gamma Irradiation and Shelf-Aging", *Polym. Degrad. Stab.*, **88** [3], 435–443, (2005)

[187] M. Goldman, R. Gronsky, G.G. Long, and L. Pruitt, "The Effects of Hydrogen Peroxide and Sterilization on the Structure of Ultra High Molecular Weight Polyethylene", *Polym. Degrad. Stab.,* **62** [1], 97–104, (1998)

[188] F. J. Buchanan, J. R. White, B. Sim, S. Downes, "The Influence of Gamma Irradiation and Aging on Degradation Mechanisms of Ultra-High Molecular Weight Polyethylene", *J. Mater. Sci. Mater. Med.*, **12** [1], 29–37, (2001)

[189] S. K. Bhateja, E. H. Andrews, S.M. Yarbrough, "Radiation Induced Crystallinity Changes in Linear Polyethylenes: Long Term Aging Effects", *Polym. J.*, **21** [9], 739–750, (1989)

[190] Y. Zhao, Y. Luo, B. Jiang, "Effect of Irradiation on Crystallinity and Mechanical Properties of Ultrahigh Molecular Weight Polyethylene," *J. Appl. Polym. Sci.*, **50** [10], 1797–1801, (1993)

[191] E. Oral, B.W. Ghail, O.K. Muratoglu, "The Elimination of Free Radicals in Irradiated UHMWPEs With and Without Vitamin E Stabilization by Annealing Under Pressure", *J. Biomed. Mater. Res. B Appl. Biomater.*, **97** [1], 167–174, (2011)

[192] C. P. Stephens, R. S. Benson, M. E. Martinez-Pardo, E. D. Barker, J. B. Walker, T.P. Stephens, "The Effect of Dose Rate on the Crystalline Lamellar Thickness Distribution in Gamma-Radiation of UHMWPE", *Nucl. Instruments Methods Phys. Res. Sect. B Beam Interact. with Mater. Atoms*, **236** [1-4], 540–545, (2005)

[193] G. Patel, A. Keller, "Crystallinity and the Effect of Ionizing Radiation in Polyethylene. Crosslinking and the Crystal Core", *Journal of Polymer Science: Polymer Physics Edition*, 13 [2], 303-21, (1975)

[194] N.C. Billingham and P.D. Calvert, "The Physical Chemistry of Oxidation and Stabilisation of Polyolefins," *Dev. Polym. Stab.*, **3** 139–190 (1980)

[195] Y. S. Jo, J. A. Schultz, S. Tachi, S. Contarini, J. W. Rabalais, "Surface stoichiometry, structure, and chemisorption on silicon nitride studied by direct recoiling, x-ray photoelectron spectroscopy, and Auger electron spectroscopy", *Journal of applied physics*, 60, 2564-2572, (1986)

[196] R. M. Bock, B. J. McEntire, B. S. Bal, M. N. Rahaman, M. Boffelli, G. Pezzotti, "Surface modulation of silicon nitride ceramics for orthopaedic applications", *Acta biomaterialia*, 26, 318-330, (2015)

[197] S. Raider, R. Flitsch, J. Aboaf, W. Pliskin, "Surface oxidation of silicon nitride films", *Journal of The Electrochemical Society*, **123,** 560-565, (1976)

[198] H. Kuzmany, "Solid-State Spectroscopy: An Introduction", Springer Berlin, Heidelberg, (2009)

[199] J. Solé, L. Bausa, D. Jaque, "An introduction to the optical spectroscopy of inorganic solids", John Wiley & Sons, (2005)

[200] A. Smekal, "Zur quantentheorie der dispersion", *Naturwissenschaften*, **11**, 873-875, (1923)

[201] C.V. Raman, "A new radiation", *Indian Journal of physics*, **2**, 387-398, (1928)

[202] F. Adar, M. Delhaye, E. DaSilva, "Evolution of instrumentation for detection of

the Raman effect as driven by available technologies and by developing applications", *Journal of chemical education*, **84**, 50-64, (2007)

[203] E. Smith, G. Dent, "Modern Raman Spectroscopy: A Practical Approach", Wiley, Chichester, United Kingdom, (2005)

[204] D. Lin-Vien, N. B. Colthup, W. G. Fateley, J. G. Grasselli, "The Handbook of Infrared and Raman Characteristic Frequencies of Organic Molecules Elsevier", Academic Press, New York, (1991)

[205] D. A. Skoog, F. J. Holler, S. R. Crouch, "Principles of Instrumental Analysis", Cengage Learning, India, (2007)

[206] G.S. Kino, T. R. Corle, "Confocal scanning optical microscopy and related imaging systems", Academic Press, (1996)

[207] P. Van Der Heide, "X-Ray photoelectron spectroscopy. An Introduction to Principles and Practices", *Analytical and Bioanalytical Chemistry*, **405** [8], 2415-2416, (2013)

[208] J. M. Wagner, "X-Ray Photoelectron Spectroscopy", Nova Science Publishers, New York, (2011)

[209] K. C. Siegbahn, A. Nordling, K. Fahlman, J. Hamrin, N. Hedman, T. Johansson, S. Bergmark, E. Karlsson, "Atomic, molecular and solid-state structure studied by means of electron spectroscopy", *Nova Acta Regiae Societatis Scientiarum Upsaliensis*, **20**, 282 (1967).

[210] Electron Spectroscopy for Atoms, Molecules and Condensed Matter, Nobel Lecture, December 8, 1981

[211] Wagner, Riggs, Davis, Moulder "Handbook of X-Ray photoelectron spectroscopy", Perkin-Elmer Corporation, Physical Electronics Division, (1979)

[212] J. F. Watts, J. Wolstenholme, "An introduction to surface analysis by XPS and AES", Chichester, Wiley, (2003)

[213] L. Kover, "Chemical Effects in XPS", in Surface Analysis by Auger and Photoelectron Spectroscopy, D. Briggs and J.T. Grant editors, IM Publications, Chichester, (2003)

[214] N. Fairley, "XPS Lineshapes and Curve Fitting", in Surface Analysis by Auger and Photoelectron Spectroscopy, D. Briggs and J.T. Grant editors, IM Publications, Chichester, (2003)

[215] S. Hofmann, "Auger- and X-Ray Photoelectron Spectroscopy in Materials Science. A User-Oriented Guide", Springer Verlag, Berlin, (2013)

[216] W. Crookes, "On radiant matter", *Journal of the Franklin Institute*, **108**, 305-316, (1879)

[217] J. Smith, R. Stenstrom, "Electron-excited luminescence as a petrologic tool", *The Journal of Geology*, 627-635, (1965)

[218] D. Krinsley, P. Hyde, "Cathodoluminescence studies of sediments", *Scan. Electron Microsc.*, 409-416, (1971)

[219] D. B. Holt, B. G. Yacobi, "Extended defects in semiconductors: electronic properties, device effects and structures", Cambridge University Press, (2007)

[220] R. Eisberg, R. Resnick, "Quantum physics", John Wiley & Sons, (1985)

[221] B.G. Yacobi, D.B. Holt, "Cathodoluminescence microscopy of inorganic solids", Springer Science & Business Media, (2013)

[222] A. Krasheninnikov, K. Nordlund, "Ion and electron irradiation-induced effects in nanostructured materials", Journal of applied physics, 107, (2010)

[223] S. Boggs, D. Krinsley, "Application of cathodoluminescence imaging to the study of sedimentary rocks", Cambridge University Press, (2006)

[224] B. G. Yacobi, D. B. Holt, "Cathodoluminescence scanning electron microscopy of semiconductors", J. Appl. Phys., 59 [4], (1986)

[225] G. Pezzotti, "Spatially resolved Raman and cathodoluminescence probes in electronic materials: basics and applications", *Phys. Status Solidi*, 208, 976–999, (2011)